THEORETICAL PREDICTIONS OF AXONAL PATHWAYS ACTIVATED BY SUBTHALAMIC DEEP BRAIN STIMULATION

by

KABILAR GUNALAN

Submitted in partial fulfillment of the requirements for the degree of

Doctor of Philosophy

Dissertation Advisor: Dr. Cameron C. McIntyre

Department of Biomedical Engineering

CASE WESTERN RESERVE UNIVERSITY

January, 2018

CASE WESTERN RESERVE UNIVERSITY

SCHOOL OF GRADUATE STUDIES

We hereby approve the thesis/dissertation of

Kabilar Gunalan

candidate for the degree of Doctor of Philosophy *.

Committee Chair

Dr. Dominique Durand

Committee Member

Dr. Cameron McIntyre

Committee Member

Dr. Benjamin Walter

Committee Member

Dr. Roberto Galán

Date of Defense

October 20, 2017

*We also certify that written approval has been obtained for any proprietary material contained therein.

Dedication

I dedicate this dissertation to my parents.

Table of Contents

List of Tables

List of Figures

Acknowledgments

The love and support of my colleagues, family, and friends have guided and motivated me during this training period. For this encouragement, I would like to thank them.

My advisor, Cameron McIntyre, has patiently helped me understand this dynamic field that was once foreign to me. He allowed me the freedom to pursue my interests, thereby providing me the flexibility to find my passions. Cameron's unique vision of the trajectory of the field helped me focus on projects with impact, and taught me how to tell a story that empowers the science behind it. Cameron fostered an environment that prioritized collaboration and mentorship, both within and between labs. Because of this well-rounded experience, I learned to be a team player and I learned the importance of interdisciplinary communication. I am truly grateful for his commitment to me and my training throughout the years.

I would also like to thank Ashutosh Chaturvedi, who mentored me during the first half of my studies. I learned an incredible amount from him about how to conduct independent research, and leaned on him for guidance even after he graduated from the lab. I truly enjoyed the time we spent working on projects together.

Bryan Howell joined the lab as a postdoctoral scholar only a few years ago, but since that time has had a tremendous impact on my training. His unbounded passion for the sciences and his clarity in focus enables him to enthusiastically explain technically demanding concepts, and elevated the level

of the projects we worked on together. He changed the trajectory of my dissertation and I am forever grateful for everything that he has contributed to my training.

Angela Noecker has been a valuable resource for me throughout my time in the lab. She helped me work through many problems and collaborated on a number of projects with me. No matter the situation, she always has a positive attitude and she has been a pleasure to work with over the years.

Ross Anderson has been instrumental in cultivating my presentation skills. For years, he worked with me on every talk to improve my storytelling capabilities, which is a critical, but often overlooked component of furthering scientific fields. The speaking award I received at the ASSFN conference is a testament to the impact his mentorship has had on me.

I would like to thank Scott Lempka, who has mentored me through several different aspects of my training. He made me a better writer and patiently helped me understand the stimulus waveform. Scott is very thorough with his work and I have enjoyed learning from him during our collaboration over the past two years.

I am grateful to Kyle Taljan and Ken Sakaie, who mentored me in the field of tractography, thereby providing me with both a theoretical and working knowledge of this complex tool that was critical to my dissertation.

I would also like to thank our collaborators at the University of Minnesota, specifically Noam Harel, Remi Patriat, Yuval Duchin, Guillermo Sapiro, Eric Maurer, and Jerrold Vitek. They provided me with patient imaging and clinical data that enabled the analysis presented herein.

My doctoral training would not have been complete without the bigger picture perspective provided by my guidance committee: Dominique Durand, Benjamin Walter, and Roberto Galán. Dr. Durand's course on electrical stimulation of excitable tissue gave me the solid foundation upon which I based this dissertation. As a member of my committee, Dr. Durand helped me thoroughly understand the rigor of the scientific method. Dr. Walter consistently instilled in me the importance of innovating within a clinical context, and Dr. Galán fortified my ability to use first principles in developing conclusions from my results.

I would also like to thank the other past and present members of the lab and collaborators who created a collaborative environment without which I would not have been able to conduct my research. These individuals include Rick Arlow, Sinem Balta Beylergil, Kelsey Bower, Sarah Carr, Scott Cooper, Trygve Dolber, AmirAli Farokhniaee, Thomas Foutz, Anneke Gilbert, Phil Hahn, Theresa Lempka, Luis Lujan, Andre Machado, Nicholas Maling, Jonathan Miller, Brian Murphy, Sarah Ozinga, Martin Reich, Mohit Saxena, Reuben Shamir, Jennifer Sweet, Curtis Tatsuoka, Suraj Thyagaraj, Jens Volkmann, and Michael Wassef. Whether it was through working on projects or generating insightful discussions, each person contributed to both my training and my perspective in viewing scientific discovery as a communal effort.

This work has relied heavily on the use of the High Performance Computing Resource in the Core Facility for Advanced Research Computing at Case Western Reserve University. I would like to thank Mike Warfe, Hadrian

Djohari, Sanjaya Gajurel, Emily Dragowsky, and S A Meka, who supported the computational infrastructure required to run our analyses.

My family and friends have supported and provided me a positive distraction to balance the rigors of this training. I would like to thank my sister, Pallavi Gunalan, for her love and guidance, my partner, Anita Rohra, for her love, patience, and support, as well as my uncle, Narayan Lalchand, for providing me a home away from home as I pursued my studies.

Most importantly, I would like to thank my parents, whose love and support have been continuous and unconditional. I owe everything that I have accomplished to them. From instilling in me the importance of an education, to inspiring me to do my best to make this world a better place, they have served as steady guides through this difficult, but rewarding journey. My mother's care for everyone around her and my father's dedication to his family and his craft have set examples for me that I hope to one day attain. Thank you for all of your sacrifices. I love you both.

I would also like to thank my funding sources. I have been supported by grants from the National Institutes of Health (R01 NS085188; T32 GM007250, TL1 TR000441, T32 EB004314) and the U.S. Department of Education (GAANN P200A100112).

List of Abbreviations

AVT	activation volume tractography
CSF	cerebrospinal fluid
CT	computed tomography
CbTT	cerebellothalamic tract
DBS	deep brain stimulation
DF	driving force
DW	diffusion-weighted
ETI	electrode-tissue interface
FC	field-cable
FEM	finite element method
FA	fractional anisotropy
GPe	globus pallidus externus
GPi	globus pallidus internus
HD	hyperdirect
Hz	Hertz
IC	internal capsule
IPG	implantable pulse generator
LF	lenticular fasciculus
MDF	modified driving force
ML	medial lemniscus
MRI	magnetic resonance image
PD	Parkinson's disease
PAM	pathway-activation model
SP	subthalamopallidal
STN	subthalamic nucleus
SW	susceptibility-weighted
T1W	T1-weighted
T2W	T2-weighted
μm	micrometer

μs	microsecond
V	Volt
VTA	volume of tissue activated

List of Publications and Awards

Manuscripts published

- **Gunalan K**, Chaturvedi A, Howell B, Duchin Y, Lempka SF, Patriat R, Sapiro G, Harel N, McIntyre CC. Creating and parameterizing patient-specific deep brain stimulation pathway-activation models using the hyperdirect pathway as an example. PLOS ONE. 2017.
- Murphy BA, Miller JP, **Gunalan K**, Ajiboye AB. Contributions of subsurface cortical modulations to discrimination of executed and imagined grasp forces through stereoelectroencephalography. PLOS ONE. 2016.
- Reich MM, Steigerwald F, Sawalhe A, Reese R, **Gunalan K**, Johannes S, Matthies C, McIntyre CC, Volkmann J. Short pulse width widens the therapeutic window of subthalamic neurostimulation. Annals of Clinical and Translational Neurology. 2015.
- Sweet JA, Walter BL, **Gunalan K**, Chaturvedi A, McIntyre CC, Miller JP. Fiber tractography of the axonal pathways linking the basal ganglia and cerebellum in Parkinson disease: implications for targeting in deep brain stimulation: Clinical article. J Neurosurgery. 2014.

Manuscripts in review

- **Gunalan K***, Howell B*, McIntyre CC. Quantifying axonal responses in patient-specific models of subthalamic deep brain stimulation.
- Lempka SF, Howell B, **Gunalan K**, Machado AG, McIntyre CC. Characterizing the stimulus waveforms generated by implanted pulse generators in deep brain stimulation.

Manuscripts in preparation

- **Gunalan K**, Howell B, Patriat R, Noecker AM, Harel N, McIntyre CC. Theoretical predictions of the axonal pathways directly activated by subthalamic deep brain stimulation.
- **Gunalan K**, McIntyre CC. Biophysical properties of the hyperdirect pathway necessary to match clinical cortical evoked potentials from subthalamic deep brain stimulation.
- Anderson RW, **Gunalan K,** Howell B, McIntyre CC. Action potential initiation and propagation in the hyperdirect pathway during subthalamic deep brain stimulation.
- Howell B, Choi KS, Rajendra J, **Gunalan K**, Mayberg HS, McIntyre CC. Axonal responses predicted with patient-specific models of subcallosal cingulate deep brain stimulation for intractable depression.

- Howell B, **Gunalan K**, McIntyre CC. Novel driving force-based predictor for estimating axonal activation.

Awards

- Best oral presentation by a resident/fellow. American Society for Stereotactic and Functional Neurosurgery Biennial Meeting. 2016.
- Graduate student excellence in mentorship award. Department of Biomedical Engineering. Case Western Reserve University. 2016.

Theoretical Predictions of Axonal Pathways Activated

by Subthalamic Deep Brain Stimulation

Abstract

by

KABILAR GUNALAN

Deep brain stimulation (DBS) is an established clinical therapy for Parkinson's disease (PD). Experimental data suggests that DBS activates axons near the active electrode contact. However, the specific axonal pathways directly activated by DBS are not clearly defined. In this study, we used patient-specific computational models to provide insights of the pathways mediating the therapeutic response to subthalamic DBS.

One such model, known as the field-cable pathway-activation model (FC PAM), is the current gold standard for predicting axonal activation on a patient-specific basis. However, FC PAMs require significant technical expertise and computational resources. Thus, the driving force (DF) and volume of tissue activated (VTA) methods, which are derived from simplified FC models, are typically used in clinical research studies. We compared the predictions of the FC PAM, DF PAM, and VTA PAM during subthalamic DBS. Unfortunately, none of these simplified models (i.e. DF PAM or VTA PAM) were able to match the

results of the FC PAM in terms of stimulation thresholds or pathway activation estimates across all pathways and combinations of stimulus parameters.

The pathways in the subthalamic region that mediate the therapeutic effects of DBS are not clearly defined. We constructed FC PAMs of three PD patients explicitly representing six axonal pathways. We calculated the pathways activated by the clinically-defined therapeutic stimulation setting in each patient. Our results suggest that therapeutic stimulation activates multiple pathways and these pathways were not consistent among the PD patients.

We used an FC PAM to dissect the neural elements mediating cortical evoked potentials. Experimental recordings of cortical evoked potentials are used to evaluate the effects of subthalamic DBS and have components that occur at discrete times after each stimulus pulse. We compared the conduction times for small (5.7 μm), medium (10.0 μm), and large (15.0 μm) diameter corticofugal axons of both the hyperdirect and internal capsule pathways. We found that subthalamic DBS likely activates small diameter hyperdirect axons resulting in the medium latency cortical evoked potentials.

This work lays the foundation for studies selectively targeting pathways in the subthalamic region with the use of FC PAMs to dissect the complex clinical response to stimulation.

Chapter 1 – Introduction

1.1. Parkinson's disease

Parkinson's disease (PD) is a neurodegenerative disorder in which patients suffer from motor symptoms [Jankovic et al., 1990; Obeso et al., 2010] and non-motor symptoms [Barone et al., 2009]. The diagnosis of PD is based on the cardinal motor symptoms, including resting tremor, bradykinesia, rigidity, and postural instability. However, diagnosis and management of the disease is difficult as the patients usually present with a heterogeneous combination of symptoms.

The pathological origin of these PD symptoms is thought be a result of the dysfunction of brain circuits [DeLong, 1990; McIntyre and Hahn, 2010]. PD patients have a loss of dopaminergic neurons in the substantia nigra pars compacta [Damier et al., 1999]. The loss of these cells is thought to manifest into synchronized oscillatory activity within the basal ganglia [Brown et al., 2001]. Administration of levodopa, a dopaminergic medication, in PD patients reduces this oscillatory activity and concurrently improves symptoms such as bradykinesia and rigidity [Kuhn et al., 2006]. But whether this oscillatory activity is a symptomatic expression of the disease or a cause of the symptoms is yet to be fully characterized.

Upon diagnosis, PD patients are initially treated with dopaminergic medications to manage the symptoms of the disease [Cotzias et al., 1969; Connolly and Lang, 2014]. As the disease progresses, patients require increased dosages of levodopa to manage the motor symptoms but levodopa-

induced dyskinesias can occur [Rascol et al., 2000; Schrag and Quinn, 2000]. Dyskinesias are a side effect of the levodopa therapy that often compromises the overall goal of levodopa on the improvement in quality of life. Surgical alternatives, such as ablation surgery and deep brain stimulation (DBS) [Benabid et al., 1987], help manage the motor symptoms thereby reducing the required amount of dopaminergic medications and controlling dyskinesias.

1.2. Deep brain stimulation

DBS is a surgical alternative for the treatment of the motor symptoms of PD. DBS systems are completely internalized with a lead implanted within the brain connected, with an extension wire, to an implanted pulse generator (IPG) (Figure 1.1). These systems produce a pulsatile electrical current within the brain that modulates the activity of the neurons near the DBS lead to suppress symptoms. DBS has become an established therapy, largely replacing ablative surgery, as it provides a reversible and customizable alternative to lesioning [Benabid et al., 1991].

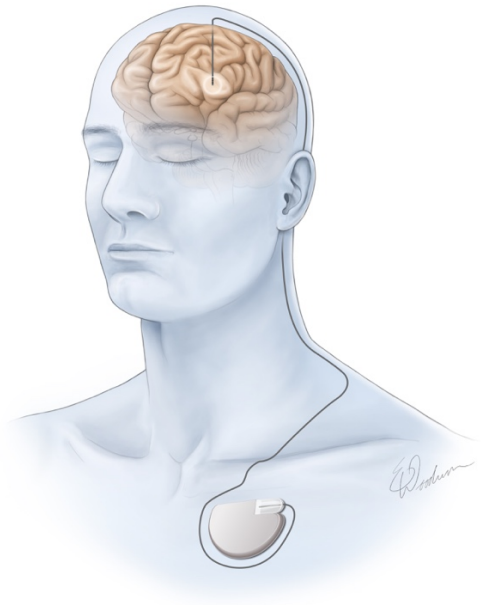

Figure 1.1. Illustration of an implanted deep brain stimulation system. The system includes a pulse generator implanted in the chest that is connected with an extension wire to the DBS lead.

An important factor in the outcome of DBS is the location of the therapeutic contact [Rolston et al., 2016]. Stereotactic surgical targeting of the DBS lead provides a systematic method for precisely positioning the electrode within the brain. First, preoperative structural magnetic resonance images (MRIs) are acquired of the patient. Second, on the day of surgery, a stereotactic frame is attached to the patient's head [Leksell, 1950] and the patient undergoes a MRI or computed tomography (CT) scan with this frame in place. Third, the surgeon then fuses the two sets of images to visualize the target structures on the MRI in the context of this stereotactic coordinate system. The surgeon uses structures that are visible on the MRIs and distances from visible landmarks to determine a target for the DBS lead. Fourth, once the patient is in the operating room, it is also common that microelectrode recordings can be used to map and

verify the target structure, and intraoperative stimulation with the DBS lead is used to verify suppression of symptoms.

For PD, there are generally two structures within the basal ganglia that can be targeted for stimulation: subthalamic nucleus (STN) or globus pallidus internus (GPi) [Limousin et al., 1998]. Initially it was believed that STN DBS produced better outcomes, but similar motor symptom control and reduction in antiparkinsonian medications has been shown with stimulation of both targets [Anderson et al., 2005; Odekerken et al., 2013; Miocinovic et al., 2013]. Even within the subthalamic region, there is not a consensus on the optimal target [Hamel et al., 2017]. This is likely because the neural elements mediating the therapeutic effect of stimulation are not well characterized.

The choice of stimulation settings is another important factor that effects therapeutic outcomes. There are thousands of programmable stimulation setting combinations as the electrode contact configuration, stimulus pulse amplitude, stimulus pulse width, and stimulus pulse frequency can be individually modified. For STN DBS, the stimulus pulse width is typically programmed to 60 μs or 90 μs [Volkmann et al., 2006] and the stimulus pulse frequency is between 130 Hz and 200 Hz [Moro et al., 2002], but the electrode contact configuration and stimulus pulse amplitude are dependent on each patient's response. A few weeks after surgery, the clinician performs a monopolar review of the device to determine the ideal settings for stimulation [Volkmann et al., 2002]. In this process, a contact is selected under monopolar configuration and the stimulus amplitude is incrementally increased. For each stimulus amplitude, any symptom

improvement and side effects are noted. This process is repeated for all four electrode contacts. The electrode contact with the largest amplitude difference between the suppression of symptoms and evolution of side effects is selected. This programming process is currently done without exact knowledge of where the electrode is placed within the target region of the patient's brain, but commercial software technologies are emerging onto the market that provide this visualization.

Given the appropriate patient selection, electrode localization, and stimulation parameter selection, DBS can improve the quality of life for PD patients; however, the mechanisms of action are still under investigation. Initial theories on the mechanisms of action of DBS was that it suppressed neuronal activity in the nucleus where stimulation is delivered thereby mimicking the mechanism of action of lesioning therapies [Lozano et al., 2002]. However, experimental [Hashimoto et al., 2003; Anderson et al., 2003; Montgomery, 2006] and theoretical [Ranck, 1975; McIntyre et al., 2004; Miocinovic et al., 2006] studies suggest that clinical DBS generates action potentials in axons near the electrode. These action potentials are transmitted to the downstream nuclei with an overall effect of reducing the pathological beta oscillatory activity in the basal ganglia [Giannicola et al, 2010; Whitmer et al., 2012] and as a result improving information flow [Zimnik et al., 2015]. In this dissertation, we focus on quantifying those axonal pathways directly activated by therapeutic STN DBS using patient-specific computational models.

1.3. Electrical stimulation modeling

Action potential conduction along an axon can be modeled with a multi-compartment cable structure (Figure 1.2) [Hodgkin and Huxley, 1952]. The model of the unmyelinated squid giant axon originally developed by Hodgkin and Huxley has subsequently been customized for a myelinated mammalian membrane with representations of nodal and internodal compartments [Frankenhaeuser and Huxley, 1964; Sweeney et al., 1987]. In this dissertation, we use the latest evolution of this axon model developed by McIntyre et al. [2002] that has been validated against experimental measurements for action potential shape, conduction velocity, strength-duration relationships, and strength-distance relationships.

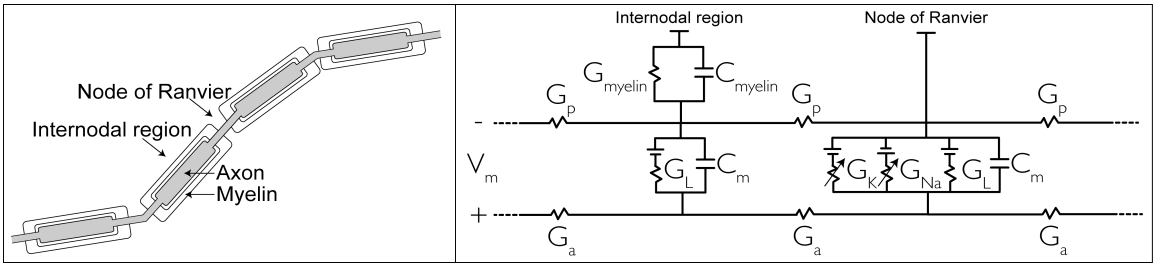

Figure 1.2. Multi-compartment cable axon model. (Left) Illustrative example of a cross section of a myelinated axon. (Right) Schematic diagram of a simplified double cable axon model with representations of the cell membrane and myelin. G_a – axial conductance; G_p – periaxonal conductance; G_{myelin} – myelin conductance; G_L – leakage conductance; G_K – potassium conductance; G_{Na} – sodium conductance; C_m – membrane capacitance; C_{myelin} – myelin capacitance; V_m – transmembrane voltage.

For a given axon model, McNeal [1976] described the methodology for calculating the threshold amplitude for activation of an axon with an extracellular stimulating electrode placed at a finite distance from the axon. McNeal showed

that the change in transmembrane voltage of the cable axon model (V_m, Figure 1.2) in response to an applied extracellular voltage is described with a set of partial differential equations (Equation 1.1). The assumption with this model is that the voltage on the outside of the axon is dictated solely by the extracellular voltage generated by the stimulating electrode. Thus, to understand the effects of stimulation in the nervous system the voltage distribution generated by a stimulating electrode needs to be coupled to cable models of axons.

$$C_m \frac{dV_{m,i}}{dt} + I_i - G_a \cdot \Delta^2 V_{m,i} = G_a \cdot \Delta^2 V_{e,i}$$

Equation 1.1. The cable equation. G_a – axial conductance; I – ionic current through the membrane; C_m – membrane capacitance; V_m – transmembrane voltage; V_e – extracellular voltage generated by stimulating electrode; i – index of a compartment; Δ - second difference operator.

This general theory of axon stimulation models has been integrated with patient imaging data to quantify the axonal pathways activated by DBS (Figure 1.3) [Miocinovic et al., 2006]. In order to do so, first, the voltage distribution generated by the stimulating electrode is calculated within a volume conductor model using the finite element method. These volume conductor models of DBS have evolved from a point source in an infinite homogeneous medium to incorporating patient-specific properties such as the DBS macroelectrode, boundaries of the head, and anisotropic tissue conductivities [Foutz and McIntyre, 2010; Chaturvedi et al., 2010; Howell and McIntyre, 2016; Howell and McIntyre, 2017]. Second, the trajectories of the multi-compartment cable axons are based off of pathway reconstructions in the patient's head. Together, these

models calculate the theoretical response of pathways to the DBS voltage distribution using multi-compartment cable models of axons and are thus known as field-cable pathway-activation models (FC PAMs). In Chapter 2, we describe the latest evolution of these FC PAMs that incorporate patient-specific properties including the tissue conductivities and axonal trajectories within the head. In the remainder of this dissertation we use FC PAMs to investigate the pathways activated during therapeutic stimulation.

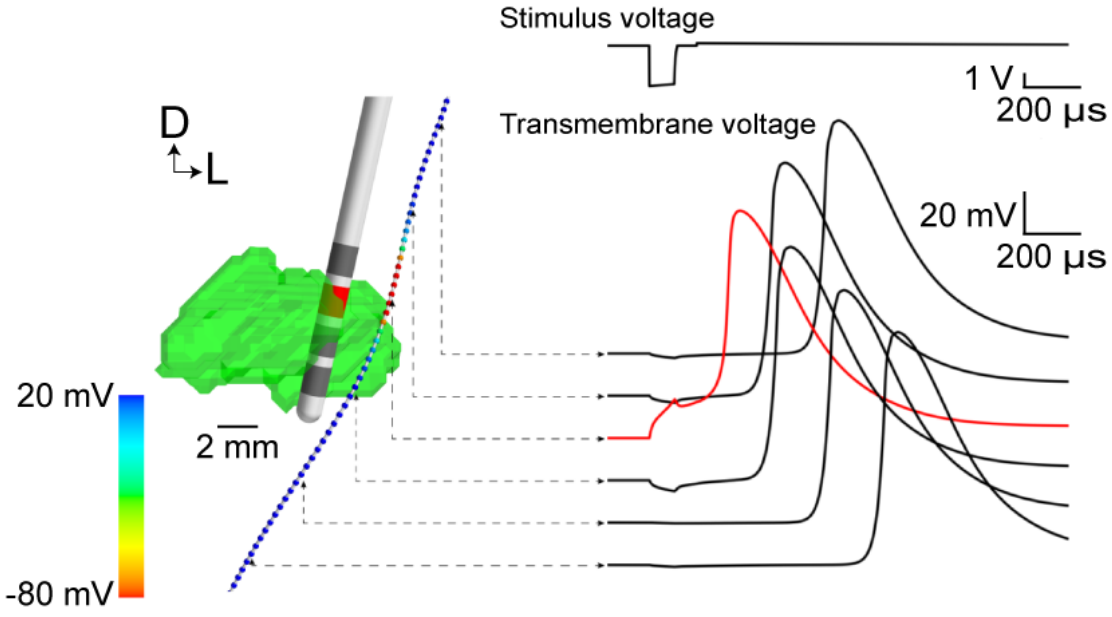

Figure 1.3. Field-cable pathway activation model. The deep brain stimulation (DBS) lead is implanted in the subthalamic nucleus (green). The DBS voltage distribution (not shown) is used to stimulate a multi-compartment cable model representation of an internal capsule axon and the response of this axon is quantified. This axon model generates a propagating action potential in response to the suprathreshold stimulus. Stimulation setting: contact 2 (-), case (+); 2.9 V; 90 µs; 130 Hz.

Solving the differential equations describing the nonlinear response of the transmembrane voltage to the applied DBS voltage distribution (Equation 1.1) is

a computationally intensive task. Thus, several studies have developed simplified methods for predicting the axonal response to stimulation, exploiting the theoretical observation that the change in the transmembrane voltage is related to the second spatial difference of the applied extracellular voltage along that element (Δ^2V_e, Equation 1.1) [McNeal, 1976; Rattay, 1986]. Such simplified methods include the driving force (DF) model [Warman et al., 1992; Peterson et al., 2011] and volume of tissue activated (VTA) model [Butson and McIntyre, 2006; Madler and Coenen, 2012; Chaturvedi et al., 2013; Astrom et al., 2015]. In Chapter 3, we evaluate these simplified methods for predicting axonal activation compared to the gold standard FC PAM in the context of subthalamic DBS.

1.4. Tractography

Tractography is a non-invasive method for reconstructing axonal pathways on a patient-specific basis. Tractography relies on diffusion-weighted (DW) MRIs that are acquired for each patient. A DW MRI provides a measurement of the diffusion of water in the brain. Tractography is based on the assumption that water is more likely to diffuse along the trajectories of anisotropic white matter [Moseley et al., 1990]. From a set of DW images measuring diffusion in at least six different directions, a model is created that describes diffusion on a voxel-by-voxel basis. The first such model was based on a tensor [Basser et al., 1994]. Alternative approaches have subsequently been described that effectively create probability distribution functions in each voxel to represent the likelihood of

diffusion in any given direction. One such alternative that we employ in this work was developed by Behrens et al. [2003; 2007].

Based on the voxel-wise diffusion models, streamline trajectories between different brain regions are calculated with a tractography algorithm. This process involves tracking from a seed region to a target region, based on the described diffusion direction in each voxel. With probabilistic tractography algorithms, the diffusion model probability distribution functions can be repeatedly sampled to capture the spatial spread in the distribution of streamline trajectories. Constraints can be placed on these algorithms such that the streamlines have to pass through waypoint regions and avoid exclusion regions. This results in the streamline trajectories theoretically representative of patient-specific axonal pathways between the seed and target regions. In our analysis, we used probabilistic tractography to reconstruct the internal capsule (IC), cerebellothalamic tract (CbTT), and medial lemniscus (ML) pathways. However, the trajectories of the tractography-based streamlines are very sensitive to the diffusion model, tractography algorithm, and input parameters [Behrens et al., 2007; Thomas et al., 2014]. As described in Chapter 4, probabilistic tractography was not able to generate anatomically realistic trajectories of the subthalamopallidal (SP) and lenticular fasciculus (LF) pathways and thus stylized representations were generated [Miocinovic et al., 2006].

1.5. Motivation

The axonal pathways in the subthalamic region that mediate the therapeutic response to DBS are not clearly defined. Patient-specific computational models can provide insights on the neurons directly modulated by DBS. These model results can be coupled with clinical measurements to get a better understanding of axonal pathways that when stimulated generate therapeutic effects or side effects. The aim of this dissertation was focused on constructing detailed patient-specific models of subthalamic DBS in PD patients and calculating the response of axons to therapeutic stimulation.

Previous studies have used computational models to provide insights on the pathways activated by STN DBS. Miocinovic et al. [2006] reconstructed the SP, LF, and IC pathways in two non-human primates implanted with DBS electrodes. They observed that increasing stimulation from a non-therapeutic amplitude to a therapeutic amplitude resulted in an increase in SP activation in both subjects, but an increase in LF activation in only one subject. Coenen et al. [2011] targeted stimulation to the CbTT pathway in a subject resulting in tremor cessation. Chaturvedi et al. [2012] explored the use of current steering with multiple independent sources to selectively activate either the SP or LF before activation of the IC. Since the time of these studies more information has been published in anatomical tracing studies regarding the trajectory of these and other pathways [Gallay et al., 2008; Kita and Kita, 2012; Haynes and Haber, 2013]. In addition to these developments, constraining an increased number of volume conductor model parameters has become a popular approach to

implementing these models [Howell and McIntyre, 2016; Howell and McIntyre, 2017].

1.6. Hypotheses

In this dissertation. we use patient-specific computational models to characterize activation of the SP, LF, IC, CbTT, ML, and hyperdirect (HD) pathways.

In Chapter 2, we provide a detailed description of the development steps for a patient-specific FC PAM. These FC PAMs account for the anatomical and biophysical details of each patient, and explicitly calculate the nonlinear axonal response to the DBS voltage distribution. Furthermore, the FC PAM presented here implements the latest advances in image processing, volume conductor modeling, and biophysical axonal stimulation modeling. Thus, this FC PAM represents the current gold standard for predicting axonal activation in humans. The workflow presented in this chapter is used for the construction of the FC PAMs in Chapters 3-5.

In Chapter 3, we compare the differences in axonal activation predictions between these detailed patient-specific DBS models (i.e. FC PAM) and simplified DBS models (i.e. VTA and DF). Our goal is to evaluate the accuracy of DF and VTA models compared to FC PAMs for DBS relevant parameters. We calculate the differences in stimulation thresholds and pathway activation between the FC PAM and the four predictors (DF-Peterson, VTA-Chaturvedi, VTA-Madler, VTA-Astrom) for a range of axon diameters (2 μm - 10 μm), stimulus pulse widths (30

μs - 120 μs), and electrode configurations (monopolar, bipolar, tripolar, quadripolar).

In Chapter 4, we calculate the axonal pathways activated by therapeutic subthalamic DBS in three PD patients using detailed patient-specific FC PAMs. We hypothesize that therapeutic stimulation (contact 2 [-], case [+]; 1-5 Volts; 60 μs; 130 Hz) in the subthalamic region selectively activates the HD and SP pathways, over the LF, CbTT, IC, and ML pathways.

In Chapter 5, we use a FC PAM to dissect the axons mediating short latency cortical evoked potentials during subthalamic DBS. These cortical evoked potentials have components that occur at 1.0 ms, 5.7 ms, and 22.2 ms after each stimulus pulse, which are referred to as R1, R2, and R3 respectively [Walker et al., 2012]. R1 is assumed to arise from antidromic invasion of layer V pyramidal neurons, R2 from intracortical synaptic activity, and R3 from orthodromic activity along the basal ganglia output nuclei. We construct a patient-specific FC PAM of the IC and HD pathways to verify the validity of these assumptions. We hypothesize that short latency responses at 1.0 ms in cortex are due to activation of hyperdirect axons. We stimulate in the subthalamic region and quantify the timings of action potentials arriving in cortex along these two pathways.

Chapter 2 – Creating and parameterizing patient-specific deep brain stimulation pathway-activation models

Gunalan K, Chaturvedi A, Howell B, Duchin Y, Lempka SF, Patriat R, Sapiro G, Harel N, McIntyre CC. Creating and parameterizing patient-specific deep brain stimulation pathway-activation models using the hyperdirect pathway as an example. PloS one. 2017 Apr 25;12(4):e0176132.

Abstract

Background: Deep brain stimulation (DBS) is an established clinical therapy and computational models have played an important role in advancing the technology. Patient-specific DBS models are now common tools in both academic and industrial research, as well as clinical software systems. However, the exact methodology for creating patient-specific DBS models can vary substantially and important technical details are often missing from published reports. **Objective**: Provide a detailed description of the assembly workflow and parameterization of a patient-specific DBS pathway-activation model (PAM) and predict the response of the hyperdirect pathway to clinical stimulation. **Methods**: Integration of multiple software tools (e.g. COMSOL, MATLAB, FSL, NEURON, Python) enables the creation and visualization of a DBS PAM. An example DBS PAM was developed using 7T magnetic resonance imaging data from a single unilaterally implanted patient with Parkinson's disease (PD). This detailed description implements our best computational practices and most elaborate parameterization steps, as defined from over a decade of technical evolution.

Results: Pathway recruitment curves and strength-duration relationships highlight the non-linear response of axons to changes in the DBS parameter settings. **Conclusion**: Parameterization of patient-specific DBS models can be highly detailed and constrained, thereby providing confidence in the simulation predictions, but at the expense of time demanding technical implementation steps. DBS PAMs represent new tools for investigating possible correlations between brain pathway activation patterns and clinical symptom modulation.

2.1. Introduction

Deep brain stimulation (DBS) is an established therapy for the treatment of movement disorders (e.g. essential tremor, Parkinson's disease (PD), and dystonia) and shows promise for the treatment of epilepsy and neuropsychiatric diseases (e.g. obsessive compulsive disorder, Tourette syndrome, and depression) (Lozano and Lipsman, 2013). Despite the growing clinical use of DBS, there is a paucity of knowledge on the neural response to the applied voltage distribution, and correlations linking the modulation of different brain pathways with clinical outcomes are lacking. Pathway-activation models (PAMs) are new scientific tools designed to help to address those knowledge gaps.

The motivation for creating PAMs comes from the clinical observation that accurate placement of the electrode within the target is a major determinant of therapeutic outcomes in DBS interventions (e.g. Welter et al., 2014; Eisenstein et al., 2014; Riva-Posse et al., 2014). However, a clear scientific definition of the "target" for each DBS therapy has been somewhat elusive. Experimental and

theoretical data suggest that axons are the most excitable neural elements to extracellular electrical stimulation (Ranck, 1975; McIntyre and Grill, 1999), and a primary effect of DBS is the generation of action potentials in axons (McIntyre et al., 2004; Miocinovic et al., 2006). Thus, irrespective of the neurological disorder under consideration, a growing consensus suggests that the target of the stimulation is likely to be axonal in nature (Gradinaru et al., 2009; Riva-Posse et al., 2014). However, the specific axonal pathways that are the explicit therapeutic targets for DBS are still under debate.

Given that a basic purpose of diffusion-weighted imaging (DWI) is to characterize axonal pathways in the brain, a burgeoning field of DBS research is now using DWI-based tractography to better understand the activated pathways (Coenen et al., 2012; Henderson, 2012). Numerous clinical studies have recently conducted tractography from voxels near DBS electrode contacts to identify potential axonal pathways that may be stimulated in disorders such as PD (Coenen et al., 2011), essential tremor (Klein et al., 2012), depression (Gutman et al., 2009), and epilepsy (Rossi et al., 2010). However, studies of this type commonly ignore the underlying biophysics of electrical stimulation when attempting to identify activated pathways. PAMs represent a methodology to explicitly calculate the axonal response to DBS, as well as its dependence on a number of factors that include: 1) the electrode configuration, 2) the shape, duration, and frequency of the applied stimuli, 3) the electrical conduction properties of the brain tissue medium, 4) the geometry and trajectory of the axons, and 5) the membrane biophysics of the axons.

We propose that accurate assessment of axonal activation requires modeling the direct application of the DBS voltage distribution on anatomically and biophysically accurate models of axons. Chaturvedi et al. (2010) and Lujan et al. (2012, 2013) demonstrated our first attempts at creating the conceptual basis of PAMs. These studies used medical images to locate the DBS electrode and model the voltage distribution generated in the patient's head. Then tractography was used to define the location and trajectory of axonal pathways surrounding the electrode. Finally, the DBS voltage distribution was used to stimulate cable models of individual axons. However, these first generation PAMs had very difficult software integration hurdles that exceeded what would be realistic for use in larger scale clinical analyses, as well as technical limitations in the volume conductor electric field models. Therefore, we worked to develop an improved workflow for constructing PAMs, and implemented numerous model parameterization steps that improve the detail and accuracy of the simulations. This manuscript describes how each step of the workflow comes together to create a PAM.

We present an example patient-specific PAM of unilateral subthalamic DBS that characterizes stimulation of two corticofugal pathways: 1) internal capsule fibers of passage, and 2) the hyperdirect pathway. Layer V pyramidal neurons send projections via the internal capsule to the brainstem and spinal cord. Of these projections, 5-10% give off a collateral to the subthalamic nucleus (STN) and are collectively known as the hyperdirect pathway (Nambu et al., 2002; Kita and Kita, 2012; Haynes and Haber, 2013). Electrical (Li et al., 2007;

Li et al., 2012) and optogenetic (Gradinaru et al., 2009; Sanders and Jaeger, 2016) stimulation of the hyperdirect pathway has been directly linked to therapeutic benefit in rodent models of PD. In addition, human experiments have supported the hypothesis that DBS of the hyperdirect pathway is related to symptom relief (Walker et al., 2012; Whitmer et al., 2012). In contrast, direct activation of internal capsule fibers of passage is known to generate muscle contraction side effects (Tommasi et al., 2008). Therefore, we use our PAM example to demonstrate the different DBS recruitment characteristics of these two clinically relevant pathways.

2.2. Materials and Methods

2.2.1. Ethics statement

Collection of all patient data for this study was approved by the University of Minnesota Institutional Review Board (IRB). The patient provided informed written consent prior to participating in the research and this consent procedure was approved by the IRB.

2.2.2. Patient data

The imaging data was acquired from a 67-year old right-handed male diagnosed with PD for ~11 years. A Medtronic 3389 DBS lead was implanted in the left STN and connected to an Activa SC implantable pulse generator (IPG) (Medtronic, Minneapolis, MN). Using standard clinical programming procedures (Volkmann et al., 2002), the following therapeutic stimulation parameters were

selected: monopolar configuration with contact 2 as the cathode and the IPG case as the anode, pulse amplitude of 1.7 V, pulse width of 60 μs, and pulse frequency of 130 Hz. His OFF medication, OFF stimulation motor subscore of the Unified Parkinson's Disease Rating Scale was 31, and the ON medication, ON stimulation score was 14. The impedance measured by the IPG at contact 2 was 1450 Ω, which is the dynamic load of the circuit as defined at 70 μs into the stimulus pulse (Appendix B).

2.2.3. Workflow overview

The general workflow required to create a PAM is outlined in Fig 2.1 and detailed in the following sections. First, we acquired, pre-processed, and co-registered the patient's imaging data (Section 2.2.4 and Appendix B). Second, we calculated the voltage distribution generated by the DBS electrode (Section 2.2.5). Third, we constructed multi-compartment cable axon models whose trajectories were based on tractography reconstructions of axonal pathways of interest near the DBS electrode (Section 2.2.6). Fourth, we used the DBS voltage distribution to stimulate the model axons and quantified their response (Section 2.2.7).

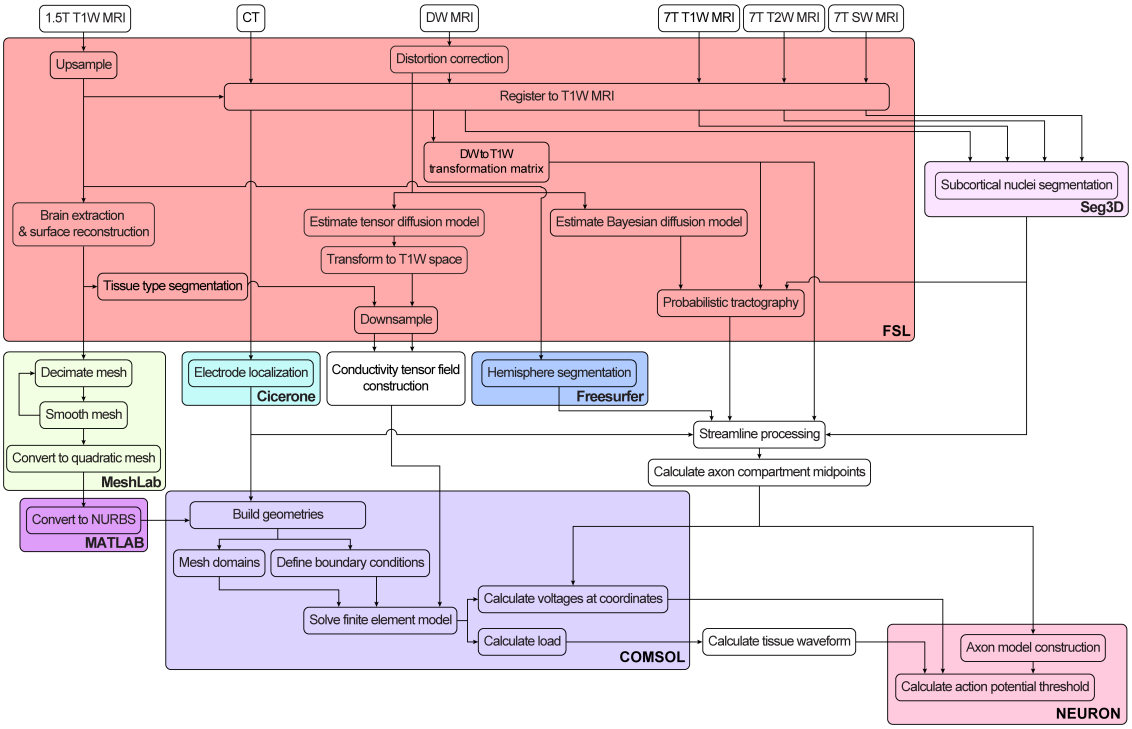

Figure 2.1. Scientific workflow for development of pathway-activation models. Color shading corresponds to the software program used for each step. Patient images are processed and tractography is performed in FSL (red). The finite element model is constructed and solved in COMSOL (purple). The axon model is constructed and the threshold stimulus amplitude for action potential generation is solved for in NEURON (pink). We automated many of the steps using custom MATLAB, Python, NEURON, and Bash scripts.

2.2.4. Image acquisition

The patient underwent pre-operative scanning on a 7T magnetic resonance imaging (MRI) system (Magnex Scientific, UK) at the Center for Magnetic Resonance Research (CMRR) at the University of Minnesota, using T1-weighted (T1W), T2-weighted (T2W), susceptibility-weighted (SW), and diffusion-weighted (DW) imaging (Appendix B). We also obtained a pre-operative T1W image on a 1.5T Siemens Magnetom Espree. A post-operative CT image was acquired on a Siemens Biograph64 Sensation approximately 1 month after the DBS surgery.

2.2.5. DBS voltage distribution

The voltage distribution generated by the DBS electrode varies both spatially and temporally in the tissue medium (Fig 2.2 and Fig 2.3). The conductance and permittivity of the tissue medium and electrode-tissue interface (ETI) affect the voltage distribution generated within the head. Temporally, the stimulus waveform generated by the IPG consists of a cathodic phase, interphase interval, passive recovery phase, and interpulse interval (Fig 2.3F). For a given set of stimulation parameters, we used a four-step approach to approximate the voltage distribution generated by the DBS electrode as a function of space and time (Equation 2.1) (Butson and McIntyre, 2005; Miocinovic et al., 2009; Howell and McIntyre, 2016; 2017):

Equation 2.1. DBS voltage distribution.

$$\Phi(\mathrm{x},\mathrm{y},\mathrm{z},\mathrm{t}) = \Phi(\mathrm{x},\mathrm{y},\mathrm{z},\mathrm{t}=0) * \mathrm{A} * \mathrm{V}_{\mathrm{tissue}}(\mathrm{t})$$

First, we calculated the static solution of the voltage distribution in the tissue medium, $\Phi(\mathrm{x},\mathrm{y},\mathrm{z},\mathrm{t}=0)$ (Fig 2.3E and Section 2.2.5.1). The voltage on the electrode surface was set to -1 V with respect to ground, which was defined at the base of the neck and set to 0 V (Fig 2.2D) (Walckiers et al., 2010). Second, because the differential equation solved is linear, we scaled the voltage distribution by the stimulus amplitude, A, under investigation. Third, to account for the filtering effects of the IPG circuitry, lead wires, and the ETI on the DBS waveform “seen” by the tissue, we calculated the tissue voltage over time,

$V_{tissue}(t)$, with an equivalent electrical circuit of the implanted DBS system (Fig 2.3F and Appendix B and Section 2.2.5.2). Finally, the extracellular voltage distribution is scaled by the tissue waveform at each time step, $\Phi(x, y, z, t)$. This process is described in further detail in the following sections.

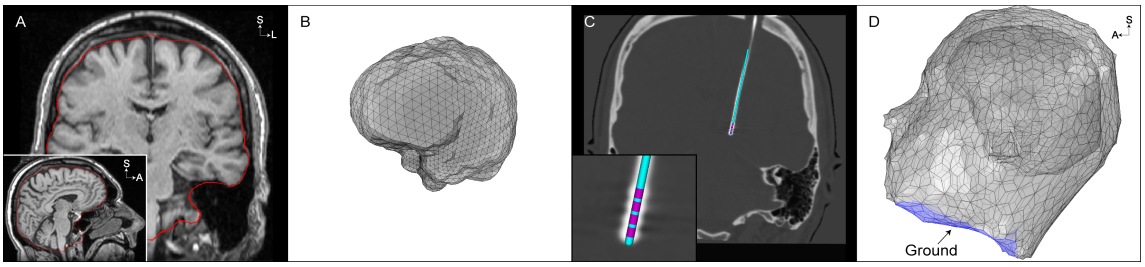

Figure 2.2. Finite element model boundaries. **(**A) The non-skull stripped 1.5T T1-weighted (T1W) image is used to extract the inner skull surface (red). (B) Inner skull surface mesh from (A) prior to any processing. (C) An oblique coronal view of the post-operative CT image, co-registered to the pre-operative T1W image, that is used to localize the four collinear electrode contacts. The inset shows the artifact of the 4 electrode contacts and a 3-dimensional rendering of the model Medtronic 3389 DBS electrode fit to the electrode artifact. (D) Domains of the finite element model, including the electrode, brain, and head. The neck region of the head surface mesh is set to 0 V under the monopolar configuration (blue).

2.2.5.1. Spatial characteristics

We calculated the voltage distribution generated in the tissue medium, $\Phi(x, y, z, t = 0)$, for monopolar cathodic stimulation delivered through contact 2. Laplace's equation was solved using an electrostatic finite element model (FEM) in COMSOL. We constructed the FEM using the following five steps. First, we constructed volumes representing a Medtronic 3389 DBS electrode, an encapsulation layer surrounding the electrode, and domains of the brain and head. Each electrode contact was modeled as a cylindrical surface, with 1.5 mm length and 0.5 mm spacing between contacts. The length of the

entire electrode shaft was 60 mm but did not pass outside the brain domain. We modeled the encapsulation layer with a radius of 0.5 mm along the entire length of the electrode shaft. Surface meshes representing the inner skull and outer head surfaces were constructed (Fig 2.2A/B and Appendix B) and imported into COMSOL to define volumes of the brain and head (Fig 2.2D).

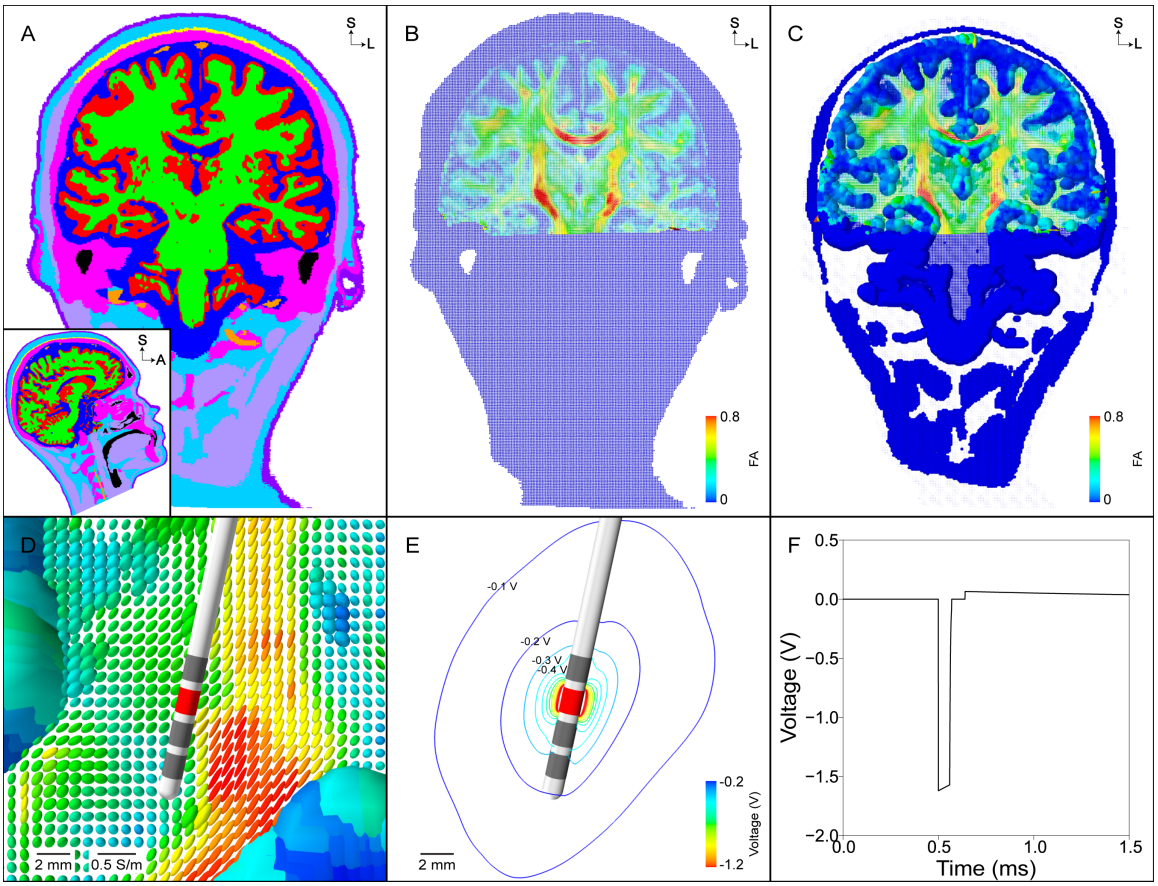

Figure 2.3. Finite element model and DBS voltage distribution. (A) Segmentation of the head into different tissue types (grey matter – red, white matter – green, cerebrospinal fluid – dark blue, muscle – light purple, tendon – yellow, bone – pink, fat – light blue, skin – dark purple, intervertebral disks – not visible, blood – orange, air – black). (B) Conductivity tensors within the head normalized by their volume. Anisotropic conductivity tensors are constructed within the brain using the eigenvectors of the diffusion tensors and a scalar mapping of the diffusion eigenvalues. Each tensor is colored according to its fractional anisotropy. (C) Same tensors from (B) but scaled so that the relative differences in conductivities can be visualized. (D) Zoomed view of tensors from (C) near the DBS electrode. (E) Isolines of the voltage distribution generated by a -1.7 V stimulus at contact 2. (F) The stimulus waveform at the electrode-tissue interface generated by the implantable pulse generator.

Second, we defined a conductivity tensor field within the head (Appendix B). The tensor field outside of the brain was isotropic, and was anisotropic within the brain. Within the brain, we defined symmetric conductivity tensors using a load preservation approach that was based off of the patient-specific diffusion tensor data (Howell and McIntyre, 2016). We defined the isotropic conductivity of the encapsulation layer so that the model impedance matched the clinically-measured impedance (Appendix B). To do so, we varied the encapsulation layer conductivity between 0.05 – 0.2 S/m (Grill and Mortimer, 1994; Butson et al., 2006), and then calculated the model impedance by replicating the impedance measurements of the Medtronic programming device.

Third, we defined Dirichlet boundary conditions of -1 V at contact 2 and 0 V at the neck region of the head surface (Fig 2.2D). The inactive contacts were modeled using boundary conditions, and the electrode shaft (except for the contacts) and head surface (except for the neck region) were modeled as perfect insulators (Appendix B). Fourth, we generated a multi-resolution, tetrahedral volume mesh between the outer boundary of the DBS electrode and the inner boundary of the outer head (Appendix B). Fifth, we solved the model to calculate the voltage distribution, $\Phi(\mathrm{x}, \mathrm{y}, \mathrm{z}, \mathrm{t} = 0)$ (Fig 2.3E).

2.2.5.2. Temporal characteristics

We calculated the temporal modulation of the voltage distribution using an equivalent electrical circuit model for voltage-regulated, monopolar stimulation (Appendix B). The equivalent electrical circuit model included representations of

the blocking capacitors (10 μF), extension wire and lead wire resistances (55 Ω), ETI with a double-layer capacitance and Faradaic resistance in parallel, and tissue resistance. The distributed values of the double-layer capacitance and Faradaic resistance of the ETI were 30 $\mu F/cm^2$ and 150 Ωcm^2, respectively, which equated to lumped values of 1.8 μF and 2.5 kΩ (Wei and Grill, 2009). We ignored the tissue capacitance because the double-layer capacitance is approximately two orders of magnitude larger than the tissue capacitance (Butson and McIntyre, 2005; Howell and McIntyre, 2016). The access resistance of our electrostatic FEM (i.e. tissue resistance) with contact 2 set as the working electrode was 1373 Ω (Appendix B). A 'parasitic' capacitance (3 nF) and 'parasitic' resistance (20 kΩ) were included in parallel with the load of the DBS system so the voltage waveform generated across the tissue resistance had decay characteristics during the interphase interval that matched the measured waveform from the output of a Medtronic IPG (data not shown).

The voltage waveform generated across the tissue resistance (i.e. tissue waveform) was calculated for an applied rectangular pulse train (Fig 2.3F). For each pulse, the applied rectangular waveform consisted of a cathodic phase, interphase interval, passive recovery phase, and interpulse interval. The tissue waveform, $V_{tissue}(t)$, was calculated by applying Kirchhoff's current law to the equivalent circuit model and using forward Euler numerical time integration to solve the ordinary differential equations. Finally, we scaled the extracellular voltage distribution, $\Phi(x, y, z, t = 0)$, by the tissue waveform, $V_{tissue}(t)$, at each

time step to calculate the temporal aspects of the voltage distribution, $\Phi(x, y, z, t)$ (Appendix B).

2.2.6. Axon model

We constructed multi-compartment cable models of myelinated axons to represent the hyperdirect pathway, as well as internal capsule fibers of passage, in NEURON (Fig 2.4). Both pathways consisted of a corticofugal axon passing through the internal capsule. The models representing the hyperdirect pathway where unique in that they had an axon collateral that branched from the corticofugal axon and terminated in the STN (Kita and Kita, 2012; Hayes and Haber, 2014).

We used probabilistic tractography to define the trajectory of each corticofugal axon (Fig 2.4B). FSL's probabilistic tractography tool (`probtrackx`) generated trajectories, or 'streamlines', which originated in the seed mask and terminated in the target masks (Appendix B). Of the 13,219 corticofugal streamlines that were reconstructed with probabilistic tractography, we randomly sampled 2,000 for use in our models. One thousand streamlines were used to model the internal capsule fibers of passage, and the other 1,000 streamlines were designated to the hyperdirect pathway. We fit a smoothing spline to each tractography-generated streamline to ensure a smooth trajectory for each streamline (Fig 2.4C and Appendix B).

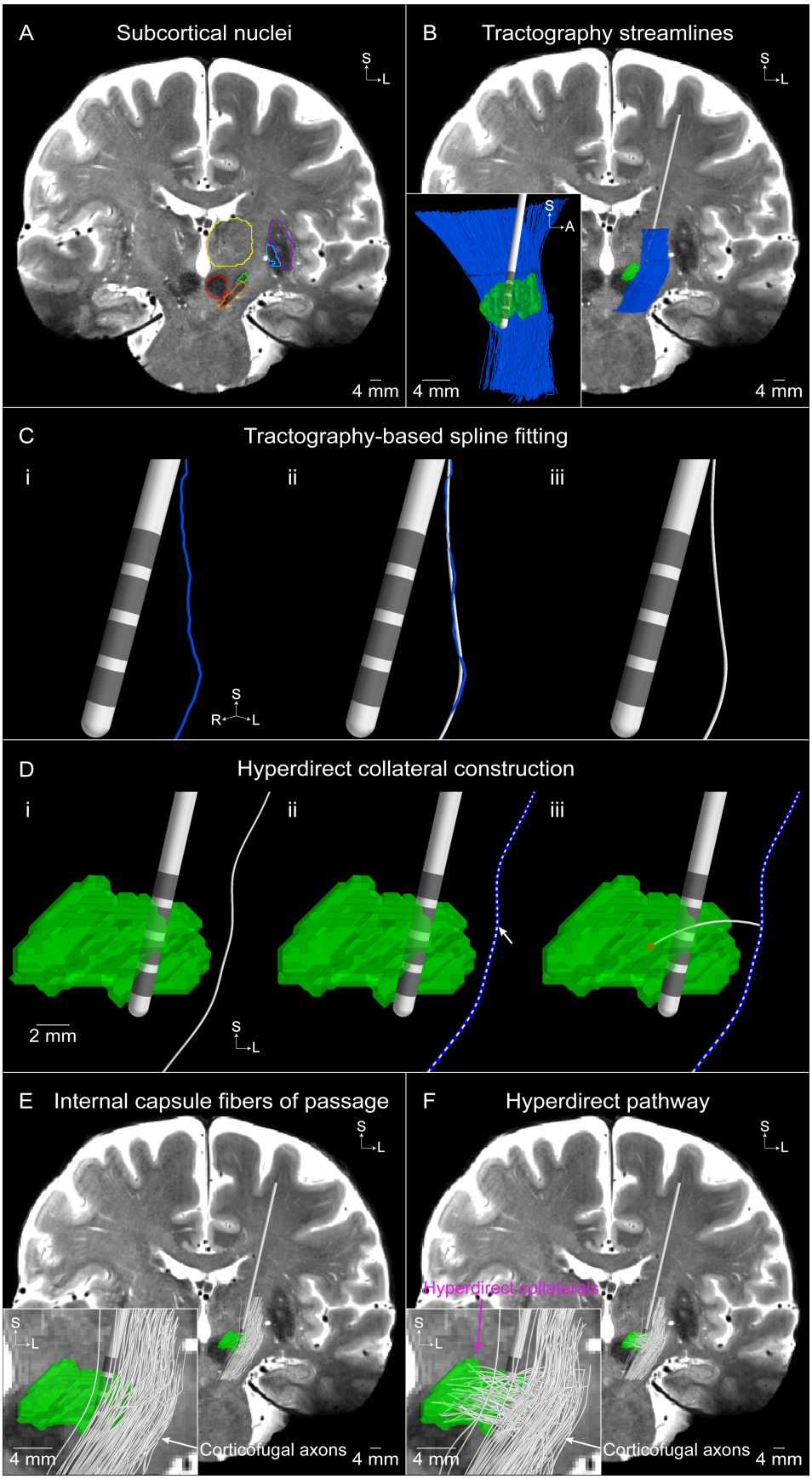
A
Subcortical nuclei
S
L
4 mm
B
Tractography streamlines
S
A
4 mm
4 mm
C
Tractography-based spline fitting
i
ii
iii
S
R
L
D
Hyperdirect collateral construction
i
ii
iii
2 mm
S
L
E
Internal capsule fibers of passage
S
L
S
L
4 mm
Corticofugal axons
4 mm
F
Hyperdirect pathway
S
L
Hyperdirect collaterals
S
L
4 mm
Corticofugal axons
4 mm

Figure 2.4. Tractography-based axon model of the hyperdirect pathway and internal capsule fibers of passage. (A) Subcortical nuclei outlined on the T2-weighted coronal image (subthalamic nucleus [STN] – green, substantia nigra – orange, red nucleus – red, thalamus – yellow, putamen – purple, globus pallidus externus – light blue, globus pallidus internus – dark blue). (B) Tractography-generated corticofugal streamlines. Inset is a sagittal view of the resulting streamlines. (C) A smoothing spline (white) is fit to an example tractography-generated streamline (blue). (D) The hyperdirect pathway axon is comprised of a collateral that branches off of a (i) corticofugal axon at a (ii) node of Ranvier (blue spheres) and (iii) terminates in a random voxel (red) within the STN. An example population of (E) 100 internal capsule fibers of passage and (F) 100 hyperdirect pathway axons. The inset in (F) shows that each hyperdirect pathway axon is comprised of a corticofugal axon with a branching collateral that terminates within the STN, whereas the inset in (E) shows that the internal capsule fibers of passage do not have a collateral.

For the hyperdirect pathway axons, we modeled the collateral as a branch at a randomly chosen node of Ranvier along the corticofugal axon that was within the axial bounds of the STN (Fig 2.4D). A random voxel within the STN was selected as the termination point of the collateral. We then generated an arc connecting the branch point node of Ranvier and the termination point within the STN to define the collateral trajectory. If the collateral passed through the DBS electrode, we randomly selected a different voxel within the STN and recalculated the corresponding arc.

The geometric and electrical parameters of the corticofugal axons were defined from previously established models (McIntyre et al., 2002). The myelinated axon was modeled with a double cable structure and the nodes of Ranvier contained active (i.e. voltage-gated fast Na^+, persistent Na^+, and slow K^+ ion channel conductances) and passive (i.e. leak conductance, capacitance) membrane properties. The axon model compartments of the corticofugal axons were defined with a myelin diameter of 5.7 μm and the hyperdirect collaterals

were defined with a myelin diameter of 1.8 μm. We divided each corticofugal axon into compartments (node of Ranvier, MYSA, FLUT, STIN) and calculated the coordinates of each compartment along the arc length of the streamline. The coordinates of each compartment for the hyperdirect collateral were defined in the same manner as the corticofugal axon. We shortened the collateral's first node of Ranvier to 0.5 μm and shortened the distal end of the collateral so that it ended with a node of Ranvier. The terminal node was assigned passive membrane properties to minimize any role as a hyperexcitable locus for action potential initiation (McNeal, 1976).

2.2.7. Axon model stimulation

The response of each individual axon model to the spatially- and temporally-varying DBS voltage distribution, $\Phi(x, y, z, t)$, was calculated with NEURON (Appendix B) (Hines and Carnevale, 2001). For each pulse width (20-120 μs), with contact 2 set as the cathode and the IPG case set as the anode, we used a binary search algorithm to determine the stimulus amplitude, A, that was sufficient for generating propagating action potentials. The threshold stimulus amplitude was calculated to within 0.01 V. The axons were stimulated with 3 pulses and the criteria for activation was that the distal active nodes of Ranvier on the corticofugal axon had to generate a 1-to-1 response to each stimulus pulse. For both the internal capsule fibers of passage and hyperdirect pathway axons, we excluded axons from subsequent analyses that had thresholds greater than or equal to 150 V or initiated action potentials in the distal active nodes of

Ranvier on the corticofugal axon. This resulted in 989 internal capsule fibers of passage and 1000 hyperdirect pathway axons. Subsequently, each of these axons for a given pathway were clustered randomly into 100 populations of 1000 axons in a bootstrapping manner (with replacement), to quantify the effects of variability in the distribution of the axon trajectories. The average and standard deviation of the number of activated axons for the 100 populations in response to a specific stimulation amplitude are presented.

We systematically changed several simulation parameters to ensure that the results converged on an accurate solution. The differences in stimulation threshold amplitudes for axons of the internal capsule fibers of passage were calculated. Two different analyses were performed: 1) we increased the mesh resolution in COMSOL from 1,429,416 to 2,347,048 tetrahedral elements; and 2) we decreased the time step in NEURON from 1 μs to 0.5 μs. Each of these changes resulted in less than 1.2% differences in the stimulation thresholds.

2.3. Results

PAMs are the integrated processing of imaging data from DBS patients with tractography and electrical stimulation modeling to provide a theoretical estimate of axonal pathway activation. In this study, we generated an example PAM using high-field (7T) MRI data to construct the patient model (Lenglet et al., 2012). These images have higher signal-to-noise, voxel resolution, and contrast than the 1.5T or 3T MRIs typically collected for clinical DBS procedures (Duchin et al., 2012).

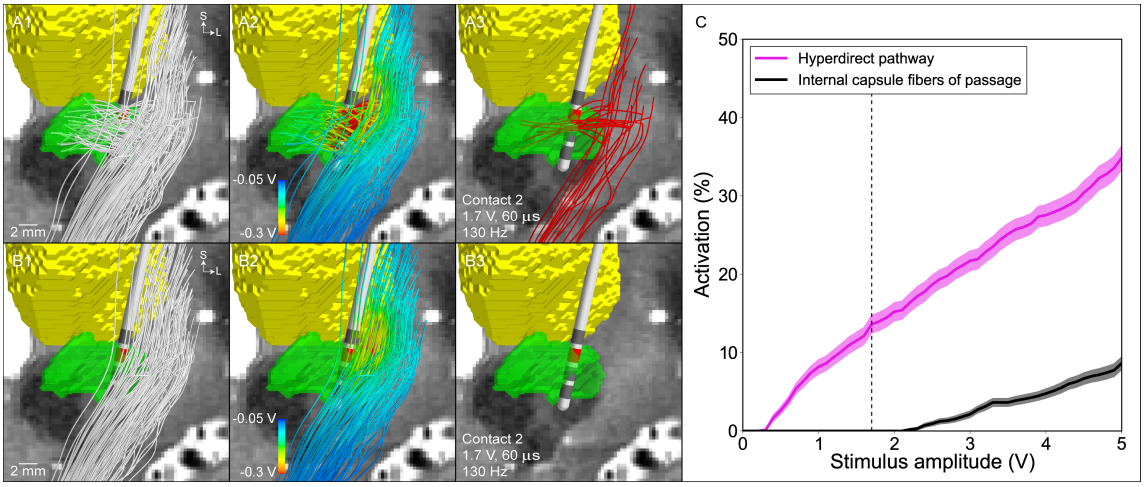

Figure 2.5. Model predictions for the activation of the hyperdirect pathway and internal capsule fibers of passage. Representative population of (A1) 100 hyperdirect pathway axons and (B1) 100 internal capsule fibers of passage (subthalamic nucleus – green, thalamus – yellow). (A2), (B2) The voltage distribution generated by -1.7 V applied at contact 2 is interpolated along the streamlines. (A3), (B3) The voltage distribution is used to stimulate the axon models, and those axons that are activated by the clinically effective stimulation setting (-1.7 V, 60 µs, 130 Hz) are shown in red. (C) Percent activation of each pathway as a function of the stimulation amplitude (contact 2 [cathode], IPG case [anode], 60 µs, 130 Hz). The dashed vertical line is the clinically effective stimulation amplitude.

We designed the patient-specific PAM to enable comparison of the DBS-induced activation of two sets of corticofugal axonal pathways. One set represented the hyperdirect pathway and the other represented the internal capsule fibers of passage. The activation of both pathways was calculated as a function of stimulation amplitude (Fig 2.5). At the clinically effective stimulation setting (contact 2 [cathode], IPG case [anode], 1.7 V, 60 µs, 130 Hz), the model predicted 13.6 ± 1.2% activation of the hyperdirect pathway and 0 ± 0% activation of the internal capsule fibers of passage (Appendix B).

The model predictions corresponded well with the clinical hypothesis that the hyperdirect pathway is directly activated during therapeutic subthalamic DBS. The steep slope of the hyperdirect recruitment curve also supports the clinical hypothesis that the degree of hyperdirect pathway activation is proportional to the degree of therapeutic benefit (Walker et al., 2012). However, hyperdirect pathway activation is constrained by stimulation spread into the internal capsule fibers of passage. Significant activation of these internal capsule fibers of passage is known to generate unwanted side effects (Tommasi et al., 2008). Previous electromyography-based estimates for DBS-induced muscle contractions have suggested that side effects begin to occur at ~10% activation of the internal capsule fibers of passage (Chaturvedi et al., 2010).

A key concept in the clinical implementation of DBS is the "therapeutic window," i.e. the stimulation amplitude range between the onset of therapeutic effects and the generation of side effects (Volkmann et al., 2002). Typically, the electrode contact with the largest therapeutic window is the contact selected for chronic stimulation. Given that good therapeutic effects were generated in our example patient with ~15% activation of the hyperdirect pathway, we then quantified the stimulus amplitudes necessary to activate 15 ± 5% of the hyperdirect pathway as a function of the stimulus pulse width; thereby creating a hyperdirect strength-duration curve (Fig 2.6A). A similar internal capsule fibers of passage strength-duration curve was also generated for 10 ± 5% activation.

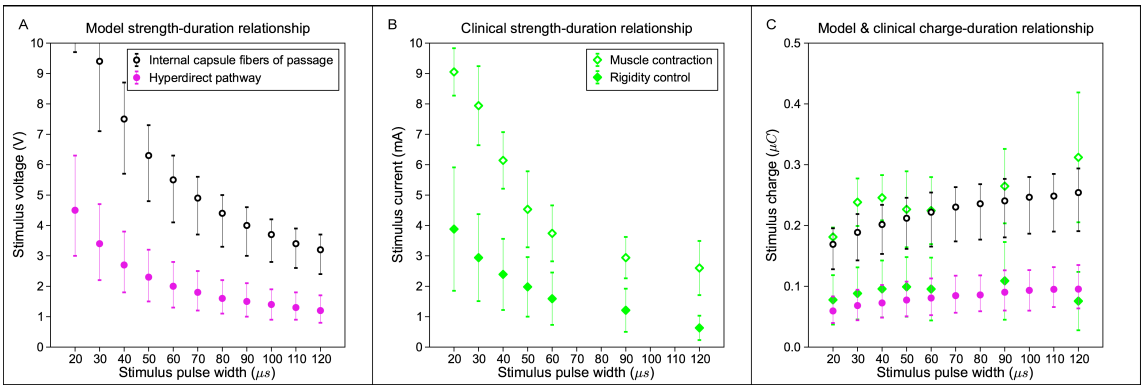

Figure 2.6. Model and clinical strength-duration and charge-duration curves. (A) Model threshold amplitudes for activation of the hyperdirect pathway (pink filled circle) and internal capsule fibers of passage (black open circle) at 15 ± 5% and 10 ± 5%, respectively. (B) Clinically-measured threshold amplitudes for DBS-induced rigidity control (green filled diamond) and muscle contractions (green open diamond) (Reich et al., 2015). (C) Total charge injected during the cathodic phase of the stimulus for the threshold amplitudes shown in A and B.

The results show that the amplitude window between direct activation of the hyperdirect pathway and the internal capsule fibers of passage increases with decreasing pulse width (Fig 2.6A). This theoretical calculation provides a possible biophysical explanation for the typical clinical practice of using short pulse widths to increase the therapeutic window (Rizzone et al., 2001). In addition, our theoretical results, albeit from a single patient, match well with the strength-duration curves for clinically measured, DBS-induced rigidity control and muscle contractions (Fig 2.6B) (Reich et al., 2015). To more directly compare the model and clinical strength-duration curves, which were generated with voltage-controlled and current-controlled IPGs, respectively, we plotted the results from Fig 2.6A/B as charge-duration curves (Fig 2.6C). The total charge injected during the cathodic phase of the stimulus was calculated with trapezoidal numerical integration for the stimulus amplitudes in Fig 2.6A/B. Of particular note

was the tight congruence of the theoretical hyperdirect activation with clinical measurements on the control of rigidity (Fig 2.6C).

2.4. Discussion

This manuscript provides a detailed description of the technical steps to construct a patient-specific PAM. PAMs represent a new scientific tool for integrating brain mapping connectomics with the computational neuroscience of electrical stimulation modeling. An obvious application of PAMs is in the field of clinical DBS, where the concepts of pathway-targeted neuromodulation for the control of specific symptoms are currently under intense clinical investigation.

2.4.1. Next generation models of DBS

Over the last two decades, the clinical applications of DBS have evolved from a focus on movement disorders to expanded opportunities in treating psychiatric disorders and epilepsy. A common feature that potentially links these various disorders are the existence of dysfunctional brain circuit oscillations that can be overridden by direct extracellular stimulation of axonal pathways (Lozano and Lipsman, 2013). In turn, the application of DBS to brain circuit modulation presents an exciting opportunity to leverage the massive scientific efforts currently underway to map the human connectome (e.g. Van Essen et al., 2013; Setsompop et al., 2013). However, most connectome-type projects rely on data derived from healthy subjects, whereas DBS is implemented in patients with neurological disorders, who have putative differences in their brain anatomy and

axonal connections. In addition, we propose that an important aspect of integrating tractography with DBS modeling is to define methods that accurately predict the biophysical response of specific axonal pathways to electrical stimulation.

A key component of PAMs are the use of multi-compartment cable axon models to quantify the neural response to DBS. This is in contrast to more simplistic approaches to estimate brain regions where DBS-induced action potentials are likely to occur via activation volume predictor functions (e.g. Chaturvedi et al., 2013). Only PAMs explicitly represent the transmembrane currents generated by extracellular stimulation, which are responsible for inducing membrane depolarization in the neural compartments closest to the active cathodic electrode contact (McNeal, 1976). These stimulation-induced inward currents open sodium channels, and if the polarization is sufficiently strong, an action potential will be generated. However, a wide range of factors dictate DBS-induced action potential generation including: 1) the electrode configuration, 2) the shape, duration, and frequency of the applied stimuli, 3) the electrical conduction properties of the brain tissue medium, 4) the geometry and trajectory of the axons, and 5) the membrane biophysics of the axons. In our experience, the most anatomically and electrically accurate method currently available to account for those various factors is a PAM.

In addition to PAMs, activation volume tractography (AVT) represents an alternative method to link tractography and stimulation. New academic software tools such as DBSproc (Lauro et al., 2016) and Lead-DBS (Horn and Kuhn,

2015) facilitate the creation of AVT models. In general, both PAMs and AVT use similar methods to construct a patient-specific model of the anatomy and the DBS electrode location. The major differences reside in the methodology for predicting axonal pathway activation. AVT defines an activation volume around the DBS electrode contact and then uses the voxels contained within that activation volume as seeds for tractography. AVT can help identify pathways of interest in a DBS therapy, but is prone to generating erroneous results (e.g. anatomically nonexistent pathways) (Behrens et al., 2007). Alternatively, PAMs use tractography to define known anatomical pathways of interest a priori, and then calculates the biophysical response of those pathways to electrical stimulation. However, relative to AVT, PAMs are more difficult to develop and analyze. We propose that each method has its own merits and value, with the major comparison being speed and simplicity for AVT versus anatomical detail and biophysical realism for PAMs.

2.4.2. DBS modeling in clinical research

While connectome-based DBS modeling is still in its infancy, the applications for clinical investigation have already been numerous. DBS for depression represents one of the most active areas of investigation, with studies addressing the potential pathways directly activated by DBS (Johansen-Berg et al., 2008; Lujan et al., 2012; Lujan et al., 2013), differences in pathway activation between alternative surgical targets (Gutman et al., 2009), prospective identification of novel surgical targets (Schlaepfer et al., 2013), and probabilistic

identification of pathways related to therapeutic benefit (Riva-Posse et al., 2014). Similarly, wide-ranging efforts are currently underway in movement disorders, with numerous recent examples focused on the development of correlations between stimulation of various pathways and the control of tremor (Coenen et al., 2011; Klein et al., 2012; Groppa et al., 2014; Sweet et al., 2014).

The results of this study provide theoretical insight into stimulation of the hyperdirect pathway during subthalamic DBS. Activation of the hyperdirect pathway has been hypothesized to be related to improvements in rigidity (Butson et al., 2011). Our patient-specific biophysical branching model of hyperdirect collaterals in the STN provided an opportunity to more directly address that hypothesis (Fig 2.6), which necessitated a more anatomically realistic model than previous attempts to reconstruct the hyperdirect pathway (Aravamuthan et al., 2007; Whitmer et al., 2012; Brunenberg et al., 2012; Kang and Lowery, 2014). This is because both the complex axonal trajectory and branching impact the activation threshold from extracellular stimulation (McNeal, 1976). The model results demonstrate robust activation of the hyperdirect pathway at the clinical stimulation setting in our example patient (Fig 2.5). We also observed strong congruence between strength-duration curves for activation of the hyperdirect pathway in our model and population averages of clinically-measured rigidity control from DBS (Fig 2.6). These results support the concept that future PAM analyses, applied to a population of DBS patients, may help in identifying correlations between direct activation of a particular pathway and modulation of a clinical symptom.

2.4.3. Study limitations and future work

The PAM created for this study represents a highly detailed patient-specific DBS computational model. However, as with any model, multiple limitations and caveats exist. PAMs are able to predict the direct activation of individual axonal pathways to a stimulus pulse, but it should be noted that PAMs do not quantify the network-level modulatory effects of DBS. However, such questions may eventually be addressed by the future combination of PAMs with large-scale network activity models (Hahn and McIntyre, 2010).

Image registration and definition of the DBS electrode location in the brain represent some of the most important sources of error in creating patient-specific DBS models. We used established registration algorithms to transform the 7T images, 1.5T image, and CT image to a common coordinate system (Duchin et al., 2012), and registration quality was verified using visual inspection to ensure that the subcortical and cortical boundaries aligned. In addition, we used established methods to minimize error in alignment of a model DBS electrode to the electrode artifact in the CT (Hemm et al., 2009).

Once the image pre-processing is complete, the patient-specific FEM and tractography-based axon models can be integrated together. While DBS FEMs are only an approximation of a highly complex phenomenon (Butson et al., 2007), they are able to match *in vivo* experimental recordings of the voltage distribution in the brain with impressive fidelity (Miocinovic et al., 2009). However, our latest advances in DBS FEM parameterization reinforce the importance of

incorporating all of the electrical details described in our PAM workflow to generate the most accurate results (Howell and McIntyre, 2016; 2017).

The multi-compartment cable models of axons we used were stylized to a single diameter and ignore some of the complex branching patterns of real axons (Kita and Kita, 2012; Haynes and Haber, 2013). These biophysical limitations are also coupled to the general limitations of tractography, which are well documented elsewhere (Jones et al., 2013) and are directly applicable to its use in PAMs. Nonetheless, tractography does represent the only non-invasive method to reconstruct structural connectivity on a patient-specific basis (Van Essen et al., 2013).

One area of necessary future development is refinement to the pathway reconstruction techniques and biophysical axon models. In the case of the hyperdirect pathway, as the collaterals terminate near the active DBS electrode contacts, consideration should be taken regarding the termination points of the streamlines. We initially attempted to use tractography to reconstruct the hyperdirect terminations within the STN (Aravamuthan et al., 2007; Brunenberg et al., 2012; Petersen et al., 2016); however, the reconstructions through the grey matter were very tortuous and anatomically unrealistic. Anatomical tracing studies have shown that the hyperdirect pathway often branches upon entering the posterio-dorso-lateral aspect of the STN and collaterals terminate throughout the STN (Parent and Hazrati, 1995; Nambu et al., 2002; Kita and Kita, 2012; Haynes and Haber, 2013). Additionally, studies have shown that the hyperdirect collaterals are typically less than 1 μm in diameter (Kita and Kita, 2012; Mathai et

al., 2013). And in the human internal capsule, there is a wide range of axon diameters from <1-10 μm (Graf von Keyserlingk and Schramm, 1984; Firmin et al., 2014). Each of these anatomical details will affect the predictive power of the model and represent opportunities for future improvement.

2.5. Conclusions

PAMs represent advanced computational tools with potential to augment clinical investigations on the mechanisms of DBS. The functional goal of PAMs is to provide quantitative patient-specific predictions on the axonal pathways directly activated by DBS, and then enable linkage of those pathway activation metrics to clinical outcome measures associated with specific symptoms. In addition, PAMs could one day be coupled with functional neuroimaging to help investigate the network-level neuromodulatory effects of DBS (e.g. Kahan et al., 2014; Fox et al., 2014).

Chapter 3 – Comparison of methods for quantifying axonal responses in patient-specific models

Abstract

Medical imaging has played a major role in defining the general anatomical targets for deep brain stimulation (DBS) therapies. However, specifics on the underlying brain circuitry that is directly modulated by DBS electric fields remain relatively undefined. Detailed biophysical modeling of DBS provides an approach to quantify the theoretical responses to stimulation at the cellular level, and has established a key role for axonal activation in the therapeutic mechanisms of DBS. When coupled with advances in defining the structural connectome of the human brain, axonal pathways activated by DBS can be simulated within the broader context of the brain circuitry and correlated with clinical outcomes. These pathway-activation models (PAMs) represent powerful tools for DBS research, but the theoretical predictions are highly dependent upon the underlying assumptions of the particular modeling strategy used to create the PAM. In general, three types of PAMs are used to estimate activation: 1) field-cable (FC) models, 2) driving force (DF) models, and 3) volume of tissue activated (VTA) models. FC models represent the "gold standard" for analysis but at the cost of extreme technical demands and computational resources. Consequently, DF and VTA PAMs, derived from simplified FC models, are typically used in clinical research studies, but the relative accuracy of these implementations is unknown. Therefore, we performed a head-to-head comparison of the different PAMs, specifically

evaluating DBS of three different axonal pathways in the subthalamic region. The DF PAM was markedly more accurate than the VTA PAMs, but none of these simplified models were able to match the results of the patient-specific FC PAM across all pathways and combinations of stimulus parameters. These results highlight the limitations of using simplified predictors to estimate axonal stimulation and emphasize the need for novel algorithms that are both biophysically realistic and computationally simple.

3.1. Introduction

Deep brain stimulation (DBS) is an established clinical therapy for a range of neurological disorders. The most common application is subthalamic DBS for the treatment of Parkinson's disease (PD). Advanced medical imaging and decades of clinical experience have helped define possible anatomical targets for therapeutic stimulation in the subthalamic region [e.g. Saint-Cyr et al., 2002; Herzog et al., 2004; Nowinski et al., 2005; Butson et al., 2011; Welter et al., 2014; Eisenstein et al., 2014]. However, there is still little to no clinical consensus on the specific neural elements (and/or axonal pathways) that are necessary and sufficient for evoking therapeutic effects when stimulated [Hamel et al., 2017].

Patient-specific computational models are tools to study the underlying effects of DBS and develop more effective stimulation paradigms [McIntyre et al., 2007]. They allow for noninvasive quantitative characterization of the theoretical response of various neural elements to a wide range of stimulation settings.

Recently, patient-specific DBS models have been used in combination with explicit representations of axonal pathways, typically derived from tractography, to evaluate possible stimulation correlations with symptom improvement or side effects [Chaturvedi et al., 2010]. These pathway-activation models (PAMs) explore the effects of DBS while leveraging advances in scientific documentation of the human brain structural connectome. Subthalamic DBS has already been the focus of numerous PAM studies [e.g. Coenen et al., 2011; Chaturvedi et al., 2012; Groppa et al., 2014; Sweet et al., 2014; Accolla et al., 2016; Vanegas-Arroyave et al., 2016; Gunalan et al., 2017; Horn et al., 2017; Akram et al., 2017]. However, the various analyses with PAMs have employed a wide range of different methods without much in the way of documentation or validation of their accuracy.

There are currently three general classes of methods for estimating the response of axonal pathways to DBS: 1) field-cable (FC) methods, 2) driving force (DF) methods, and 3) volume of tissue activated (VTA) methods. FC methods are the most detailed and technically demanding, explicitly modeling the electric field, axonal trajectories, and transmembrane ion channels responsible for action potential initiation in response to extracellular stimuli [McNeal, 1976; Gunalan et al., 2017]. DF methods require calculation of the electric field but simplify the estimation of the transmembrane response to substantially speed up the simulations [Warman et al., 1992; Peterson et al., 2011]. VTA methods simplify calculations of the electric field and axonal response into a generic

algorithm that is the fastest and easiest to implement [Butson and McIntyre, 2006; Chaturvedi et al., 2013].

Numerous academic software tools have recently been created to help facilitate the use of algorithms to estimate pathway activation by clinical DBS researchers [e.g. Miocinovic et al., 2007; Horn and Kuhn, 2015; Lauro et al., 2016; Noecker et al., 2017]. However, these tools hide non-expert users from the technical details of the methodology and tend to rely on numerous simplifications to generate their results, which subsequently have unknown implications on the conclusions reached. This technical issue within the burgeoning field of connectomic modeling of DBS is exacerbated by the lack of direct comparisons of different methods for estimating axonal responses to electrical stimulation [Chaturvedi et al., 2010; Howell and McIntyre, 2017]. Therefore, the goal of this study was to perform a head-to-head comparison of different methods for estimating axonal activation, specifically evaluating DBS of three different axonal pathways in the subthalamic region.

3.2. Methods

3.2.1. Patient-specific model of subthalamic DBS

The technical details and methodology for constructing the patient-specific models of DBS are described in prior works [Howell and McIntyre, 2016; Howell and McIntyre, 2017; Gunalan et al., 2017] and summarized below. We hypothesized that the assumptions and simplifications inherent in DF and VTA PAMs would generate markedly different results when compared to the current

standard for biophysical modeling of DBS, FC PAMs. We used the most detailed patient-specific foundation for DBS modeling currently available to perform our analysis [Gunalan et al., 2017], and attempted to minimize sources of variance between comparison of methods. We used the FC PAM, one DF PAM [Peterson et al., 2011] and three VTA PAMs [Chaturvedi et al., 2013; Madler and Coenen, 2012; Astrom et al., 2015] to estimate the activation thresholds of individual axons within three different pathways coursing through the subthalamic region. Our pathways of interest were the internal capsule fibers of passage (IC), hyperdirect pathway (HDP), and cerebellothalamic tract (CbTT). These pathways were chosen for their clinical relevance.

3.2.1.1. Patient data

Collection of all patient data for this study was approved by the University of Minnesota Institutional Review Board. Pre-operative T1-weighted (T1W), T2-weighted (T2W), susceptibility-weighted (SW), and diffusion-weighted (DW) images were obtained on a 7T magnetic resonance imaging (MRI) system (Magnex Scientific, UK) [Duchin et al., 2012; Gunalan et al., 2017]. A pre-operative T1W image was also acquired on a 1.5T Siemens Magnetom Espree. These MRI data were used to create the anatomical model of the patient. A post-operative CT image (Biograph64 Sensation, Siemens) was obtained approximately 1 month after surgery and used to define the location of the implanted DBS electrode.

3.2.1.2. Image processing

The DW images were corrected for distortions from eddy currents using FSL's *eddy* tool and from magnetic field inhomogeneities using FSL's *topup* tool. We registered all images to the T1W image using Advanced Normalization Tools or FSL's image registration tool, *flirt* [Jenkinson and Smith, 2001; Jenkinson et al., 2002]. FSL's brain extraction tool, *bet* [Smith, 2002], was used to isolate the brain from the 1.5T T1W image, and subsequently, we used FSL's automated segmentation tool, *fast* [Zhang et al., 2001], to subdivide the brain image into grey matter, white matter, and cerebrospinal fluid (CSF). The locations of bone and other soft tissues (e.g. fat and muscle) were approximated using a detailed single-patient atlas named MIDA [Iacono et al., 2015]. A linear mapping was calculated by using *flirt* with 12 degrees of freedom to coregister the grey matter, white matter, and CSF tissue types in the MIDA image to those in the patient's T1W image, and the affine transformation was used to warp the MIDA masks of the non-brain regions into the patient's T1W space [Gunalan et al., 2017].

Manual segmentation of subcortical nuclei (putamen, globus pallidus, subthalamic nucleus, substantia nigra, red nucleus) was performed with Seg3D. As no image had adequate contrast for thalamic segmentation, we fit the thalamic atlas developed by Krauth et al. [2010] to the 1.5T T1W image in Cicerone [Miocinovic et al., 2007]. Freesurfer's *recon* tool was used to segment the ipsilateral CSF and contralateral cerebral hemisphere from the 1.5T T1W image [Fischl et al., 2012].

3.2.1.3. Streamline reconstruction

We reconstructed three pathways for our analysis: internal capsule fibers of passage (IC), hyperdirect pathway (HDP), and cerebellothalamic tract (CbTT) (Figure 3.1). IC and HDP are comprised of layer V pyramidal cells that project corticofugal axons from the motor cortex, through the internal capsule, and terminate in the brainstem/spinal cord. The HDP is distinct from the IC in that it gives off a collateral from the corticofugal axon to the STN [Nambu et al., 2002; Kita and Kita, 2012; Haynes and Haber, 2013]. The CbTT originates from the dentate nucleus of the cerebellum, passes through the superior cerebellar peduncle, and terminates in the ventral lateral posteroventral (VLpv) thalamic nucleus [Gallay et al., 2008].

The IC, HDP, and CbTT each represent pathways of substantial clinical interest in the subthalamic region for DBS studies. Stimulation of the IC is commonly associated with motor contraction side effects of subthalamic DBS [Tommasi et al., 2008; Mahlknecht et al., 2017]. Stimulation of the HDP is thought to be a major contributor to the therapeutic effects of subthalamic DBS [Walker et al., 2012; Sanders and Jaeger, 2016]. Stimulation of the CbTT is considered therapeutic for the control of tremor [Coenen et al., 2011; Groppa et al., 2014; Sweet et al., 2014], but has also been implicated in the generation of speech disturbance side effects [Astrom et al., 2010; Tripoliti et al., 2014].

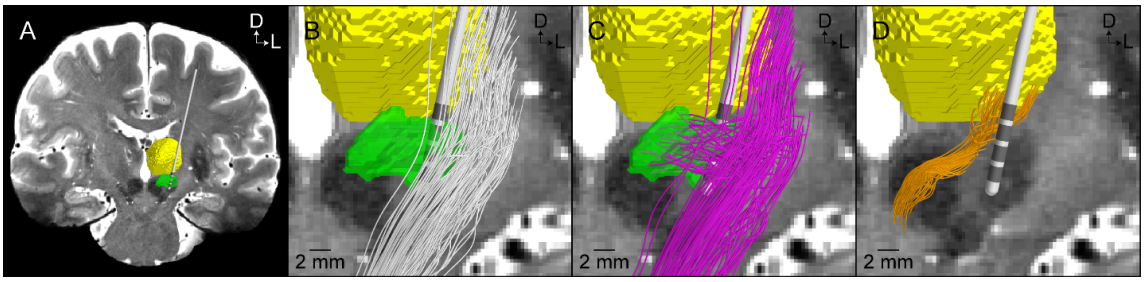

Figure 3.1. Patient-specific axonal pathways. (A) A coronal view of the 7T T2-weighted magnetic resonance image along with overlaid representations of the DBS lead (Medtronic model 3389), thalamus (yellow), and subthalamic nucleus (green). Representative population of 100 streamlines of the: (B) internal capsule fibers of passage (white streamlines), (C) hyperdirect pathway (pink streamlines), and (D) cerebellothalamic tract (orange streamlines). Axes: D = dorsal, L = lateral.

We used the probabilistic tractography toolbox in FSL to reconstruct the IC, HDP, and CbTT pathways. Diffusion parameters were fit using *bedpostx*, and streamlines were generated with *probtrackx*. We saved only those streamlines that originated in the seed mask, terminated in the target mask(s), and avoided the exclusion masks (as well as the patient-specific DBS electrode position). We fit a smoothing spline to the tractography-generated streamlines to create the axonal trajectories used in our simulations (Figure 3.1 and Appendix C).

The streamlines of the IC were generated from a seed region (with 100 seeds per voxel) that resided in the white matter lateral to the STN, between the thalamus and lenticular nucleus. Streamlines connected a target mask in the cerebral peduncle of the midbrain to another target mask superior to the seed mask [Gunalan et al., 2017], while avoiding the ipsilateral thalamus, globus pallidus, putamen, substantia nigra, red nucleus, CSF, DBS lead, and contralateral cerebral hemisphere. This process resulted in 13,219 streamlines, from which we randomly subsampled 1,000 to represent the IC. The corticofugal

streamlines of the HDP were constructed by randomly subsampling another 1,000 samples from the IC population. Then for each axon of the HDP, we constructed a collateral that branched from a node of Ranvier along the corticofugal axon and terminated within the STN [Kang and Lowery, 2014; Gunalan et al., 2017].

The streamlines of the CbTT were generated from a seed mask within the contralateral superior cerebellar peduncle (with 2,000 seeds per voxel) (Appendix C). Streamlines decussated, then passed through a waypoint mask between the red nucleus and subthalamic nucleus, and terminated within the VLpv thalamic nucleus (Appendix C) [Gallay et al., 2008], while avoiding the ipsilateral globus pallidus, substantia nigra, subthalamic nucleus, ventral lateral anterior (VLa) thalamic nucleus, ventral posterior lateral (VPL) thalamic nucleus, CSF, DBS lead, and contralateral cerebral hemisphere. Additionally, we excluded streamlines that traveled superior to the VLpv thalamic nucleus. Applying these constraints resulted in 1,662 streamlines, from which we randomly subsampled 1,000 for creation of our CbTT. We then extended these CbTT streamlines up into the VLpv, using a weighting of the average their trajectory, so they did not simply terminate at the ventral border of the thalamus.

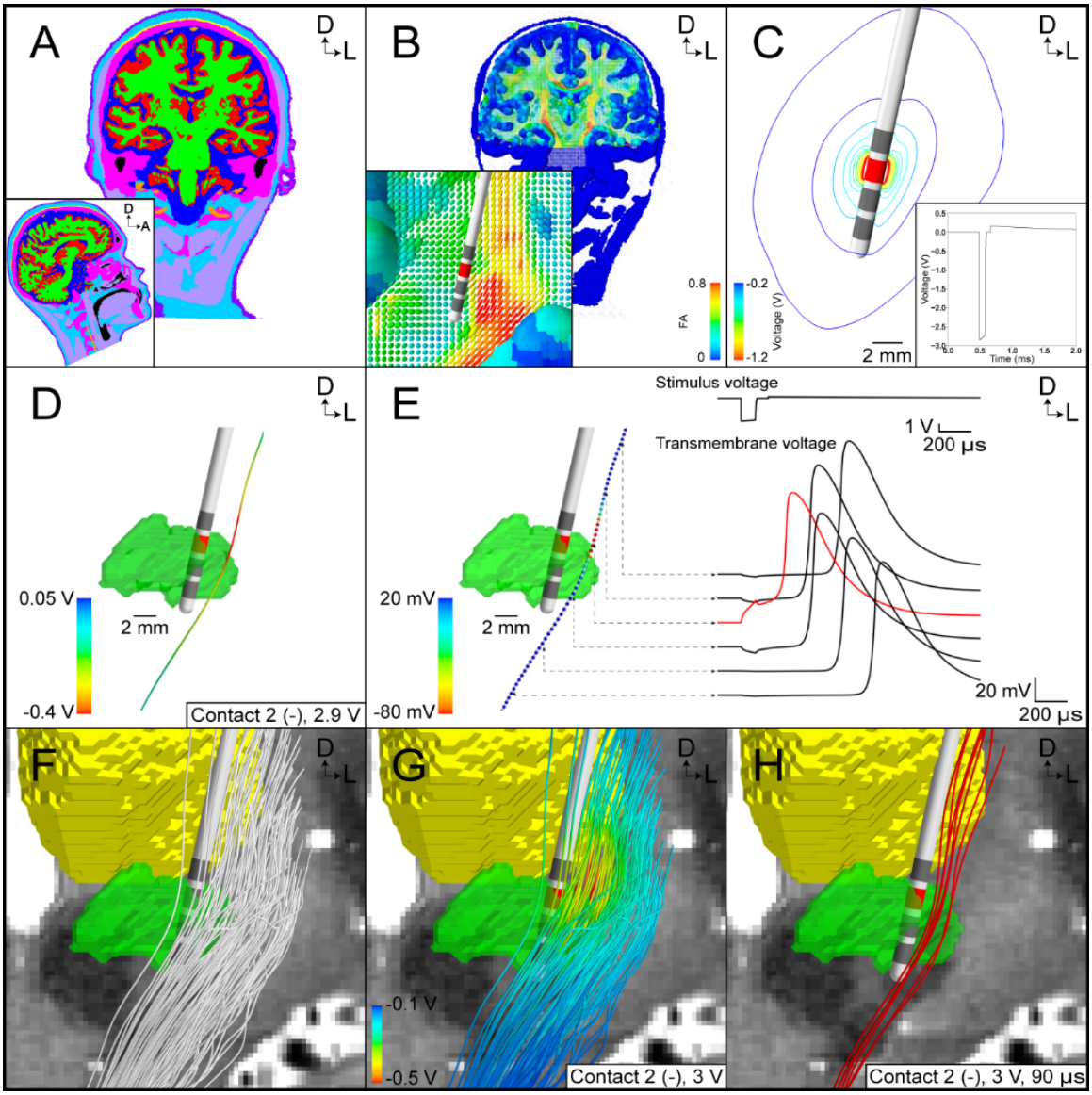

Figure 3.2. FC PAM of subthalamic DBS. (A) Tissue-type segmentation (grey matter – red, white matter – green, cerebrospinal fluid – dark blue, muscle – light purple, tendon – yellow, bone – pink, fat – light blue, skin – dark purple, intervertebral disks – not visible, blood – orange, air – black). (B) Conductivity tensors. The tensors are colored according to their fractional anisotropy (FA). (C) Isolines of the potential distribution generated by the Medtronic model 3389 lead (active contact – red). Inset. Stimulus waveform at the electrode-tissue interface. (D) Extracellular potentials interpolated along a tractography-generated streamline. (E) Multi-compartment cable model of an axon is stimulated with a suprathreshold stimulus from D. (Right) Stimulus waveform and transmembrane voltage response at select nodes of Ranvier (red line - node of action potential initiation). (F) Subsample of 100 axons representing the internal capsule fibers of passage. (G) Potential distribution used to stimulate the axon models. (H) Axons that generate action potentials in response to stimulation.

3.2.1.4. Volume conductor

The volume conductor of the head consisted of three domains (Figure 3.2): (1) a domain of encapsulation tissue delineated by the internal boundary representing the implanted Medtronic model 3389 lead and the outer surface of a 0.5 mm thick uniform layer surrounding the lead, (2) a domain of brain tissue delineated by the outer boundaries of the encapsulation tissue and the surface of the brain, and (3) a non-brain domain delineated by the outer boundaries of the brain and the scalp.

We constructed a conductivity tensor field for the entire head volume in the patient's T1W space. Specifically, each voxel was categorized into 1 of 11 different types of tissues (Figure 3.2A), each with its own corresponding effective conductivity [Gunalan et al., 2017]. Within the brain volume, FSL's *dtifit* tool was used to fit a single tensor to the signal in each voxel of the patient's DW image and the tensors in DW space were warped to T1W space. We then used the load preservation approach to define a conductivity tensor in each voxel from the respective isotropic conductivity, and eigenvalues and eigenvectors of the fitted diffusion tensor [Howell and McIntyre, 2016]. Diffusion tensor data was only used within the boundaries of the patient's brain (i.e. domain 2); therefore, conductivity tensors within the brain were modeled as anisotropic, whereas the conductivity tensors outside the brain (i.e. in domain 3) were modeled as isotropic.

We used COMSOL (version 5.1) to construct tetrahedral meshes for the head model. The mesh was refined with an especially high nodal density within

a 30-mm cubic region surrounding the tip of the modeled DBS lead. Elements within domain 1, the encapsulation tissue, were assigned an isotropic conductivity of 0.07 S/m, which falls within the range of previously reported values [Grill and Mortimer, 1994] and was chosen so that the load of the modeled head matched that measured from the patient by the Medtronic programming device [Gunalan et al., 2017]. Elements in domains 2 and 3, the brain and non-brain domains, respectively, were assigned conductivity tensors based on their proximity to the nearest neighbor in the tensor field defined by the structured rectangular grid in the patient's T1W space. The complete head model consisted of 1,429,416 total tetrahedral elements and 6,524,354 nodes in the finite element mesh.

For stimulation configurations where the implantable stimulator was intended to be the return electrode (i.e. monopolar configurations), we defined Dirichlet boundary conditions of 1 V at the active contact(s), and 0 V at the neck. Inactive contacts were treated as ideal conductors and modeled using Robin boundary conditions that specified two conditions, per contact: all potentials within the contact were equal in value, and the net current flow through the surface of the contact was 0 A. Neumann boundary conditions of 0 A/mm^2 were used to model the electrode shaft and scalp surface (minus the neck) as perfect insulators. In stimulation configurations where the return and source were both electrode contacts (i.e. bipolar configurations), the base of the neck was insulated.

The potential field in the volume conductor at the onset of the stimulus was calculated by using the finite element method (FEM) to solve numerically Laplace's equation for conductive media:

Equation 3.1. Laplace's equation.

$$\nabla \cdot (\Sigma \cdot \nabla \Phi) = 0$$

, where Σ is the tensor conductivity field. The variation of the potentials over time was approximated by multiplying the above solution with a time-varying waveform derived from an equivalent circuit model of the implanted DBS system [Gunalan et al., 2017].

3.2.1.5. Cable model of axons

Multi-compartment cable models of axons were constructed and solved in the NEURON simulation environment (version 7.3). We started with the MRG axon model [McIntyre et al., 2002] and modified some of the geometrical parameters to better reflect central nervous system axons [Howell and McIntyre, 2016]. We defined the diameter of the hyperdirect collateral as a fraction (1/3.1) of the diameter of the corticofugal axon [Hongo et al., 1987; Struijk et al., 1992; Grill et al., 2008]. We used the streamlines generated from tractography (Section 3.2.1.3) to define the axonal trajectories in the volume conductor. The extracellular potentials at the coordinates of each compartment of the axon model were interpolated from the spatiotemporal distribution of potentials calculated from the volume conductor model (Section 3.2.1.4). These potentials

were used to stimulate the modeled axons [McNeal, 1976; Gunalan et al., 2017] (Figure 3.2). For a given electrode configuration and stimulus pulse width, we used a binary search algorithm to determine the threshold stimulus amplitude for action potential generation to within 0.01 V. An axon was deemed activated when it responded “one-to-one” with the stimulus frequency. The combination of the electric field from the volume conductor and axonal responses from the multi-compartment cable models represent the results of the FC PAM (Figure 3.2).

3.2.2. DF PAM

Simulating the nonlinear response of axons in an FC PAM is a time-consuming process. Therefore, incentives exist for estimating the axonal response using predictive algorithms. Charge flow throughout an axon is modeled with the cable equation, where the driving force (DF) approximates the effects of the extracellular potentials on the neural membrane [McNeal, 1976]. Warman et al. [1992] demonstrated that a weighted version of the DF could be used to calculate the steady-state response of a passive cable in response to an extracellular stimulus, and the passive response could, in turn, be used to estimate the threshold for activation in the corresponding nonlinear axon model. However, it is not possible to determine a priori the critical steady-state response that corresponds to the threshold for activation in the nonlinear axon model. Therefore, DF-based predictors are capable of reducing computation time and achieving relatively high accuracy in most situations, but require extensive parameterization steps [Moffitt et al., 2004]. In this study, we elected to analyze

the most recent iteration of a DF-based predictor [Peterson et al., 2011], which we refer to as DF-Peterson.

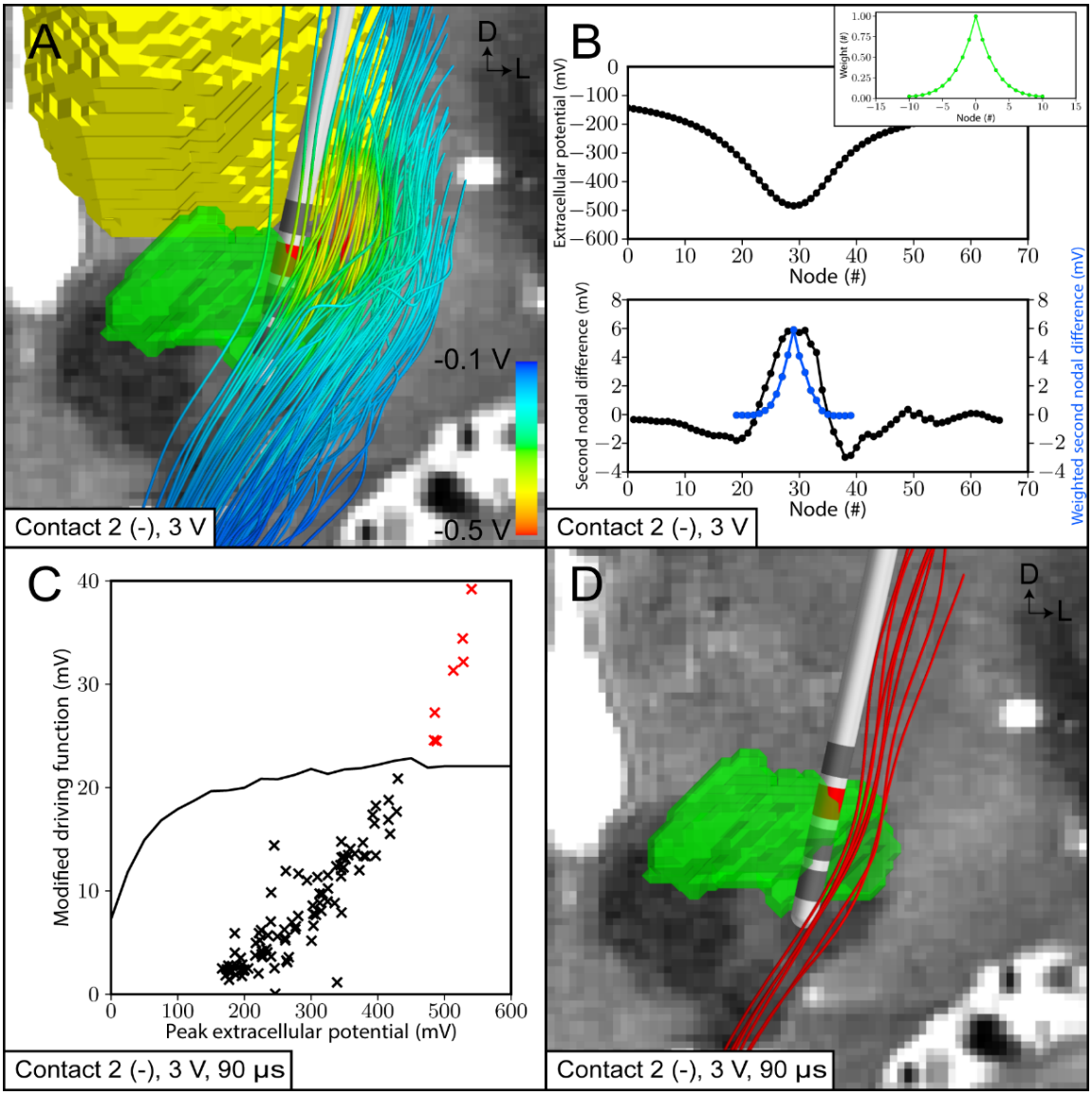

Figure 3.3. DF PAM of subthalamic DBS. (A) Extracellular potentials (Φ_e) calculated from the patient-specific volume conductor (3 V, contact 2 [-]) were interpolated along 100 internal capsule fibers of passage. (B) (Top) Φ_e at the nodes of Ranvier along an example axon. (Bottom) Second differences of Φ_e (black line) and weighted second differences of Φ_e (blue line). (Inset) Corresponding weights for weighted second difference calculation (green line). (C) Peterson et al. [2011] threshold modified driving force (MDF_{th}) values as a function of the maximum extracellular potential ($\Phi_{e,0}$) (black line). Patient-specific axons with a MDF that lie above the threshold curve are classified as active (red cross). (D) Axons that are categorized as active for a 3 V stimulus amplitude. Pulse width = 90 µs. Axon diameter = 5.7 µm.

3.2.2.1. DF-Peterson

Peterson et al. [2011] estimated stimulation thresholds based on two metrics: the maximum magnitude of the stimulus potentials (Φ_e) across the axon and the weighted sum of $\Delta^2\Phi_e$ across the nodes of Ranvier (NoRs), which they refer to as a modified driving force (MDF),

Equation 3.2. Modified driving force.

$$MDF = \sum_{i=-n/2}^{n/2} w_i(PW, D)\Delta^2\Phi_{e,i}$$

Equation 3.3. Second difference calculation.

$$\Delta^2\Phi_{e,i} = \Phi_{e,i-1} - 2\Phi_{e,i} + \Phi_{e,i+1}$$

, where *i* is the index of a given NoR, w_i is a weighting term at the ith NoR for a given stimulus pulse width (PW) and axon diameter (D), and 2*n+1* is the total number of NoRs. The calculation of the weights is summarized in the Section A of the Supplementary Text.

Development of the DF-Peterson algorithm can be summarized in two phases: In the first phase, vectors of applied potentials were constructed without the use of a volume conductor. They began by designating values for Φ_e and $\Delta^2\Phi_e$ at the middle NoR, which we refer to as $\Phi_{e,0}$ and $\Delta^2\Phi_{e,0}$, respectively. Assuming that $\Phi_{e,0}$ is maximal and $\Phi_{e,-1}$ = $\Phi_{e,+1}$, (3.3) was used to define $\Phi_{e,-1}$ and $\Phi_{e,+1}$. The remaining nodal potentials were then set to decay so that the first derivatives were zero at the ends of the axons, and a fitted spline was used to define the potentials at all internodal compartments. This process was repeated,

constructing vectors of applied potentials for various different combinations of $\Phi_{e,0}$ and $\Delta^2\Phi_{e,0}$, and (3.2) was used to calculate an MDF for each vector of potentials.

In the second phase, simulations were conducted in NEURON to determine which vectors of potentials from the previous phase evoked action potentials in the modeled axon [McIntyre et al., 2002]. The threshold MDF was defined as the smallest MDF for a given $\Phi_{e,0}$ whose corresponding potentials directly activated the axon. The threshold MDFs for all values of $\Phi_{e,0}$ at a given PW and D were summarized in a lookup table, and phases 1 and 2 were repeated for various combinations of PW and D. PWs ranged from 20 μs to 10 ms, and Ds ranged from 4 μm to 20 μm. We refer to the threshold $\Phi_{e,0}$ and threshold MDF as $\Phi_{e,0,th}$ and MDF_{th}, respectively.

Peterson et al. [2011] provide the data for implementing their predictor in Tables S1 and S3 of their supplement (Note: in their Table S3, units of potentials are in mV, whereas units of MDF are in μV). We calculated weights at unspecified combinations of D and PW using bilinear interpolation, and nearest neighbor extrapolation was used to estimate MDF_{th} at $\Phi_{e,0,th}$ > 500 mV (Appendix C). We also used a fitted spline to approximate the continuous relationship between $\Phi_{e,0,th}$ and MDF_{th}. Stimulation thresholds at a given D and PW were calculated as follows (Figure 3.3). First, for a given axon, we sampled Φ_e at the NoRs generated with the patient-specific volume conductor (Figure 3.3A/B). The NoR at which Φ_e was maximal was designated as i = 0. The potential at this NoR was defined as $\Phi_{e,0,unit}$, and we used (2) to calculate the corresponding MDF_{unit},

where “unit” designates that values were calculated at an applied voltage of 1 V. Then, $\Phi_{e,0}$ and MDF were calculated by multiplying $\Phi_{e,0,unit}$ and MDF_{unit} by a scalar, respectively. The stimulation threshold voltage was the smallest scalar multiple that when applied to $\Phi_{e,0,unit}$ generated an $\Phi_{e,0}$ whose corresponding MDF was $\geq MDF_{th}$ (Figure 3.3C/D).

For the HDP, we calculated the thresholds in a piecewise manner. We calculated the MDF_{unit} along the main body of the corticofugal axon separately from the MDF_{unit} along the collateral projecting to the STN. We then used the larger of the two MDF_{unit} to calculate thresholds as described above.

3.2.3. VTA PAMs

Another way to simplify bioelectric field modeling is to use a predictor to estimate the nonlinear relationship between the parameters of stimulation and the spatial extent over which axons are activated. The typical approach is to use an ellipsoidal volume, commonly referred to as a volume of tissue activated (VTA) [Butson and McIntyre, 2006]. VTA PAMs are derived from highly simplified FC models, where a DBS lead is placed in an isotropic volume conductor and used to estimate the extent of activation of straight axons oriented perpendicular to the electrode shaft (Figure 3.4A). Simulations are conducted to assess which axons are directly activated for various stimulation settings and circumscribing ellipsoids are used to approximate the region of activation. This section describes three common implementations of VTA PAMs (Figure 3.4). We defined the stimulation threshold for direct activation of an axon as the

minimum voltage amplitude needed to generate a VTA that intersects the respective streamline for a given axon diameter, stimulus pulse width, and electrode configuration (Figure 3.4C).

3.2.3.1. VTA-Chaturvedi

Chaturvedi et al. [2013] used a series of ellipsoids to approximate the planar regions of activation, and then used an artificial neural network (ANN) to predict the relationship between a set of input parameters (described below), and the center and radii of the ellipsoids, which were the output of the ANN. We refer to this VTA PAM as VTA-Chaturvedi. This predictor represents the latest advancement of the original concepts developed by Butson and McIntyre [2006] and is capable of predicting the VTA for multipolar electrode configurations and multiple axon diameters.

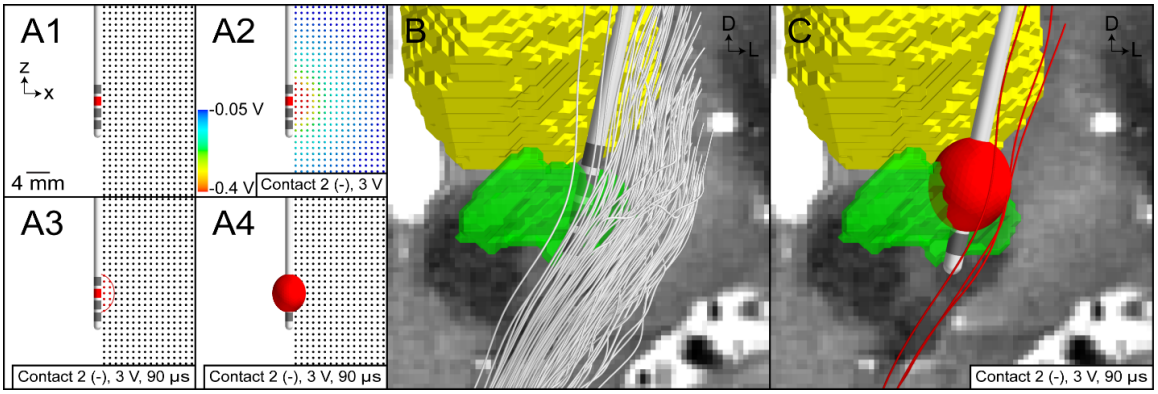

Figure 3.4. VTA PAM for subthalamic DBS. (A) Illustrative example of training a VTA algorithm with a simplified axisymmetric model of DBS. (A1) Multi-compartment cable models of straight axons perpendicular to the electrode are modeled. (A2) The potential distribution from a volume conductor model with isotropic and homogeneous conductivities is used to stimulate the model axons. (A3) Those axons that are activated by stimulation are shown as red. A circumscribing ellipse is then used to characterize the spatial extent of activation of the straight axons. (A4) The ellipse is then extruded about the electrode shaft to create a 3-dimensional ellipsoid volume. (B) Trajectories of internal capsule fibers of passage are generated using probabilistic tractography. (C) A rigid body transformation is used to map the VTA to the patient-specific location of the DBS electrode, and the trajectories of axons that intersect the VTA are categorized as active (red streamlines).

Given an electrode configuration, an electrode/access resistance (R_a), a stimulus amplitude ≤ 10 V, a PW between 60 µs and 450 µs, and axon diameter of 2 µm, 5.7 µm, or 10 µm; we generated an ellipsoid or set of ellipsoids based on the radii and center coordinates output from the ANN. The VTAs were then used to estimate which axons in the IC, HDP, and CbTT pathways were activated by quantifying the intersection of individual streamlines with the VTA (Figure 3.4). The VTA-Chaturvedi predictor is currently employed by the StimVision software tool [Noecker et al., 2017].

3.2.3.2. VTA-Astrom

Astrom et al. [2015] constructed VTAs based on the magnitude of the electric field (E_T). For a given combination of PW and D, E_T was calculated at the location in the grid where the furthest perpendicular axon was activated, and this process was repeated (at a given PW and D) across a number of stimulation amplitudes. The effective nominal threshold, or $E_{T,th}$, was the median threshold E_T across all the stimulus amplitudes. The VTA, then, was the minimum ellipsoidal volume circumscribing the volume delineated in the bulk tissue where E were $\geq E_{T,th}$. We refer to this predictor as VTA-Astrom.

Astrom et al. [2015] provide a table summarizing $E_{T,th}$ for PWs between 30 μs and 120 μs and Ds between 2 μm and 7.5 μm. Because only values for $E_{T,th}$ were provided, we constructed the simplified axisymmetric volume conductor model used in their work. The conductivity of the bulk tissue and scar were set to 0.2 S/m and 0.1 S/m, respectively, which yielded an R_a that matched their reported value of 1 kΩ. We then changed the encapsulation layer conductivity from 0.1 S/m to 0.0625 S/m, yielding an R_a of 1.37 kΩ, that matched the R_a in our patient-specific model, and we used the axisymmetric model to calculate the VTAs described above. For combinations of PW and D that were not provided in the tables, we estimated $E_{T,th}$ by using a fitted bivariate decaying rational function to interpolate and extrapolate values (Appendix C). The concept of $E_{T,th}$-based VTAs are currently employed by the Lead-DBS software tool [Horn et al., 2017].

VTA-Astrom is based on a myelinated single-cable axon model whose ion channels and geometry are different than that of the double-cable model used in

this study. The results of the former match the latter when their axon diameters are 3.5 μm and 5.7 μm [Astrom et al., 2015], respectively, so to match better VTA-Astrom with the FC PAM, we reduced the axon diameter by a factor of 0.6140 (i.e., 3.5/5.7) when analyzing a subset of the axonal responses with VTA-Astrom (Appendix C).

3.2.3.3. VTA-Madler

Madler and Coenen [2012] began with digital reconstructions of ellipsoidal VTAs originally calculated by Butson et al. [2006], and the lateral radius of each ellipsoid, which is the radius transverse to the electrode shaft's axis, was used to define a corresponding spherical VTA. Next, they used a fitted second-order bivariate polynomial to approximate the relationship between the applied voltage, the nominal dependent variable, and two nominal independent variables, the radius of the spherical VTA and R_a. Coefficients that altered the output of the predictor by < 1% were dropped, thereby allowing the radius of the spherical VTA to be expressed as a closed-form function of the applied voltage and R_a. We refer to this bivariate quadratic predictor as VTA-Madler.

VTA-Madler can be used for a range of R_a, namely between 741 Ω and 1244 Ω, but the data used to fit the predictor only reflects one combination of PW and D; more specifically, PW = 90 μs and D = 5.7 μm. Therefore, this predictor is very limited compared to the other more flexible predictors. The VTA-Madler predictor is currently employed by the DBSproc software tool [Lauro et al., 2016].

3.2.4. Analyses

Stimulation thresholds were calculated for all 1,000 axons in each pathway (IC, HDP, CbTT) using the most advanced methods for patient-specific modeling of DBS (Section 3.2.1, Figure 3.2) [Gunalan et al., 2017]. We defined thresholds from the FC PAM as our gold standard and evaluated the ability of the simplified predictor functions to estimate the thresholds of each axon. We omitted those axons from our analyses that initiated action potentials from the distal nodes of Ranvier along the main body of the axon, as calculated with the FC PAM. This resulted in 933, 983, and 1,000 axons for the IC, HDP, and CbTT, respectively. We defined absolute error in the voltage stimulation threshold (V_{th}) as $V_{th,Predictor}$-$V_{th,FC}$. Axons with $V_{th,FC}$ > 10 V or $V_{th,Predictor}$ > 10 V were omitted from the stimulus threshold error calculations, as these stimulation amplitudes are not relevant to clinical DBS.

Using the threshold amplitude calculations, we created recruitment curves at a 0.1 V step size. For a given pathway, each axon was randomly clustered into 100 subsamples of 1000 axons in a bootstrapping manner (with replacement), to quantify the effects of variability in the distribution of the axon trajectories. The average and 2.5% to 97.5% quantiles of the number of activated axons for the 100 subsamples in response to a stimulation amplitude are presented in the recruitment curves.

Table 3.1. Predictive algorithms and the parameters for which they were developed.

Predictor	Amplitude (V)	Pulse width (μs)	Frequency (Hz)	Configuration	Electrode impedance (Ω)	Axon diameter (μm)
DF-Peterson	0-0.5[a]	20 - 10,000	Single pulse[b]	N/A[a]	N/A[a]	4.0 - 20.0
VTA-Chaturvedi	≤ 10	60, 90, 120, 150, 180, 210, 450	130[c]	Monopolar, Bipolar	Low (0-749), Medium (750-1250), High (1251+)	2.0, 5.7, 7.3, 8.7, 10.0
VTA-Madler	1-10	90	130[c]	Monopolar	Low (741), Medium (1003), High (1244)	5.7
VTA-Astrom	1-5 (step 0.5)	30, 60, 90, 120	Single pulse[c]	Monopolar	1000	2.0 - 7.5 (step 0.5)[d]

[a]Predictor was developed for a peak extracellular potential along an axon. Thus this is irrespective of the applied stimulus amplitude and electrode configuration.
[b]Square, monophasic pulse.
[c]Representative of the stimulation waveform output from a Medtronic pulse generator.
[d]Axon diameter to internodal distance relationship is different than the other predictors.

3.3. Results

We constructed a detailed patient-specific model of subthalamic DBS and used it to evaluate a range of different methods for estimating axonal response. The FC PAM, which incorporated the latest advances in biophysical modeling of DBS [Gunalan et al., 2017], served as our gold standard, and we compared those results to the estimations of four predictive algorithms. Some of the predictors were unable to simulate all of the combinations of stimulus pulse widths, electrode configurations, and axon diameters investigated in this study. Therefore, an absence of results in the figures indicates that the corresponding

predictor could not evaluate thresholds for that given set of parameters. The model parameters used to develop each predictor are summarized in Table 3.1.

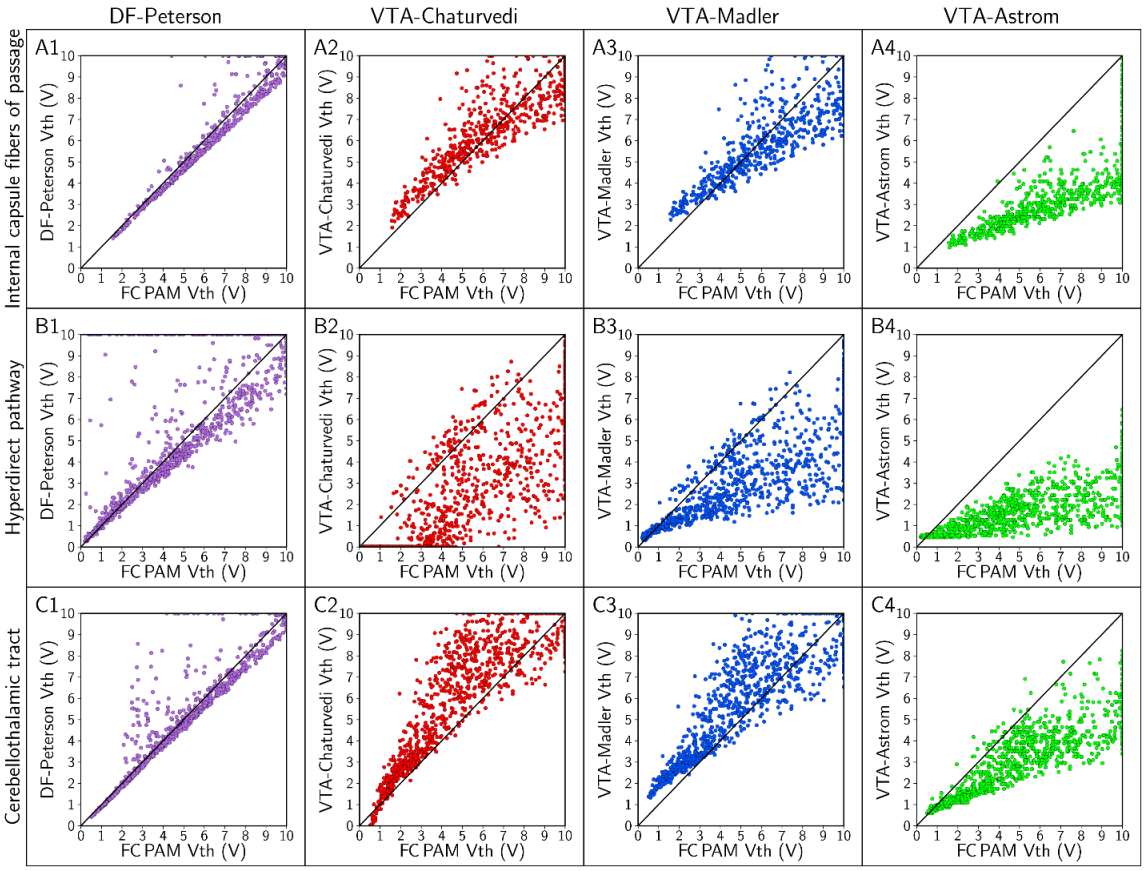

Figure 3.5. Axon-to-axon comparison of threshold stimulus amplitude (V_{th}) with FC, DF, and VTA PAMs. We used a stimulus pulse width of 90 μs and a monopolar cathodic electrode configuration (contact 2 [-] and case [+]) to stimulate axons with diameters of 5.7 μm. The rows denote results for the: (A) internal capsule fibers of passage, (B) hyperdirect pathway, and (C) cerebellothalamic tract; and there is one column for each of the four predictors. In this plot, we set axons with V_{th} > 10 V as 10 V, so that all axons representing a pathway can be visualized in the field of view.

3.3.1. Errors in stimulation thresholds

Absolute errors in the predicted stimulation thresholds had systematic trends. Errors generally increased with increasing stimulus amplitude, and errors in estimating the stimulation thresholds of the HDP were markedly greater than

the errors in estimating thresholds of the IC and CbTT (Figures 3.5 and 3.6). However, the order of magnitude of the absolute errors was not the same across the different predictors (Figure 3.7). We observed the largest errors with VTA-Astrom, which had median errors of between −1 V and −4 V. The next most accurate predictors were VTA-Chaturvedi and VTA-Madler, with median errors of between −3 V and 3 V. DF-Peterson was the most accurate, with median errors of between −3 V and 1 V. No predictor was accurate enough to limit errors to within 1 V across all stimulus pulse widths, electrode configurations, and axon diameters tested (Figure 3.7).

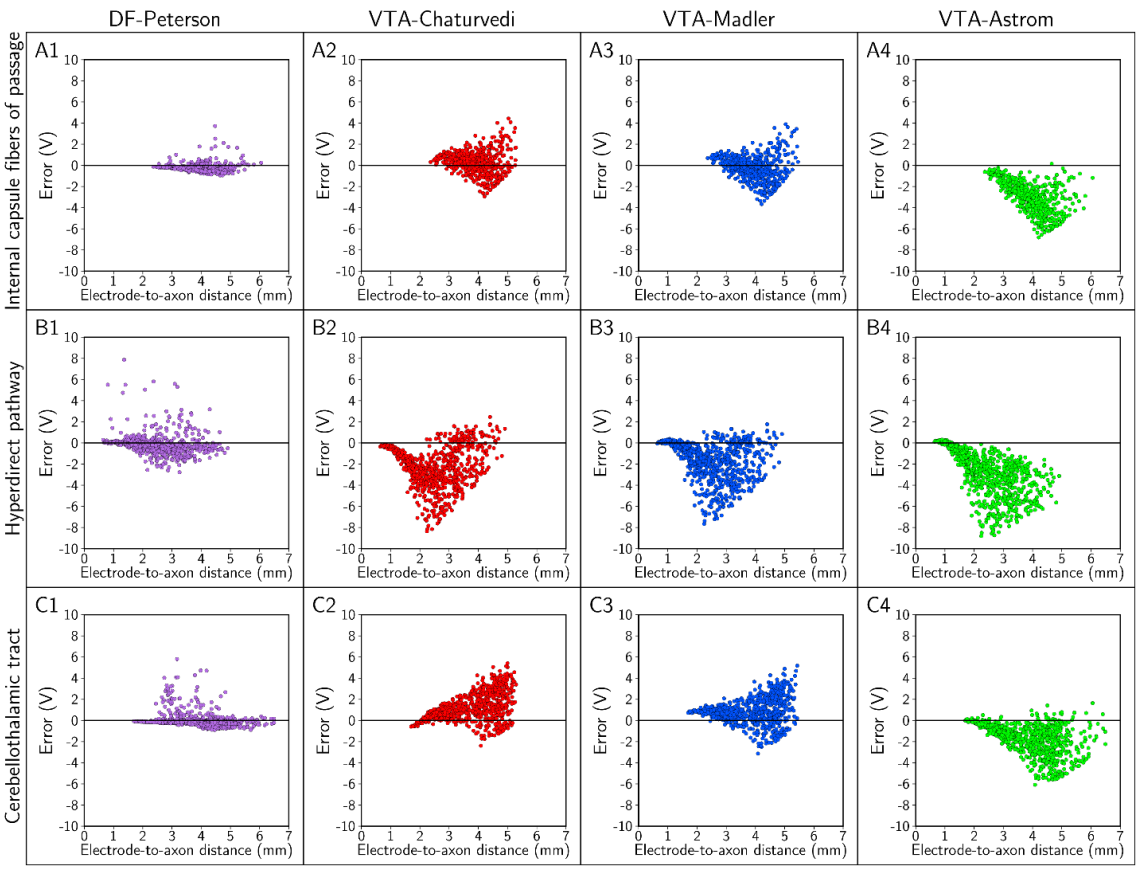

Figure 3.6. Errors in the threshold stimulus amplitude as a function of the electrode-to-axon distance. Each column pertains to one predictor, and errors were calculated for the: (A) internal capsule fibers of passage, (B) hyperdirect pathway, and (C) cerebellothalamic tract. In this analysis, the stimulus pulse width was 90 μs; contact 2 was the cathode (-), the case was the anode (+), and the axon diameter was 5.7 μm.

Given that the DF and VTA PAMs are derived from relatively simplified models of stimulation (Figures 3.3 and 3.4), we expected to find inherent biases in their results as described above. The biases in the VTA PAMs are likely due to disparities in the decay and shape of the extracellular potentials between the simple volume conductor model (Figure 3.4A2) and the highly detailed patient-specific volume conductor (Figure 3.2C) (Section 3.4.1). In addition, the bias in VTA-Astrom to underestimate the stimulation thresholds is likely because of the axon model used to generate this predictor (Appendix C and Section 3.2.3.2).

Alternatively, DF-Peterson is developed from an even more simplified volume conductor than that of the VTA PAMs, but it performed better. However, DF predictors are a 1-degree simplification from FC models, whereas VTA predictors are a 2-degree simplification. As such, DF predictors are able to take advantage of both the patient-specific extracellular potentials and the actual axonal trajectories in their threshold predictions.

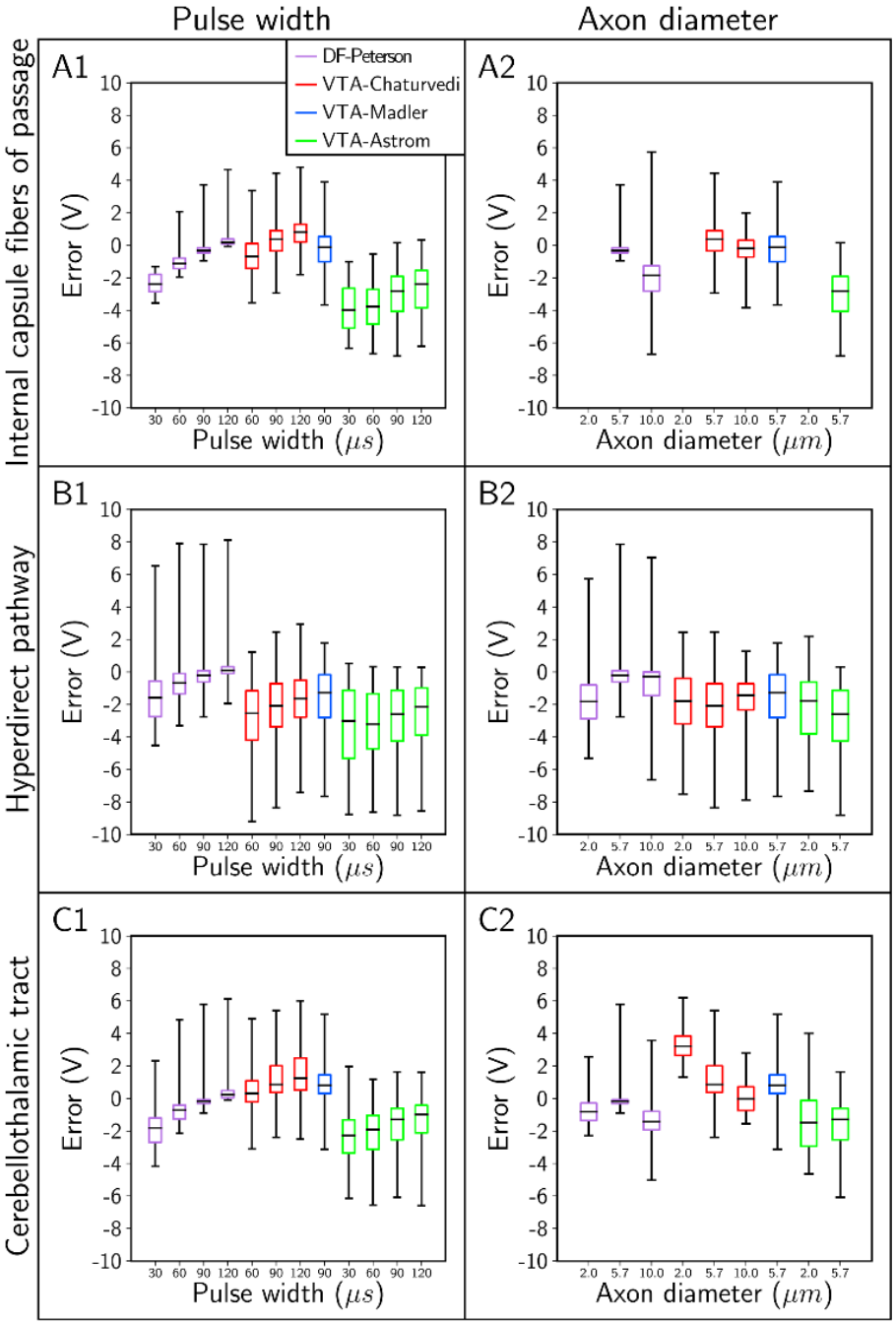

Figure 3.7. Absolute errors in the stimulation thresholds for a variety of stimulus pulse widths and axon diameters. We started with a stimulus pulse width of 90 µs, a monopolar electrode configuration of contact 2 (-) and case (+), and an axon diameter of 5.7 µm; and we varied each parameter individually. The absolute error in the stimulation threshold for each predictor is plotted for the different pulse widths (column 1), and axon diameters (column 2). Rows denote results for the: (A) internal capsule fibers of passage, (B) hyperdirect pathway, and (C) cerebellothalamic tract. Note: data was omitted when all stimulation thresholds were > 10 V.

3.3.2. Errors in pathway recruitment

Although the four predictors were unable to estimate accurately the stimulation thresholds of individual axons, the predictors could still, in some cases, accurately predict the percent activation of a given pathway (Figures 3.8 and 3.9). We bootstrapped the 933, 983, and 1,000 sampled axons of the IC, HDP, and CbTT pathways, respectively, into 100 subsamples of 1,000 axons for each pathway. Bootstrapping was implemented to assess how well the sampled axons represents the true population of axons within each pathway. The data presented represents the average and 2.5% to 97.5% quantiles of activated axons for the 100 subsamples in response to stimulation (Figures 3.8 and 3.9). These quantiles give an indication of the variability of the bootstrapped subsamples. The overlap of these quantiles between the predictor (i.e. DF-Peterson, VTA-Chaturvedi, VTA-Madler, VTA-Astrom) and the FC PAM indicates that in some, but not all, cases there is likely not a difference in prediction capability.

To account for the effect size, we elected to use the maximum absolute differences in pathway activation as the criteria for accuracy. We first designated a predictor as accurate if it estimated the percent activation of a given pathway to within 5% accuracy (on an absolute scale) at amplitudes of $\leq$ 10 V (Table 3.2). VTA-Astrom, because of its large bias in underestimating V_{th}, overestimated the percent activation of all pathways, regardless of the choice of stimulus pulse width (Figure 3.8) or axon diameter (Figure 3.9). VTA-Madler and VTA-Chaturvedi were also inaccurate for all of the cases tested. DF-Peterson,

although more accurate than all the VTA PAMs, still only satisfied our criterion for accuracy in 4 of the 18 cases.

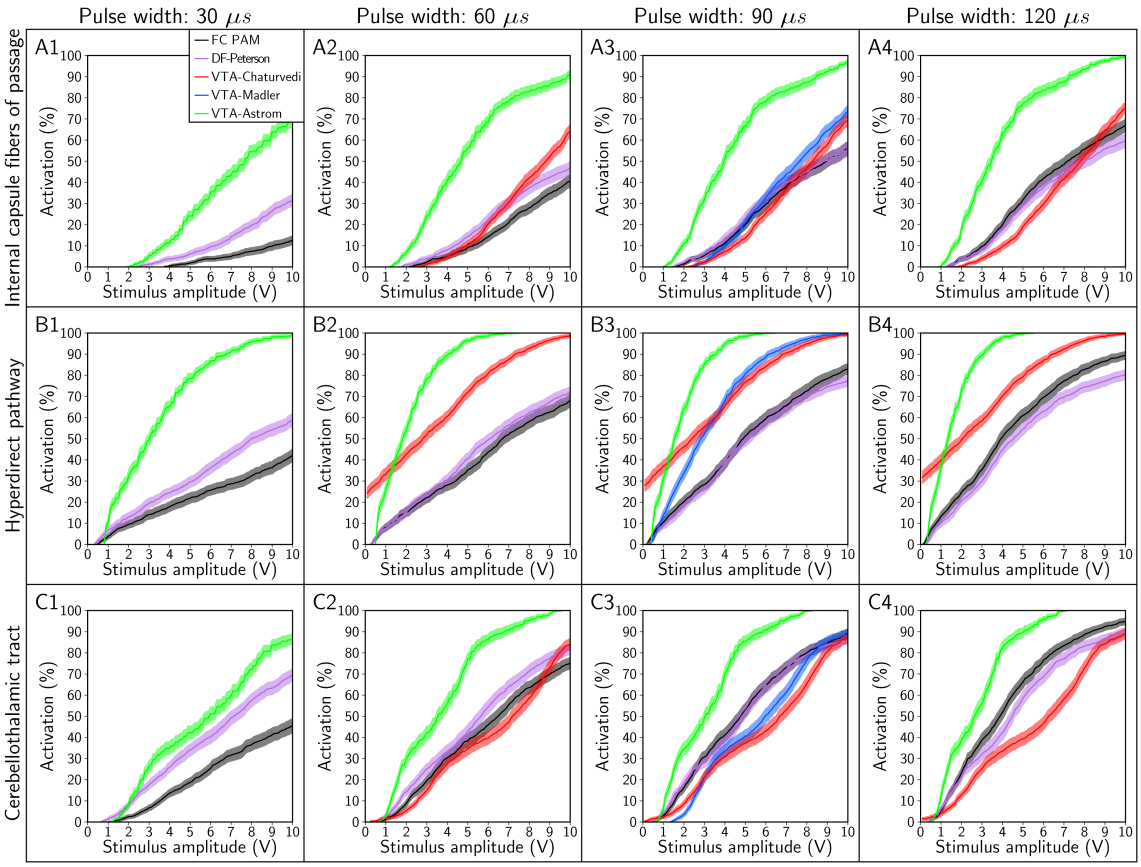

Figure 3.8. Recruitment curves generated with the FC, DF, and VTA PAMs for stimulus pulse widths of 30 µs, 60 µs, 90 µs, and 120 µs. Recruitment curves were calculated for the: (A) internal capsule fibers of passage, (B) hyperdirect pathway, and (C) cerebellothalamic tract. The electrode configuration was contact 2 (-), case (+) and axon diameter was 5.7 µm. The data presented represents the average and 2.5% to 97.5% quantiles of activated axons for the 100 subsamples in response to stimulation.

If we relaxed our criterion for accuracy to a maximum absolute error of 10%, we observed that DF-Peterson could satisfy 11 of the 18 cases, VTA-Chaturvedi could satisfy 2 of the 18 cases, and VTA-Astrom remained inaccurate in all cases. DF-Peterson was the only PAM accurate enough to capture the

monotonic trends of the recruitment curves in most cases. However, given that clinical/behavioral effects are typically noted at pathway activation levels beginning at ~10% [Chaturvedi et al., 2010; Gunalan et al., 2017], it is unclear if a 10% error tolerance is acceptable for clinical analyses.

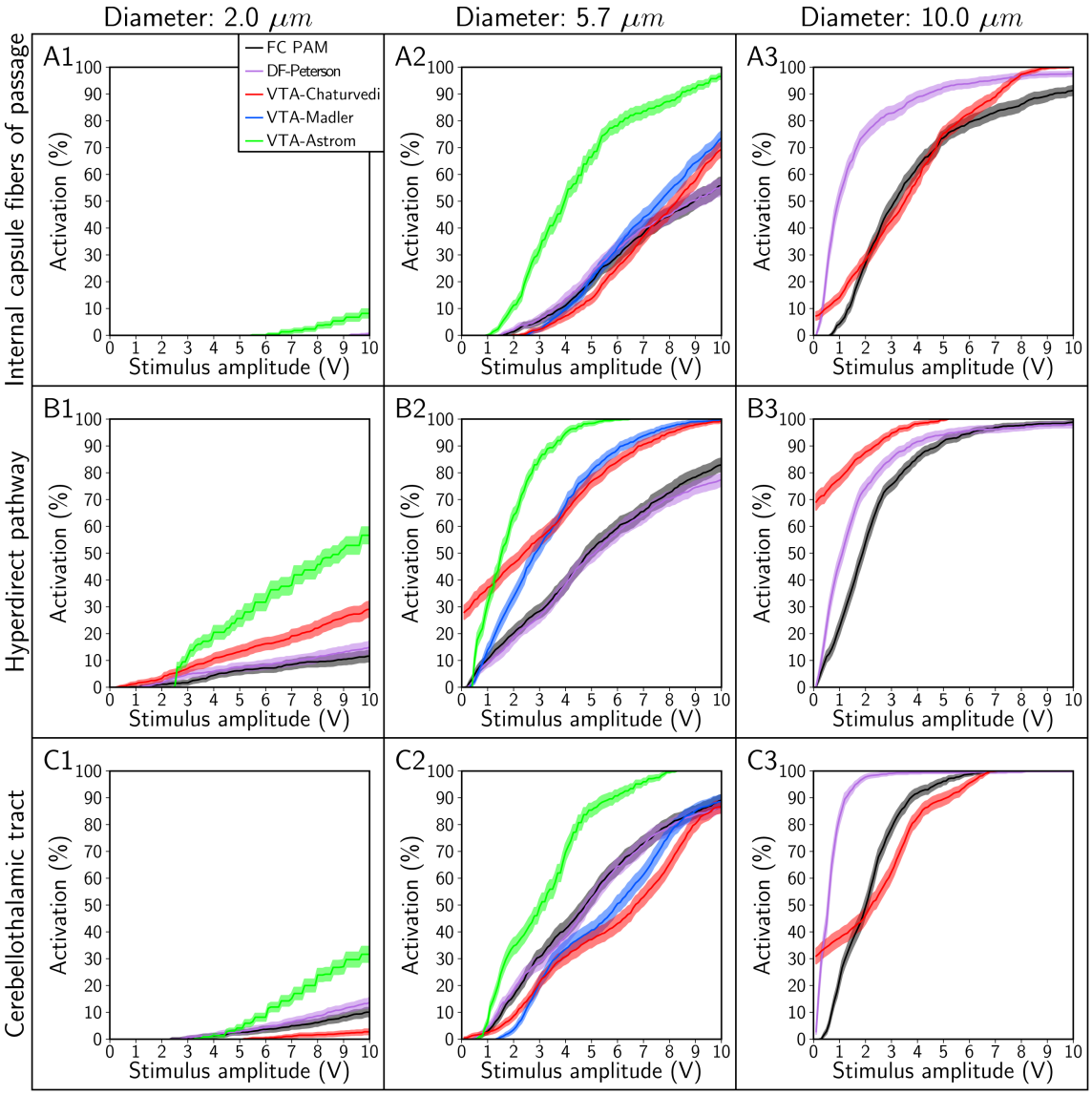

Figure 3.9. Recruitment curves generated with the FC, DF, and VTA PAMs for axon diameters of 2 µm, 5.7 µm, and 10 µm. Recruitment curves were calculated for the: (A) internal capsule fibers of passage, (B) hyperdirect pathway, and (C) cerebellothalamic tract. The stimulus pulse width was 90 µs and electrode configuration was contact 2 (-), case (+). The data presented represents the average and 2.5% to 97.5% quantiles of activated axons for the 100 subsamples in response to stimulation.

Table 3.2. Maximum absolute difference in percent activation between each predictor and the FC PAM, for the range of 0-10 Volts. This analysis is based on the data presented in the recruitment curves in Figures 8 and 9. '-' signifies that the predictor was not developed for the pulse width and axon diameter combination and 'X' signifies that the FC PAM predicted 0% activation for the entire range. Data is presented for the internal capsule fibers of passage (IC), hyperdirect pathway (HDP), and cerebellothalamic tract (CbTT).

Axon diameter (μm)	Pulse width (μs)	DF-Peterson			VTA-Chaturvedi			VTA-Madler			VTA-Astrom		
		IC	HDP	CbTT	IC	HDP	CbTT	IC	HDP	CbTT	IC	HDP	CbTT
2.0	**90**	X	3.3	3.7	X	17.4	7.4	---------	---------	---------	X	45.4	22.2
5.7	**30**	19.2	17.9	24.1	---------	---------	---------	---------	---------	---------	56.6	63.9	42.5
5.7	**60**	10.0	7.7	9.5	23.5	38.7	9.0	---------	---------	---------	58.6	62.7	41.9
5.7	**90**	3.3	5.7	4.0	13.5	28.7	22.4	17.8	31.1	15.5	50.4	58.1	34.7
5.7	**120**	7.3	9.6	10.3	13.6	32.1	29.9	---------	---------	---------	46.4	55.4	30.7
10.0	**90**	53.6	25.9	60.7	11.3	69.1	32.8	---------	---------	---------	---------	---------	---------

The 2.5% to 97.5% quantiles of each predictor did not overlap with the FC PAM at all amplitudes (0 V - 10 V) for all DBS relevant stimulus pulse widths (30 μs - 120 μs), electrode configurations (monopolar, bipolar, tripolar, quadripolar), and axon diameters (2 μm - 10 μm). This suggests that the activation calculations of all predictors are likely different from the gold standard FC PAM, for at least a portion of the parameter space tested. Thus, we have elected to use the FC PAM for analysis in the subsequent chapters.

3.4. Discussion

The goal of this study was to evaluate the relative accuracy of different methodologies for estimating pathway activation in the quantification of clinical DBS. We found that algorithms derived from simplified FC models have

substantial limitations in their predictive capabilities, especially VTA-based predictors which are commonly used in clinical DBS research. These results call into question the validity of numerous recent studies linking direct axonal activation with structural connectome results derived from diffusion-weighted imaging. Nonetheless, there exists a great scientific and clinical need to characterize the axonal pathways directly modulated by DBS, as well as their anatomical connections. Therefore, the conclusion of our analysis is that future connectomic DBS studies require far greater attention to the technical details of the DBS modeling strategy being used, as well as appropriate selection of a method that has the quantitative accuracy necessary for the desired analysis to be performed.

3.4.1. Pathway-activation models

Patient-specific models of DBS utilizing anatomically and electrically accurate volume conductor models and neuron models represent the most scientifically advanced tool for simulating the effects of DBS [Gunalan et al., 2017]. However, these field-cable pathway-activation models (FC PAMs) are so technically demanding to implement that their use in clinical research studies is greatly limited. The alternative is to use predictors derived from simplified DBS models, which impose various assumptions to speed up the simulations and reduce the complexity of implementation. DF PAMs represent a one-step reduction from FC PAMs, whereas VTA PAMs are a two-step reduction. Therefore, it is not surprising that the DF PAMs performed better than the VTA

PAMs in our analyses (Figure 3.5 and Appendix C). However, DF PAMs require constructing a volume conductor model, making them only moderately easier to implement than a corresponding FC PAM and thereby not widely used. VTA PAMs, on the other hand, are substantially easier to implement, and as a result, widely used in clinical DBS research.

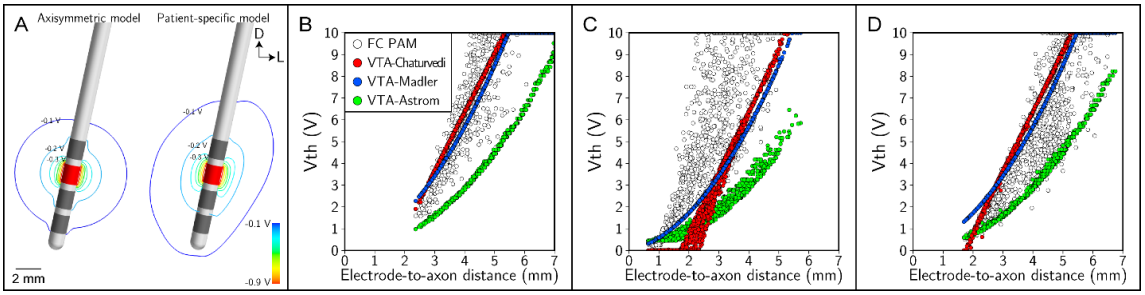

Figure 3.10. Axisymmetric versus patient-specific volume conductor models. (A) Isopotential contours for a -1 V stimulus amplitude created with (left) an axisymmetric model aligned to the trajectory of the patient-specific electrode and (right) the patient-specific model. (B-D) Strength-distance relationship of the threshold stimulus amplitudes for action potential initiation calculated with the FC and VTA predictors. Thresholds were calculated for the: (B) internal capsule fibers of passage, (C) hyperdirect pathway, and (D) cerebellothalamic tract. The stimulus pulse width was 90 µs, electrode configuration was contact 2 (-), case (+), and axon diameter was 5.7 µm. In this plot, we set axons with V_{th} > 10 V as 10 V, so that all axons representing a pathway can be visualized in the field of view. Note, electrode-to-axon distance is calculated from the center of the electrode contact.

The ease of implementing VTA PAMs facilitates their use in clinical research studies and DBS software tools designed to enable patient-specific analyses [Horn and Kuhn, 2015; Lauro et al., 2016; Noecker et al., 2017]. However, the simplifying assumptions and methodology used to create VTA PAMs can dramatically affect the subsequent predictions (Figure 3.5). VTA-based methods, more generally, are the product of two major simplifications. First, the electric field in a detailed patient-specific volume conductor model is

modulated by inhomogeneity and anisotropy in the electrical properties of the tissue (Figure 3.2), whereas VTA PAMs are derived from volume conductor models with a homogenous and isotropic tissue medium. Second, with a VTA-based method, the trajectories of surrounding axonal pathways represented are assumed to be perfectly straight and perpendicular to the electrode shaft (Figure 3.4A). These two simplifications impart symmetry in the model that generates a smooth and continuous "strength-distance" relationship (Figure 3.10 and Appendix C). However, more realistic DBS models generate substantial scatter in stimulation thresholds as a function of electrode-to-axon distance [Chaturvedi et al., 2010]. As a result, the corresponding fit of the VTA PAM to pathway recruitment is primarily dictated by how well it approximates the mean of the thresholds as a function of distance (Figure 3.10). In addition, VTA PAMs tend to do better simulating the response of relatively straight pathways (Figure 3.10B), but have more difficulty when the pathway trajectory is tortuous or branching (Figure 3.10C, 3.10D and Appendix C).

In general, we found that VTA PAMs performed relatively poorly when placed into a patient-specific context. However, if an appropriate method (i.e. VTA-Chaturvedi) is being used to estimate activation of an appropriate pathway (i.e. IC) at typical stimulation parameter settings (i.e. 60 μs, <5 V), it can perform very well (Appendix C). Nonetheless, those particular instances are limited, and our results reinforce the need to apply PAMs with care when using simplified algorithms or software tools that shield users from the technical details of the underlying model.

Unfortunately, simplified PAMs have not been used with care in the recent clinical DBS literature. They have been extended far beyond their design capabilities to perform analyses that are likely unsound. One glaring example is the use of activation volume tractography (AVT) (Figure 3.11). AVT defines an activation volume around a DBS electrode contact, uses the voxels contained within that volume as seeds for tractography, and then attempts to define connectivity between the VTA and different brain regions. However, this method, especially when applied in a grey matter region, actually violates numerous assumptions inherent to VTA-based methods [Butson and McIntyre, 2006]. In addition, blindly relying on tractography from a seed region to define connectivity is likely to generate a great deal of false positive results [Behrens et al., 2007; Morris et al., 2008; Thomas et al., 2014].

As an example of AVT and its shortcomings, we used AVT (with VTA-Chaturvedi) to evaluate thalamic connectivity and compared it to the corresponding FC PAM estimation of CbTT activation (Figure 3.11 and Appendix C). Not only did the percent activation predicted by the two algorithms not align, but the spatial trajectory of the resulting pathways were markedly different. Discrepancies with AVT were exacerbated even further when only excluding tracts that intersected the CSF or passed into the contralateral cerebral hemisphere, which is consistent with the tractography exclusion criteria typically used in clinical DBS studies using AVT (Figure 3.11B3). For example, aberrant streamlines from AVT passed above the thalamus before terminating in the VLpv (Figure 3.11B3). Therefore, we have found that minimizing the potential for

erroneous results requires first, the construction of the pathways of interest with appropriate anatomical constraints, and then the application of the predictor to estimate theoretical activation of the pathways.

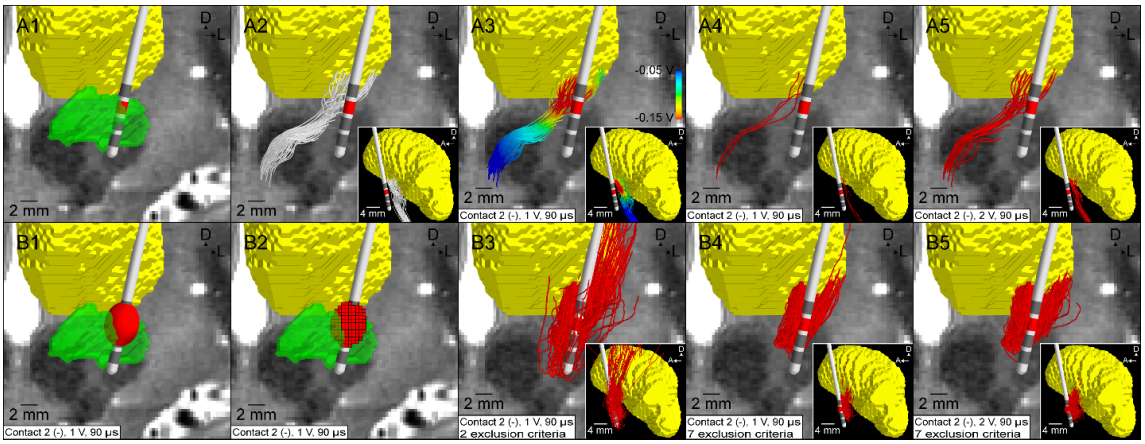

Figure 3.11. Errors inherent in activation volume tractography (AVT) of the cerebellothalamic tract. (A) FC PAM. (A1) T2-weighted image with overlaid DBS electrode (subthalamic nucleus - green, thalamus - yellow). (A2) Subsample of 100 streamlines representing the cerebellothalamic tract. (A3) Potentials from the volume conductor model were calculated at an applied voltage of 1 V, interpolated along the streamlines, scaled in space and time, and then used to stimulate the modeled axons. (A4) Axons activated by a 1 V stimulus (2.9 ± 0.5%). (A5) Axons activated by a 2 V stimulus (16.3 ± 1.1%). (B) Activation volume tractography. For clarity, only 10% of the streamlines generated are displayed. (B1) VTA-Chaturvedi predictor for a 1 V stimulus. (B2) Voxels whose centers are within the VTA/ellipsoid. (B3) Streamlines originating from the VTA shown in B2, terminating in the VLpv thalamus, and avoiding CSF and the contralateral cerebral hemisphere (16.0%). (B4) The same as B3 except subject to the same exclusion constraints used in the FC PAM, except for the subthalamic nucleus and DBS lead (13.7%) (Section 2.1.3). (B5) The same as B4 except for a 2 V VTA (15.1%). The same model parameters were used for both the FC PAM and AVT: pulse width = 90 µs; pulse frequency = 130 Hz; electrode configuration = contact 2 (-) and case (+); axon diameter = 5.7 µm.

One application where AVT may be somewhat more accurate is when it is used explicitly within large white matter pathways. Examples include DBS clinical research applications focused on neuropsychiatric targets such as the anterior limb of internal capsule or the subcallosal cingulate white matter. For

example, AVT from the subcallosal cingulate white matter generates predictions [Riva-Posse et al., 2017] that are qualitatively consistent with predictions from a patient-specific FC PAM [Lujan et al., 2013]. Nonetheless, AVT is likely not generalizable to all white matter regions, and we recommend that AVT methodology should not be used in future DBS research.

3.4.2. Limitations

The major limitation of this study is that no ground truth for model comparison actually exists. The patient-specific FC PAM that we used as our gold standard is the most detailed and advanced computational model of DBS ever created. However, while aspects of that model, such as the volume conductor and cable model, can be validated and constrained by experimental data [McIntyre et al., 2002; Miocinovic et al., 2009], the output predictions of pathway activation cannot be measured with current experimental techniques. It is possible to perform indirect measurements that can be used to evaluate model predictions, with electromyography (EMG) measurements corresponding to IC activation being the most easily attainable [Chaturvedi et al., 2010]. Recent clinical interest in using EMG to better characterize activation of the IC during subthalamic DBS [e.g. Mahlknecht et al., 2017; Bally et al., 2017], or cortically evoked electric potentials from HDP antidromic activation [e.g. Walker et al., 2012], represent excellent opportunities for the DBS modeling and clinical communities to converge on analyses that would be mutually beneficial.

Another limitation of our study was that the four predictors we analyzed only represent a subset of the different VTA and DF PAMs that are currently available. We chose VTA-Chaturvedi because it is more accurate and generalizable than previous VTAs [Chaturvedi et al., 2013]. VTA-Madler and VTA-Astrom were chosen because they are being utilized as scientific tools by a broader community of researchers studying DBS [e.g. Vanegas-Arroyave et al., 2016; Horn et al., 2017]. And, we chose DF-Peterson because it is the most accurate and generalizable DF-based method currently available [Peterson et al., 2011]. Therefore, our analyses, although not exhaustive, provide a best-case assessment of the performance of current predictive algorithms versus patient-specific FC PAMs.

Finally, a group of important limitations associated with modeling of DBS are the substantial errors that can arise from image co-registration [Klein et al., 2009], imprecise localization of the DBS electrode in a post-operative CT [Hemm et al., 2009], general ambiguity of tractography [Thomas et al., 2014], and uncertainty in various parameters used to define the patient-specific volume conductor model [Miocinovic et al., 2009; Howell and McIntyre, 2016]. However, by using the same underlying imaging data and model parameters for all of our simulations, we were able to hold constant these general errors and focus on quantifying the errors that come about from using a predictive algorithm in place of a full patient-specific FC PAM. Nonetheless, it should be noted that these general errors do come into play when connectomic DBS analyses are

performed across a population of subjects, especially if attempting to map population results into an atlas space.

3.5. Conclusions

Predictive algorithms that estimate the neural response to DBS do simplify the process of patient-specific pathway-activation modeling, but those simplifications come with the expense of a substantial decline in predictive accuracy. When parameters such as stimulus pulse width, electrode configuration, and axon diameter are matched, VTA-based methods offer a coarse estimate of the extent of activation but are subject to errors on the order of millimeters. Thus, current versions of these algorithms are likely not suitable for defining correlations between clinical metrics and stimulation of specific axonal pathways. While that same caveat probably applies to the currently available DF-based method, their general framework, with some additional customization for DBS studies, does hold promise for accurately estimating the percent activation of individual axonal pathways within a patient-specific context. Therefore, future connectomic DBS studies looking to strike a balance between model tractability and accuracy should transition away from VTA-based analyses and focus on developing and using DF-based tools.

Chapter 4 - Theoretical predictions of the axonal pathways directly activated by subthalamic deep brain stimulation

Abstract

Deep brain stimulation (DBS) is an established therapy for Parkinson's disease (PD). Experimental studies suggest that DBS activates neurons near the active electrode contact. However, the specific neurons mediating the therapeutic effects of DBS are not clearly defined. Biophysical models of DBS represent the only non-invasive method for calculating the neuronal pathways directly activated by stimulation in humans. In this study, we used these DBS models to evaluate our hypothesis that many pathways are activated by the clinically-defined therapeutic stimulation setting during subthalamic DBS and performed sensitivity analyses to determine the strength of our conclusions. We developed highly detailed patient-specific computational models of subthalamic DBS for three PD patients with 7T magnetic resonance imaging data. We reconstructed the trajectories of the subthalamopallidal, hyperdirect, internal capsule fibers of passage, cerebellothalamic, lenticular fasciculus, and medial lemniscus axonal pathways. Each of the axons within these pathways were modeled as a multi-compartment cable structure. We calculated the voltage distribution generated by the DBS electrode with the finite element method. We stimulated each axon with this DBS voltage distribution and calculated their response to stimulation. The results suggest that multiple pathways are activated by therapeutic stimulation, and these pathways were not consistent

among the three PD patients. Misalignments in the electrode position and the choice of axon diameter both effected the predictions of pathway activation, but the conclusions drawn were largely consistent for the entire parameter space investigated. Lastly, we evaluated alternative stimulation paradigms such as electrode configurations and stimulus pulse widths to explore methods for increasing selectivity in activation of these pathways. Electrode configuration and position has the greatest ability to change relative recruitment profiles. Subthalamic DBS likely activate multiple pathways indiscriminately and selectivity is dependent on the electrode position. Future studies need to focus on developing robust methods for reconstructing axonal pathways on a patient-specific basis and constraining the axon diameter used to represent each axon.

4.1. Introduction

Deep brain stimulation (DBS) of the subthalamic region is an established clinical therapy for Parkinson's disease (PD) [Benabid et al., 1994; Deuschl et al., 2006], but wide ranging scientific questions remain unanswered on its therapeutic mechanisms of action [Lozano and Lipsman, 2013; McIntyre and Anderson, 2016]. Numerous clinical research analyses of subthalamic DBS have clearly demonstrated that a major determinate of therapeutic outcome from the intervention is accurate electrode placement in the "target" [Butson et al., 2011; Welter et al., 2014; Eisenstein et al., 2014]. Unfortunately, scientific definition of the specific anatomical substrate for that "target" remains largely unknown. The subthalamic nucleus (STN) is surrounded by myelinated white matter consisting

of a wide array of different axonal pathways. Even within the STN boundaries, myelinated axons occupy ~45% of the sensorimotor territory of the nucleus [Mathai et al., 2013]. Therefore, while key aspects of subthalamic DBS therapy are now commonly attributed to the direct stimulation of axonal pathways, the specific axonal pathways of greatest therapeutic relevance remain to be defined.

Experimental and theoretical studies suggest that electrical stimulation in the generates action potentials in axons near the electrode contact [Ranck, 1975; McNeal, 1976]. Computational methods for studying the effects of DBS typically employ DBS electric field models coupled to models of individual axons to simulate action potential signaling in response to specific stimulation parameter settings [McIntyre et al., 2004]. These theoretical models, as well as empirical clinical observations, have subsequently suggested that many different axonal pathways in the subthalamic region are likely stimulated during therapeutic DBS, and prompted recent hypotheses that direct activation of different pathways may be linked to the control of different symptoms [Miocinovic et al., 2006; Coenen et al., 2011; Groppa et al., 2014]. In turn, it is possible that there are actually several different “targets” in the subthalamic region and the next level of scientific analysis requires a more detailed anatomical description of the relevant axonal pathways that might be stimulated during subthalamic DBS.

To address the detailed anatomy of the subthalamic region, characterize the axonal pathways, and evaluate the effects of stimulation, we used 7T magnetic resonance imaging (MRI) datasets to construct anatomically and biophysically detailed patient-specific DBS models. We hypothesized that

therapeutic stimulation would generate non-discriminate activation of multiple pathways, including the subthalamopallidal (SP), hyperdirect (HD), lenticular fasciculus (LF), and cerebellothalamic tract (CbTT) pathways. Further, we proposed that the spatial extent of therapeutic stimulation is primarily limited by avoiding activation of the internal capsule fibers of passage (IC) and medial lemniscus (ML) pathways, and not necessarily targeted activation of a specific therapeutic pathway.

4.2. Materials and methods

This study analyzed the theoretical activation of six axonal pathways by DBS electrodes implanted in the subthalamic region of three PD patients using field-cable pathway-activation models (FC PAMs). Each patient-specific FC PAM was constructed using the patient's 7T MRI datasets and included two main components: 1) a volume conductor model; and 2) multi-compartment cable models of axons. Highly detailed volume conductor models of DBS were built to calculate the DBS voltage distribution. Multi-compartment cable models of myelinated axons with anatomically realistic trajectories were stimulated with the DBS voltage distribution and their transmembrane voltage response was quantified as a function of the stimulation parameter settings. We explored the response of the SP, HD, LF, CbTT, ML, and IC axonal pathways. The workflow used to create each patient-specific model is detailed in Gunalan et al. [2017]. We briefly describe the steps below.

4.2.1. Ethics statement

Collection of all patient data for this study was approved by the University of Minnesota Institutional Review Board (IRB). The patients provided informed written consent prior to participating in the research and the consent procedure was approved by the IRB.

4.2.2. Patient data

The imaging data was individually acquired from three patients diagnosed with PD (Table 4.1). We selected patients who were implanted unilaterally on the left side of the brain. For each patient, a Medtronic 3389 DBS lead was implanted in the left STN (Figure 4.1) and connected to an Activa SC implantable pulse generator (IPG) (Medtronic, Minneapolis, MN). Using standard clinical programming procedures [Volkmann et al., 2002], therapeutic stimulation parameters were selected for each patient. The patient-specific stimulation parameter settings we evaluated were defined at least 4 months after their surgery, ensuring adequate time for clinical optimization. The DBS electrode monopolar impedances, as measured by the IPG [Gunalan et al., 2017], were also noted. The post-operative OFF medication, OFF stimulation motor subscore of the Unified Parkinson's Disease Rating Scale (UPDRS) were compared to the ON medication, ON stimulation scores (Table 4.2).

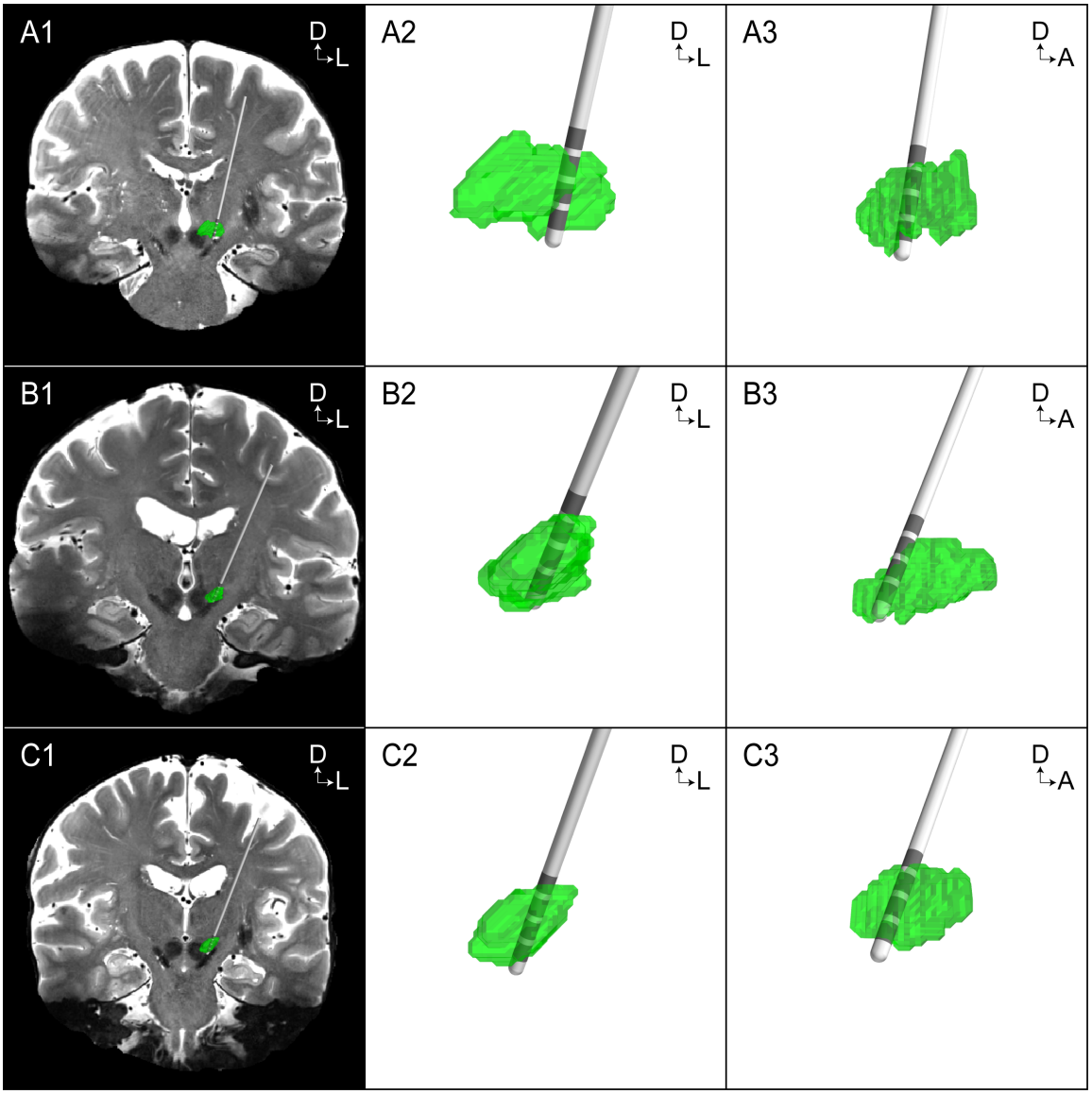

Figure 4.1. Deep brain stimulation lead locations within the subthalamic nucleus. (A-C) Patients 1-3. (Column 1) Coronal slice directly posterior to the subthalamic nucleus (STN, green). (Column 2) Coronal and (Column 3) sagittal zoomed views of electrode contact locations within the STN. Dorsal – D, Lateral – L, Anterior – A.

Table 4.1. Patient demographic data. Monopolar impedance measurements were obtained from the Medtronic IPG programmer. IPG = implantable pulse generator. STN = subthalamic nucleus.

Patient	Gender	Handedness	Age at diagnosis	Age at implant	Electrode location	Medtronic IPG	Electrode contact impedance measurement (Ω)					Clinically-determined stimulation setting			
							Months post implant	0	1	2	3	Electrode configuration	Pulse frequency (Hz)	Pulse amplitude (V)	Pulse width (μs)
1	Male	Right	58	67	Left STN	Activa SC	4	2000	1627	1450	1896	c2(-), case(+)	130	1.7	60
2	Male	Right	49	58	Left STN	Activa SC	4	1168	1147	1300	1337	c2(-), case(+)	130	2.0	60
3	Female	Right	55	63	Left STN	Activa SC	4	1684	1499	1099	1493	c2(-), case(+)	130	2.4	60

Table 4.2. Unified Parkinson's Disease Rating Scale motor subscore.MED = Antiparkinsonian medication. DBS = deep brain stimulation.

Patient	Months post implant	OFF MED/OFF DBS	OFF MED/ON DBS	ON MED/OFF DBS	ON MED/ON DBS
1	4	31	Not available	Not available	14
2	3	36	27	14	12
3	7	43	32	32	20

Table 4.3. Model monopolar impedance calculations. R_{Tissue} is the access resistance of each contact. R_{70} is the model impedance measurement mirroring the Medtronic programmer.

Patient	σ (S/m)	R_{Tissue} (Ω)	R_{70} (Ω)
		Contact 2	Contact 2
1	0.07	1373	1493
2	0.09	1168	1286
3	0.12	969	1085

4.2.3. Image processing

Each patient underwent pre-operative scanning on a 7T MRI system (Magnex Scientific, UK) at the University of Minnesota, using T1-weighted (T1W), T2-weighted (T2W), susceptibility-weighted (SW), and diffusion-weighted (DW) imaging. We also obtained a pre-operative T1W image on a 1.5T Siemens Magnetom Espree. The T2W and SW images were acquired in slabs focused around the basal ganglia nuclei in both the coronal and axial orientations with an in-plane resolution of ~0.4 mm. A post-operative CT image was acquired on a Siemens Biograph64 Sensation approximately 1 month after the DBS surgery.

The 1.5T T1W image was resliced to 0.4 mm isotropic dimensions to match the in-plane resolution of the 7T images. All images were registered to the common space of the resliced 1.5T T1W image using ANTS or FSL. The DW images were corrected for distortions from both magnetic field inhomogeneities and eddy currents.

Segmentation of the STN, substantia nigra, and red nucleus was performed on the coronal 7T T2W or SW image. These segmentations were transformed to the T1W common space. These segmentations were thresholded at 0.5 and binarized. As no image provided adequate contrast for segmentation of the thalamus, we fit the Harvard-Oxford atlas thalamus to each patient using Cicerone [Miocinovic et al., 2007].

4.2.4. Field-cable pathway-activation model

4.2.4.1. Volume conductor model

The voltage distribution generated by the DBS electrode varies both spatially and temporally in the brain [Miocinovic et al., 2009]. Therefore, we created detailed volume conductor models in COMSOL to account for the tissue anisotropy and inhomogeneity in the human head (Figure 4.2) [Gunalan et al., 2017]. We defined boundaries of the brain and the outer skin by segmenting the 1.5T T1W image with FSL's brain extraction tool (Figure 4.2A). We defined the position of the model DBS lead based on the artifact in the post-operative CT, registered to the T1W common space [Hemm et al., 2009]. We fitted diffusion tensors to the patient-specific DW images using FSL diffusion tensor fitting tool. Using these diffusion tensors and the tissue-type segmentation of the head (Figure 4.2B), we defined anisotropic conductivities within the boundaries of the brain using the load preservation approach [Howell and McIntyre, 2016], and isotropic conductivities outside of the brain (Figure 4.2C) [Howell and McIntyre, 2017]. We defined the encapsulation layer with a 0.5 mm radius around the entire electrode shaft, and defined the isotropic conductivity of the encapsulation layer such that the model impedance (Table 4.3) best matched the clinical impedance (Table 4.1) at the therapeutic electrode contact [Gunalan et al., 2017]. We applied a Dirichlet boundary condition at the active contact(s). For monopolar configurations, the anode was set to the be neck surface (Figure 4.2A). Neumann boundary conditions of 0 A/mm^2 were imposed along the electrode shaft, except for the contacts, and at the outer skin surface, except for

the neck during monopolar configurations. We solved for the electrostatic solution of Laplace's equation using the finite element method.

We then calculated the temporal modulation of the voltage distribution using an equivalent electrical circuit model for voltage-regulated DBS, such that the modeled stimulus waveform matched the waveform of the Medtronic IPG [Lempka et al., In review]. For each pulse, the applied rectangular waveform consisted of a cathodic phase, interphase interval, passive recovery phase, and interpulse interval. This stimulus waveform was then calculated for a pulse train, and the pulse train was applied to the axon models.

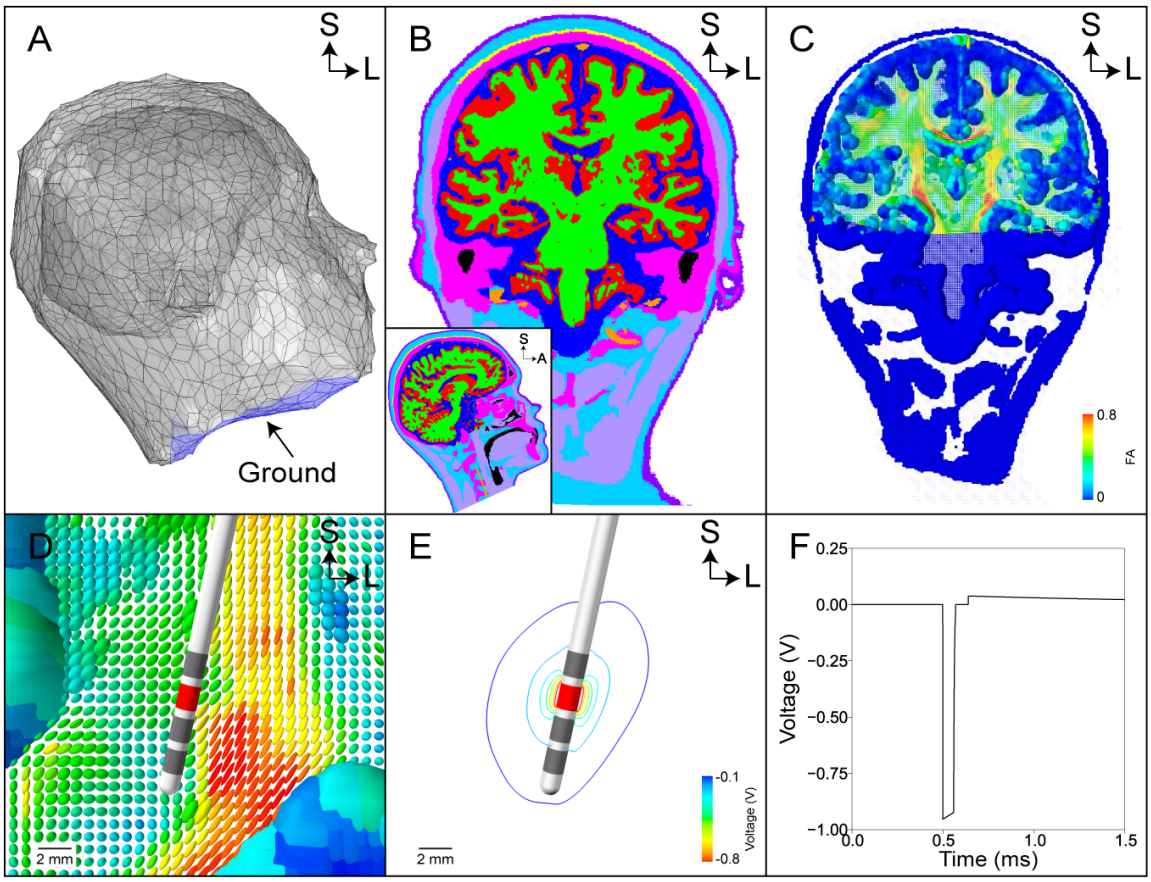

Figure 4.2. Patient-specific deep brain stimulation volume conductor model. (A) Outer head and brain boundaries. Under monopolar configurations the neck is defined as 0 V (blue). (B) Tissue-type segmentation of the head. (C) Conductivity tensors within the head, colored according to their fractional anisotropy (FA). (D) Zoomed view of the conductivity tensors near the electrode. (E) DBS voltage distribution isolines for a 1 V stimulus amplitude at contact 2. (F) Stimulus waveform at the electrode-tissue interface for a 1 V, 60 μs, and 130 Hz.

4.2.4.2. Axonal reconstructions

We constructed multi-compartment cable models of myelinated axons to represent six pathways in the subthalamic region (Figure 4.3). We used probabilistic tractography to define the trajectory of each axon in the HD, CbTT, ML, and IC pathways. FSL's probabilistic tractography tool (probtrackx) generated trajectories, or 'streamlines', which originated in the seed mask and

terminated in the target mask(s) (Table 4.4). Of the thousands of streamlines that were generated for each pathway, we randomly sampled 1,000 for use in each specific pathway representation. We fit a smoothing spline to each tractography-generated streamline to ensure a smooth trajectory for use in the stimulation modeling [Gunalan et al., 2017].

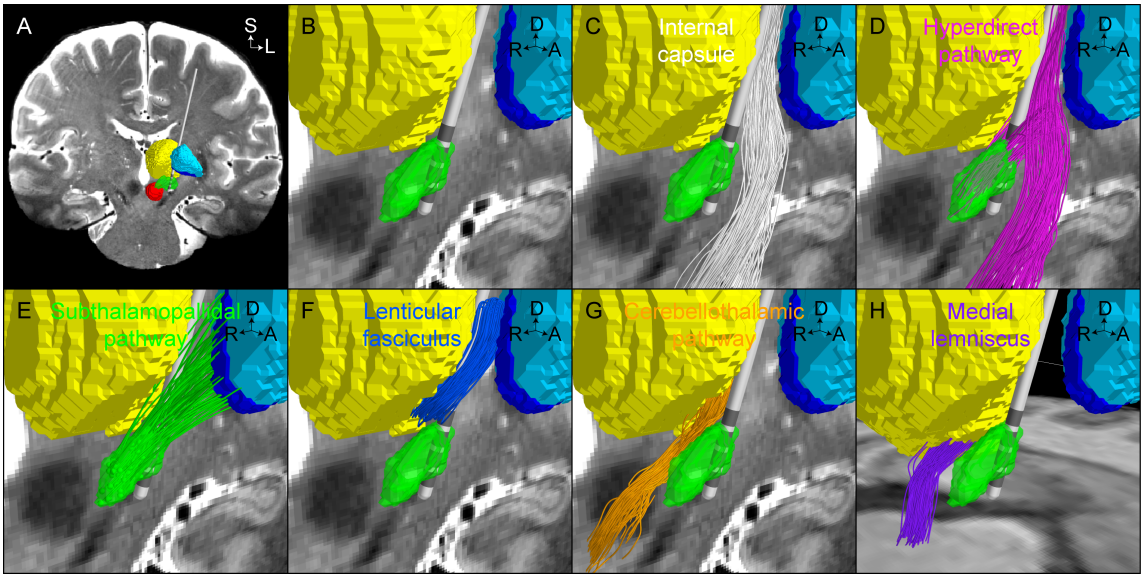

Figure 4.3. Axonal pathways in the subthalamic region. Data is presented for Patient 1. (A) Coronal view of the T2W image, DBS lead, and subcortical nuclei (thalamus – yellow, globus pallidus externus – light blue, globus pallidus internus – dark blue, subthalamic nucleus – green, substantia nigra – pink, red nucleus – red). (B) Oblique zoomed view of the subthalamic region. One hundred representative streamlines reconstructed for the (C) internal capsule fibers of passage, (D) hyperdirect, (E) subthalamopallidal, (F) lenticular fasciculus, (G) cerebellothalamic tract, and (H) medial lemniscus pathways.

Table 4.4. Properties of streamlines representing each pathway. Corticofugal axons represent the axons of the internal capsule fibers of passage and hyperdirect pathway. GP – globus pallidus, GPi – globus pallidus internus, Pu – putamen, STN – subthalamic nucleus, SN – substantia nigra, RN – red nucleus, SCP – superior cerebellar peduncle.

	Tractography				
Pathway	Seed mask	Target mask(s)	Exclusion masks	Seeds per voxel	Axon diameter (μm)
Corticofugal axon	White matter near STN	White matter near thalamus; White matter in cerebral peduncles	GPe, Pu, RN, SN, thalamus, CSF	100	5.7
Hyperdirect pathway – Collateral section	Corticofugal axon	STN	SN, thalamus	N/A	1.8
Subthalamopallidal	STN	GP	SN, thalamus	1	2.0
Lenticular fasciculus	GPi	VLa	N/A	N/A	2.0
Cerebellothalamic tract	SCP	VLpv	GP, STN, SN, VLa, VPL, CSF	2000	5.7
Medial lemniscus	Brainstem	VPL	GP, STN, SN, RN, VLa, VLpv, LP, CSF	1000	5.7

For the hyperdirect pathway axons, we modeled the collateral as a branch at a randomly chosen node of Ranvier along the corticofugal axon that was within 3 mm in the dorsal-ventral direction from the dorsal boundary of the STN. A random voxel within the STN was selected as the termination point of the collateral. We then generated an arc connecting the branch point node of Ranvier and the termination point within the STN to define the collateral trajectory. If the collateral passed through the DBS lead, we randomly selected a different voxel within the STN and recalculated the corresponding arc.

Despite our extensive efforts, tractography failed to generate anatomically realistic axonal trajectories for the SP and LF pathways. These relatively small pathways cross the IC, thereby making their reconstruction very difficult, even with exceptionally high quality DWI data. Therefore, instead of using streamlines that we knew were not consistent with anatomical tracing studies [Sato et al.,

2000; Parent et al., 2004; Gallay et al., 2008], we elected to create populations of stylized trajectories guided by anatomical landmarks [Miocinovic et al., 2006; Chaturvedi et al., 2012].

For Patient 1, we segmented the globus pallidus internus, globus pallidus externus, and putamen from the axial 7T T2W image in T1W common space. The SP stylized streamlines originated from each voxel within the subthalamic nucleus and terminated in a random voxel in the globus pallidus. The LF stylized streamlines originated in the globus pallidus internus, crossed the IC, coursed dorsally over the STN, and projected into the VLa thalamic nucleus. In order to create a consistent reconstruction of the LF we generated a set of 2,000 streamlines in Patient 1 space and transformed those streamlines to each subsequent patient space. This transform was defined by fitting Patient 1's globus pallidus and thalamus to Patient 2 and 3 using 9 degree of freedoms. Additionally, we used the globus pallidus fitting in Patient 2 and 3 as exclusion masks in subsequent patient-specific tractography reconstructions of the other pathways. Of the 2,000 stylized streamlines for LF, we ignored those that intersected the DBS lead. We subsampled 1,000 streamlines of the LF and SP to represent each of these pathways.

4.2.4.3. Cable model of axons

The geometric and electrical parameters of all axon models were defined from previously established models [McIntyre et al., 2002; Howell and McIntyre, 2016]. The myelinated axon was modeled with a double cable structure. The

nodes of Ranvier had voltage-gated fast Na^+, persistent Na^+, and slow K^+ ion channel conductances, leakage conductance, and, membrane capacitance properties. The axon models for the various pathways were assigned a single diameter (Table 4.4). Given that local projection neurons can respond differently than fibers of passage to electrical stimulation [McIntyre and Grill, 2000; Foutz and McIntyre, 2010], we attached a 20 μm diameter soma with passive membrane properties to the first node of Ranvier of each SP axon.

The response of each individual axon model in each modeled pathway to the spatially- and temporally-varying DBS voltage distribution was calculated with NEURON [Hines and Carnevale, 2001]. We used a binary search algorithm to determine the threshold stimulus amplitude that was sufficient for generating propagating action potentials at the distal nodes to a train DBS stimuli at 130 Hz.

From these threshold stimulus amplitudes, we constructed recruitment curves representing the percent activation of the pathway as a function of stimulus amplitude. We bootstrapped the sampled axons of each pathway into 100 subsamples of 1,000 axons. Bootstrapping was implemented to assess how well the sampled axons represents the true population of axons within each pathway. The data presented represents the average and 2.5% to 97.5% quantiles of activated axons for the 100 subsamples in response to stimulation (Figure 4.4). These quantiles give an indication of the variability of the bootstrapped subsamples. The overlap of these quantiles between different pathways indicates that there is likely not a difference in activation.

4.3. Results

We developed highly detailed computational models of subthalamic DBS for three PD patients. The type of computational model constructed for this study, known as a FC PAM [Gunalan et al., 2017], explicitly calculates the response of cable axon models with anatomically realistic trajectories to the DBS voltage distribution. To construct these FC PAMs, we generated the trajectories of six pathways in the subthalamic region, modeled each axon within these pathways as a multi-compartment cable structure, and calculated the response of each axon to the voltage distribution generated by the DBS electrode. We retrospectively used these models to evaluate our hypothesis that the clinically-defined therapeutic stimulation setting selectively activates the HD and SP pathways over the LF, CbTT, IC, and ML pathways, and performed sensitivity analyses to determine the robustness of our conclusions. Lastly, we evaluated alternative stimulation paradigms to explore possibilities for increasing the stimulation selectivity of these pathways.

4.3.1. Activation of Multiple Pathways

We calculated the activation of axonal pathways in the subthalamic region to the clinically-defined therapeutic stimulation setting (Figure 4.4). We found that therapeutic stimulation activates multiple pathways and these pathways were not consistent among the three PD patients. For instance, in Patient 1 the HD was activated at a higher percentage than the SP and CbTT pathways, but in Patient 3 the LF was activated at a higher percentage than the HD and SP

pathways. We then explored the effects of changing the stimulus amplitude from 0 to 6 V in each patient and created recruitment curves for each pathway. The results demonstrate that the relative proportions of each pathway can be biased by amplitude changes.

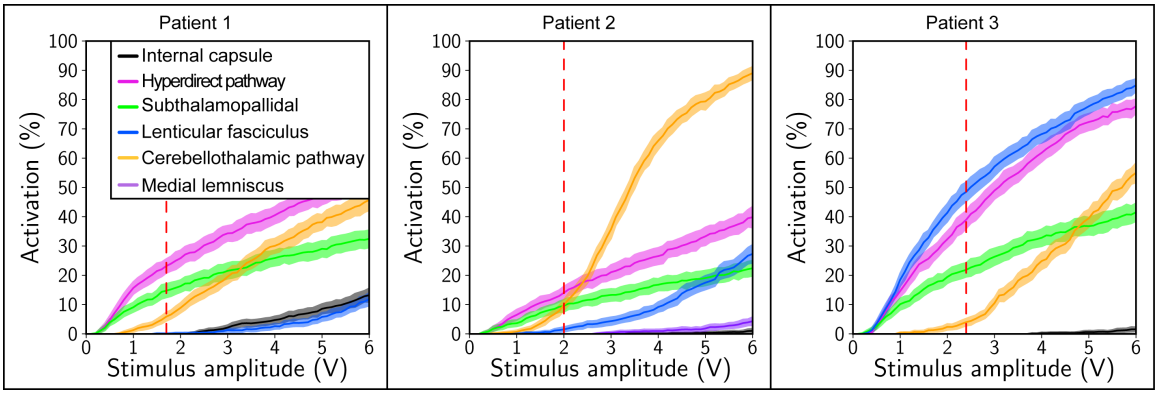

Figure 4.4. Pathways activated by the clinically-defined therapeutic stimulation setting for each patient. Recruitment curves for monopolar stimulation with contact 2 (60 μs, 130 Hz). Red dashed line represents the clinically-defined therapeutic stimulation setting. Internal capsule fibers of passage – white; hyperdirect pathway – pink; subthalamopallidal pathway – green; lenticular fasciculus – blue; cerebellothalamic tract – orange; medial lemniscus – purple. The data presented represents the average and 2.5% to 97.5% quantiles of activated axons for the 100 subsamples in response to stimulation.

Next, we evaluated the sensitivity of the model predicted pathway activation results to two key parameters: electrode location and axon diameter. We shifted the location of the DBS electrode by 0.5 mm in the anterior-posterior, dorsal-ventral, and medial-lateral directions in Patient 1 (Figure 4.5). The relative trends in activation of the SP and HD pathways stayed consistent with shifts of the DBS lead. However, pathways that were located on one side of the DBS lead (e.g. CbTT pathway) were sensitive to changes in DBS lead position. Additionally, we modeled all axons within the IC, HD, and ML pathways with

diameters of either 2 μm, 4 μm, 5.7 μm, 8 μm, or 10 μm, and all axons within the SP, LF, and CbTT pathways with diameters of either 2 μm, 4 μm, 5.7 μm (Figure 4.6). For all pathways, the pathway activation was extremely sensitive to the choice of axon diameter. In some cases, the predicted activation changed from 0% to ~50% as the diameter change from 2 μm to 5.7 μm. Thus, both electrode location and axon diameter have an impact on pathway activation predictions. However, the basic model prediction that both the HD and SP pathways are in Patient 1 activated during therapeutic stimulation appears robust.

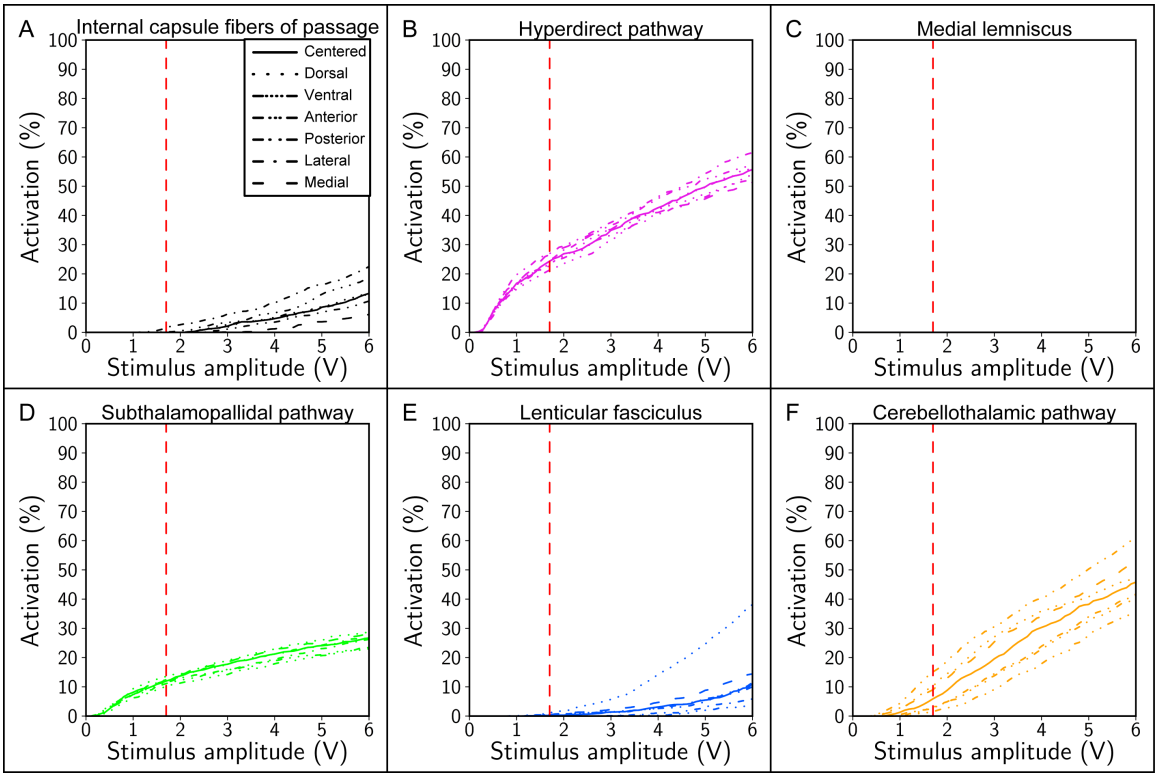

Figure 4.5. Sensitivity of pathway activation to electrode localization. The modeled DBS electrode was shifted by 0.5 mm in a given direction. Data is shown for Patient 1. Red dashed line represents the clinically-defined therapeutic stimulation setting. Stimulation parameters: voltage-controlled stimulation; contact 2 (-), case (+); 60 μs; 130 Hz.

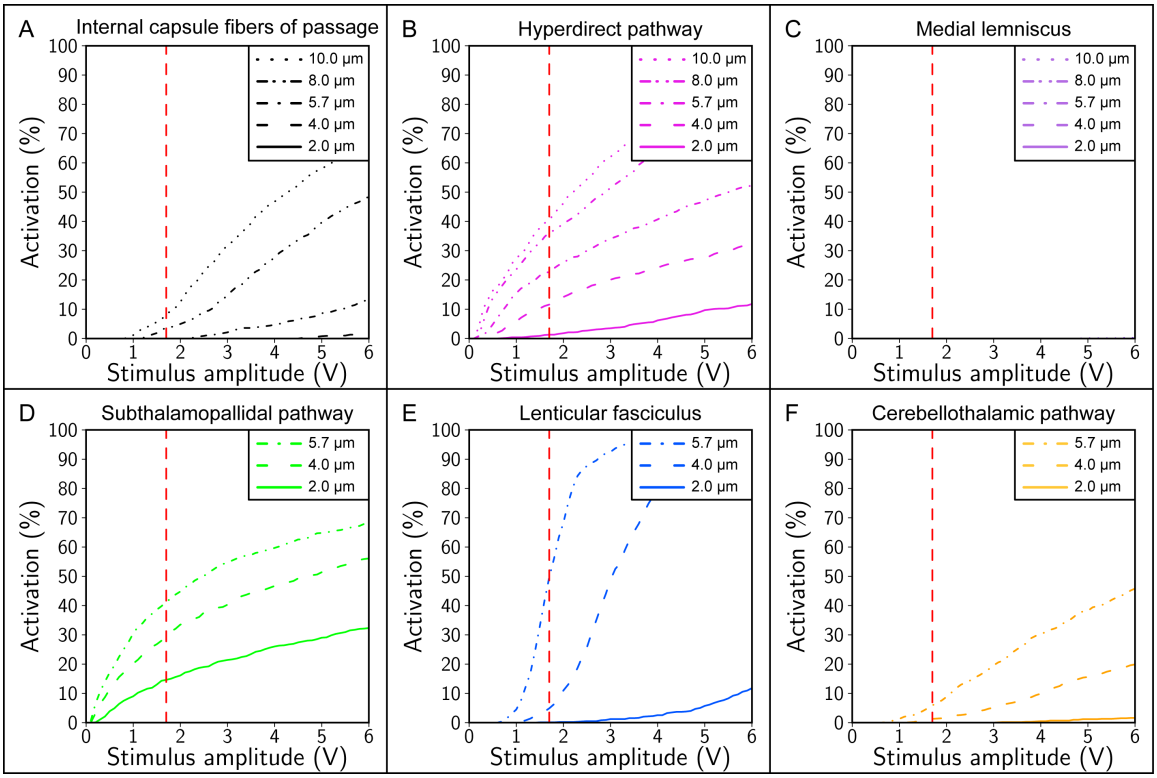

Figure 4.6. Sensitivity of pathway activation to axon diameter. Activation of the (A) internal capsule fibers of passage, (B) hyperdirect pathway, (C) medial lemniscus, (D) subthalamopallidal pathway, (E) lenticular fasciculus, and (F) cerebellothalamic tract. All axons within a pathway were modeled as a single diameter. Data is shown for Patient 1. Red dashed line represents the clinically-defined therapeutic stimulation setting. Stimulation parameters: voltage-controlled stimulation; contact 2 (-), case (+); 60 µs; 130 Hz.

4.3.2. Alternative stimulation paradigms

The clinically-defined therapeutic stimulation setting for Patient 1 was contact 2 (-)/case (+), 1.7 V, 60 µs, and 130 Hz. We explored the use of alternative stimulus pulse widths, electrode configurations, and current-controlled stimulation on the activation of the aforementioned 6 pathways for Patient 1. We calculated the activation of these pathways with either 30 µs, 60 µs, 90 µs, and 120 µs pulse widths (Figure 4.7). We found that as the amplitude increased the SP and HD pathways were activated before any other pathway for all stimulus

pulse widths. Subsequently, we calculated activation of these pathways for four monopolar and four adjacent bipolar electrode configurations (Figure 4.8). For all electrode configurations tested, the SP and HD pathways were activated before any other pathway. However, by shifting the active monopolar electrode contact from contact 2 to contact 3 the LF increased activation for 1.7 V from 0.1% to 19.0%. This change is reflective of the position of contact 3 in the region dorsal to the STN. As contact 2 was located within the dorsal portion of the STN in Patient 1, the SP and HD pathways were most likely to be activated.

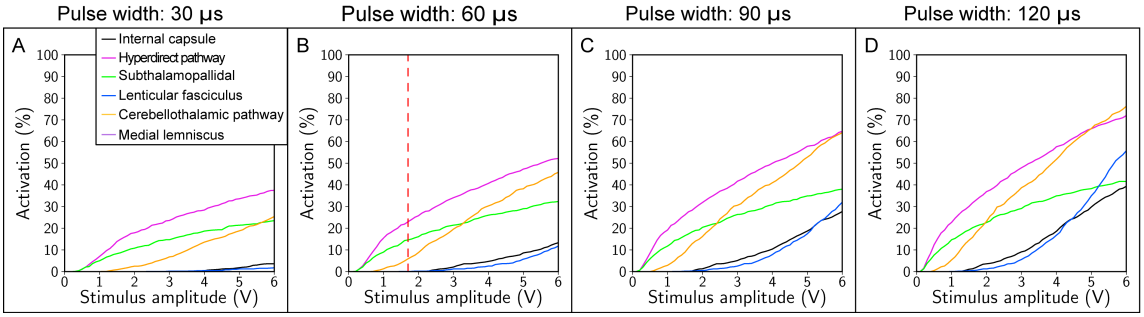

Figure 4.7. Effect of stimulus pulse width on pathway activation. (A-D) Activation was calculated for 30 µs, 60 µs, 90 µs, and 120 µs stimulus pulse widths. Data is shown for Patient 1. Red dashed line represents the clinically-defined therapeutic stimulation setting. Stimulation parameters: voltage-controlled stimulation; contact 2 (-), case (+); 130 Hz.

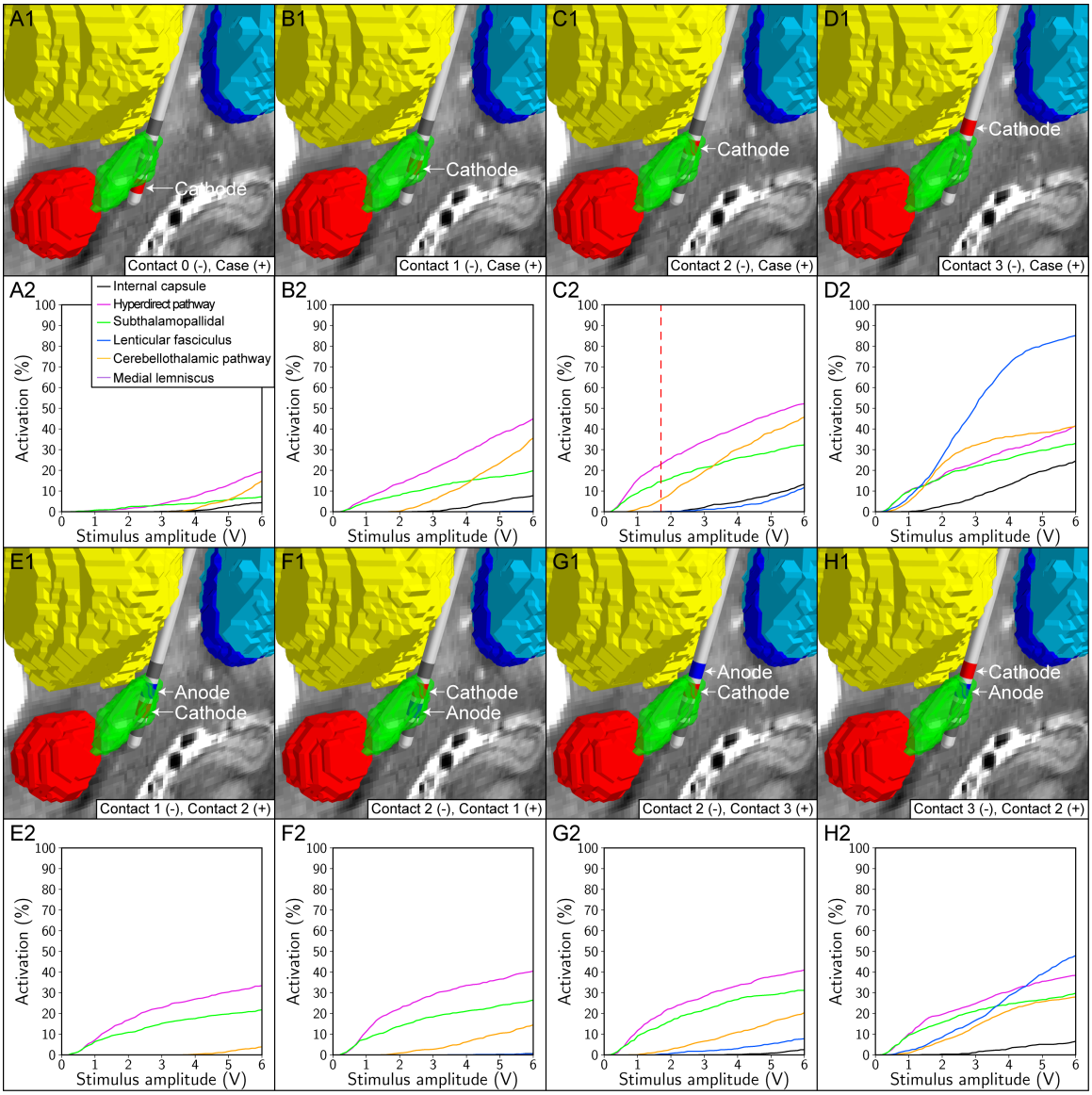

Figure 4.8. Effect of electrode configuration on pathway activation. Activation was calculated for (A-D) monopolar and (E-H) bipolar electrode configurations. Data is shown for Patient 1. Red dashed line represents the clinically-defined therapeutic stimulation setting. Stimulation parameters: voltage-controlled stimulation; 60 μs; 130 Hz.

Studies have shown that the DBS electrode impedances change over time [Cheung et al., 2013; Hartmann et al., 2015]. Impedance changes are likely due to a glial scar formation around the DBS lead [Grill and Mortimer, 1994]. Previous studies have shown that current-controlled systems can reduced the

variability of the stimulus waveform measured in the brain as the electrode impedance changes [Lempka et al., 2010]. We changed the encapsulation layer conductivity to reflect this impedance change and calculated activation of the CbTT pathway during voltage- and current-controlled stimulation (Figure 4.9). We modeled the encapsulation layer as a 0.5 mm radius around the entire DBS lead with a homogenous conductivity of either 0.05 S/m, 0.07 S/m, or 0.20 S/m, which resulted in an access resistance of 1.69 kΩ, 1.37 kΩ, or 0.82 kΩ. For voltage-controlled stimulation, we found that as the encapsulation layer conductivity decreased the activation of the CbTT pathway also decreased. For current-controlled stimulation, activation of the CbTT pathway was largely insensitive to changes in encapsulation layer conductivity.

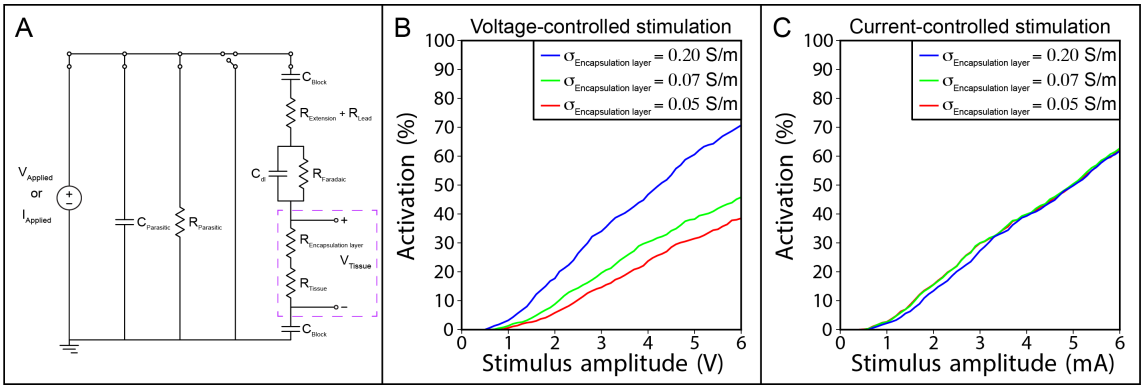

Figure 4.9. Analysis of voltage- and current-controlled stimulation. (A) An equivalent electrical circuit of the implanted DBS system for monopolar stimulation [Lempka et al., In review]. The brain is represented as a series resistance of the encapsulation layer ($R_{Encapsulation\ layer}$) and bulk tissue (R_{Tissue}) (dashed purple line). (B) Activation of the cerebellothalamic tract for voltage-controlled stimulation. We defined the encapsulation layer conductivity as either 0.05 S/m, 0.07 S/m, or 0.20 S/m. (C) Activation of the cerebellothalamic tract for current-controlled stimulation.

4.4. Discussion

We constructed anatomically and biophysically detailed models of subthalamic DBS to predict the pathways that mediate the therapeutic response to stimulation. The model results suggest that multiple pathways are robustly activated by the clinically-defined therapeutic stimulation setting and these pathways were not consistent among the three PD patients. These general conclusions hold true for potential errors in electrode localization and axon diameter choice, but these parameters have an appreciable influence on activation percentage. Future studies will need to focus on constraining parameters such as the distribution of axon diameters within a pathway to produce physiological accurate predictions of pathway activation.

4.4.1. Implications for identifying a therapeutic target

The clinical literature has made clear that the major determinate of therapeutic outcome from DBS interventions is accurate electrode placement in the "target", commonly defined in anatomical terms as the dorsal-lateral STN [e.g. Welter et al., 2014; Eisenstein et al., 2014]. However, scientific definition of the neural elements making up the "target" for subthalamic DBS has taken many different faces over the last two decades. The original concept of simply stimulating the cell bodies of the STN [Limousin et al., 1995], eventually evolved to stimulating the efferent axons of the STN neurons [Miocinovic et al., 2006]. In addition, recognition that many different axonal pathways in the subthalamic region are likely stimulated during therapeutic DBS prompted hypotheses that

stimulation of different pathways may be linked to the control of different symptoms [Coenen et al., 2011; Chaturvedi et al., 2012]. Plus, basic neuroscience investigations using optogenetics in rodents have recently highlighted the important role of directly stimulating afferent axonal inputs, most notably hyperdirect axon collaterals in the STN [Gradinaru et al., 2009; Sanders and Jaeger, 2016]. In turn, it is likely that there are many different "targets" in the subthalamic region.

The models developed in this study provided a framework for us to address to the basic question of what pathways are being stimulated (Figure 4.4). Our calculations suggest that directly stimulating the SP, HD, and CbTT pathways are necessary for therapeutic effect; however, our models cannot determine if one or the other is sufficient. Unfortunately, it does not appear easy to disentangle activation of the HD and SP pathways with electrical stimulation, as our attempts to explore alternative stimulation paradigms yielded coupled activation for all conditions (Figure 4.8). Therefore, we must look to additional metrics and methods to identify if stimulating one of these pathways is more important than the other in terms of therapeutic efficacy. One option could be to use correlations of electrophysiological evoked potentials in the connected nuclei (i.e. cortex and pallidum) with clinical measurements of benefit. Such experiments have been done in the human cortex (see Chapter 5) [Walker et al., 2012; de Hemptinne, 2015] with positive results, but corresponding results in pallidum remain to be acquired.

4.4.2. Implications for stimulation parameter selection

In this study, we used patient-specific FC PAMs to provide insights on theoretical activation of pathways in the subthalamic region. We explored the use of a range of stimulus pulse widths, electrode configurations, and voltage- and current-controlled stimulation on pathway activation and selectivity in Patient 1. First, we showed that the difference in the stimulus amplitude to activate the SP/HD/CbTT pathways compared to the stimulus amplitude to activate the IC pathway, known as the therapeutic window, increased as the pulse width decreased (Figure 4.7). These results match previously reported clinical results suggesting that short pulse widths widen the threshold amplitude between rigidity control and muscle contractions [Rizzone et al., 2001; Reich et al., 2015]. Second, stimulation with the therapeutic electrode contact activated the SP, HD, and CbTT pathways (Figure 4.4). Theoretical translation of the active monopolar electrode contact was able to change the recruitment profile. For example, activation of the LF could be increased in Patient 1 by shifting the active monopolar electrode dorsally from contact 2 to contact 3 (Figure 4.8). And activation of the CbTT pathway could be increased in Patient 1 by shifting the contact 2 posteriorly by 0.5 mm (Figure 4.5). Third, compared to voltage-controlled stimulation, current-controlled stimulation was able to keep consistent the pathway activation of, for example, the CbTT pathway as the encapsulation layer conductivity changed reflecting a change in electrode impedance. The patient-specific FC PAMs suggest that selectivity of individual pathways is not

likely given the close proximity of multiple pathways, but certain stimulation paradigms can activate specific groups of pathways.

4.4.3. Study limitations

The patient-specific FC PAM represents an anatomically and biophysically detailed model of DBS, but as with any model limitations exist with the methods presented. Electrode misalignment resulting from image registration errors and errors in the placement of the model DBS lead represents a source of error in the model predictions. We explored the sensitivity of our predictions to errors in electrode localization by varying the position of the electrode by 0.5 mm in six orthogonal directions (Figure 4.5). The results show that pathway activation can change by greater than 10%, suggesting that further work is necessary to improve potential errors in electrode localization.

Subcortical nuclei of the basal ganglia were segmented to create constraints for the DWI-based tractography. We attempted to reduce error in nuclei segmentation by acquiring 7T MRI data for each patient, which allow for higher resolution and signal-to-noise than conventional 1.5T or 3T images [Duchin et al., 2012]. However, these images are not without error as manual nuclei segmentation of the substantia nigra, red nucleus, and subthalamic nucleus were performed in the coronal 7T T2W or 7T SW image and then transformed to 1.5T T1W image space. As a result of this transformation, the borders of the nuclei are less clearly defined because of interpolation during the

transformation process. Furthermore, there was not adequate contrast of the thalamus on any 7T image so an atlas thalamus had to be fit to these patients.

DWI-based tractography provides a technique to predict axonal pathway trajectories and has revolutionized connectional neuroanatomy in the human brain [e.g. Horn and Blankenburg, 2016; Glasser et al., 2016]. In turn, it is only logical that tractography is now playing a major role in DBS research, and connectomic-based analyses of subthalamic DBS are beginning to become available [e.g. Vanegas-Arroyave et al., 2016; Horn et al., 2017]. However, it remains unclear how consistent the grey matter anatomy and axonal trajectory anatomy is across PD patients, or if tractography alone is capable of accurately reconstructing subthalamic pathways of interest for DBS analysis [Lenglet et al., 2012; Thomas et al., 2014]. These anatomical details become especially important when attempting to characterize the signaling response of axonal pathways to DBS because the axonal trajectory is a key determinate of the membrane polarization from the applied electric field [McNeal, 1976; Gunalan et al., 2017].

For a given axon diameter, the multi-compartment cable axon model is capable of reproducing excitation characteristics that match experimental measurements [McIntyre et al., 2002]. However, each pathway within the brain is comprised of axons that have a distribution of diameters [Mathai et al., 2013; Firmin et al., 2014] and most analyses to date model all axons within a pathway as a single diameter. As the choice of axon diameter has a large impact on the pathway activation predictions (Figure 4.6) [McNeal 1976; Zitella et al., 2015],

future models need to account for the realistic distribution of diameters within each pathway to accurately predict activation.

4.5. Conclusions

We developed detailed patient-specific computational models to calculate the neuronal pathways directly activated by subthalamic DBS. The stimulation likely activates multiple pathways indiscriminately. The results presented provide a biophysical foundation for interpreting the wide-ranging clinical electrophysiology and functional imaging studies exploring the brain network activity generated by subthalamic DBS. However, the models also highlight the desire to be more specific and detailed in the stimulation predictions carries with it the caveats of scientific gaps in anatomical knowledge and image registration limitations.

Chapter 5 - Biophysical properties of the hyperdirect pathway necessary to match clinical cortical evoked potentials from subthalamic deep brain stimulation

Abstract

Deep brain stimulation (DBS) of the subthalamic region is an established clinical therapy for the treatment of Parkinson's disease (PD). Direct stimulation of the hyperdirect pathway, which consists of a special subset of corticofugal axons originating from layer V pyramidal neurons that send an axon collateral to the subthalamic nucleus (STN), has been extensively linked to therapeutic benefit in experimental studies of PD. One experimental measurement used to evaluate hyperdirect activation is the recording of cortical evoked potentials generated by subthalamic DBS. In humans, these evoked potentials have a very fast component (R1) that occurs ~1 ms after the stimulus pulse, as well as a slower component (R2) that reaches its peak in ~6 ms. R1 is typically assumed to arise from antidromic invasion of the hyperdirect layer V pyramidal neurons, while R2 is assumed to arise from intracortical synaptic activity. To address these assumptions, we used a detailed patient-specific DBS model of hyperdirect pathway activation. We reconstructed the hyperdirect pathway using tractography derived from diffusion-weighted images of a PD patient implanted with a subthalamic DBS system. Each of the 1000 tractography-generated streamlines were then modeled as a multi-compartment cable structure. The voltage distribution generated by the DBS electrode was calculated and used to stimulate the model axons. The model system allowed us to evaluate conduction

times from activation of the hyperdirect axons in the STN to arrival of the action potentials in cortex. We compared the conduction times for small (5.7 μm), medium (10.0 μm), and large (15.0 μm) diameter corticofugal axons. Only the 15.0 μm models could generate action potentials in cortex at ~1 ms, coinciding with clinical measurements for R1, but histological measurements suggest that axons of that size are extremely rare in the internal capsule. Given the expected diameter distribution of the hyperdirect pathway, R1 and R2 may actually represent a combined continuum of antidromic invasion of cortex, where the experimentally recorded waveform is the result of interacting field potentials generated by neurons with small, medium, and large diameter axons.

5.1. Introduction

Subthalamic deep brain stimulation (DBS) is an established treatment for the motor symptoms of Parkinson's disease (PD) [Limousin et al., 1998]. While the therapeutic mechanisms of subthalamic DBS remain unresolved, direct activation of the hyperdirect (HD) pathway is thought to play a major role. The HD pathway consists of a subset of corticofugal axons that originate in layer V of cortex, pass through the internal capsule, branch collaterals to the subthalamic nucleus (STN), and terminate in the brainstem/spinal cord [Nambu et al., 2002; Kita and Kita, 2012; Haynes and Haber, 2013]. Electrical and optogenetic stimulation studies in rodents have demonstrated a causal link between HD pathway activation and therapeutic benefit [Li et al., 2007; Gradinaru et al., 2009; Li et al., 2012; Sanders and Jaeger, 2016]. The HD pathway is distinct from the

corticofugal axons that do not branch collaterals to the STN, known as the internal capsule fibers of passage (IC). While stimulation of the HD pathway is believed to improve PD symptoms, stimulation of the IC pathway is believed to cause unwanted side effects such as muscle contractions [Tommasi et al., 2008].

Clinical experiments measuring cortical evoked potentials during subthalamic DBS have identified several different short latency signals [Ashby et al., 2001; Baker et al., 2002; Walker et al., 2012]. Of particular interest, Walker et al. [2012] observed three responses (R1-R3) after each DBS pulse with peak latencies at 1.0 ± 0.4 ms (R1), 5.7 ± 1.1 ms (R2), and 22.2 ± 1.8 ms (R3). They hypothesized that antidromic activation of the HD pathway was the cause of the cortical evoked potential measured at ~1 ms. Therefore, we attempted to verify this hypothesis using a detailed patient-specific computational model of subthalamic DBS. We stimulated the HD and IC pathways in the subthalamic region and measured the timings of action potentials arriving in cortex along these pathways. We also explored the role of stimulation parameter settings (monopolar, bipolar, and stimulus amplitude), as well as the influence of axon diameter on the propagation of action potentials to cortex from subthalamic DBS.

5.2. Materials and methods

This study analyzed the theoretical activation of the HD and IC axonal pathways by DBS electrodes implanted in the subthalamic region using an anatomically and biophysically realistic patient-specific model [Gunalan et al., 2017]. Using the 7T magnetic resonance imaging (MRI) datasets acquired prior

to DBS surgery, we constructed a highly detailed field-cable pathway-activation model of DBS. We explicitly represented the stimulus voltage distribution generated by the DBS electrode and then calculated the response of multi-compartment cable models of myelinated axons with anatomically realistic trajectories to the stimulation.

5.2.1. Ethics statement

Collection of all patient data for this study was approved by the University of Minnesota Institutional Review Board (IRB). The patient provided informed written consent prior to participating in the research and the consent procedure was approved by the IRB.

5.2.2. Patient data

The PD patient was implanted with a Medtronic 3389 DBS lead in the left STN that was connected to an Activa SC IPG (Medtronic, Minneapolis, MN). Using standard clinical programming procedures [Volkmann et al., 2002], therapeutic stimulation parameters were selected (contact 2 [-], case [+]; 1.7 V; 60 μs; 130 Hz). The preoperative OFF medication, OFF stimulation motor subscore of the Unified Parkinson's Disease Rating Scale (UPDRS) was 31, and the 4 month post-operative ON medication, ON stimulation UPDRS score was 14. The DBS electrode impedance at contact 2, as measured by the IPG, was 1450 Ω.

5.2.3. Image acquisition and processing

The patient underwent pre-operative scanning on a 7T MRI system (Magnex Scientific, UK) at the University of Minnesota, using T1-weighted (T1W), T2-weighted (T2W), susceptibility-weighted (SW), and diffusion-weighted (DW) imaging. A pre-operative T1W image was also collected on a 1.5T Siemens Magnetom Espree. A post-operative CT image was acquired on a Siemens Biograph64 Sensation approximately 1 month after the DBS surgery.

The 1.5T T1W image was resliced to 0.4 mm isotropic dimensions to match the in-plane resolution of the 7T images. All images were registered to the common space of the resliced 1.5T T1W image. The DW images were corrected for distortions from magnetic field inhomogeneities and eddy currents. Segmentation of the STN, substantia nigra, and red nucleus was performed on the coronal 7T T2W image, and these segmentations were transformed to T1W space. We segmented the globus pallidus internus, globus pallidus externus, and putamen from the axial 7T T2W image in T1W space. As no image provided adequate contrast for segmentation of the thalamus, we fit the Harvard-Oxford atlas thalamus to the 1.5T T1W image.

5.2.4. Field-cable pathway-activation model

5.2.4.1. DBS voltage distribution

The voltage distribution generated by the DBS electrode varies both spatially and temporally in the tissue medium. We created an electrostatic finite element model in COMSOL to solve Laplace's equation. We accounted for the

tissue anisotropy and inhomogeneity by defining the conductivities from the patient's DW images and tissue-type segmentation [Howell and McIntyre, 2016; Howell and McIntyre, 2017; Gunalan et al., 2017]. We defined the encapsulation layer with a 0.5 mm radius around the entire electrode shaft, and defined the conductivity of the encapsulation layer such that the model impedance best matched the clinical impedance at the therapeutic electrode contact. We then calculated the temporal characteristics of the voltage distribution using an equivalent electrical circuit model for voltage-regulated DBS, such that the modeled stimulus waveform matched the waveform of the Medtronic IPG [Lempka et al., In review].

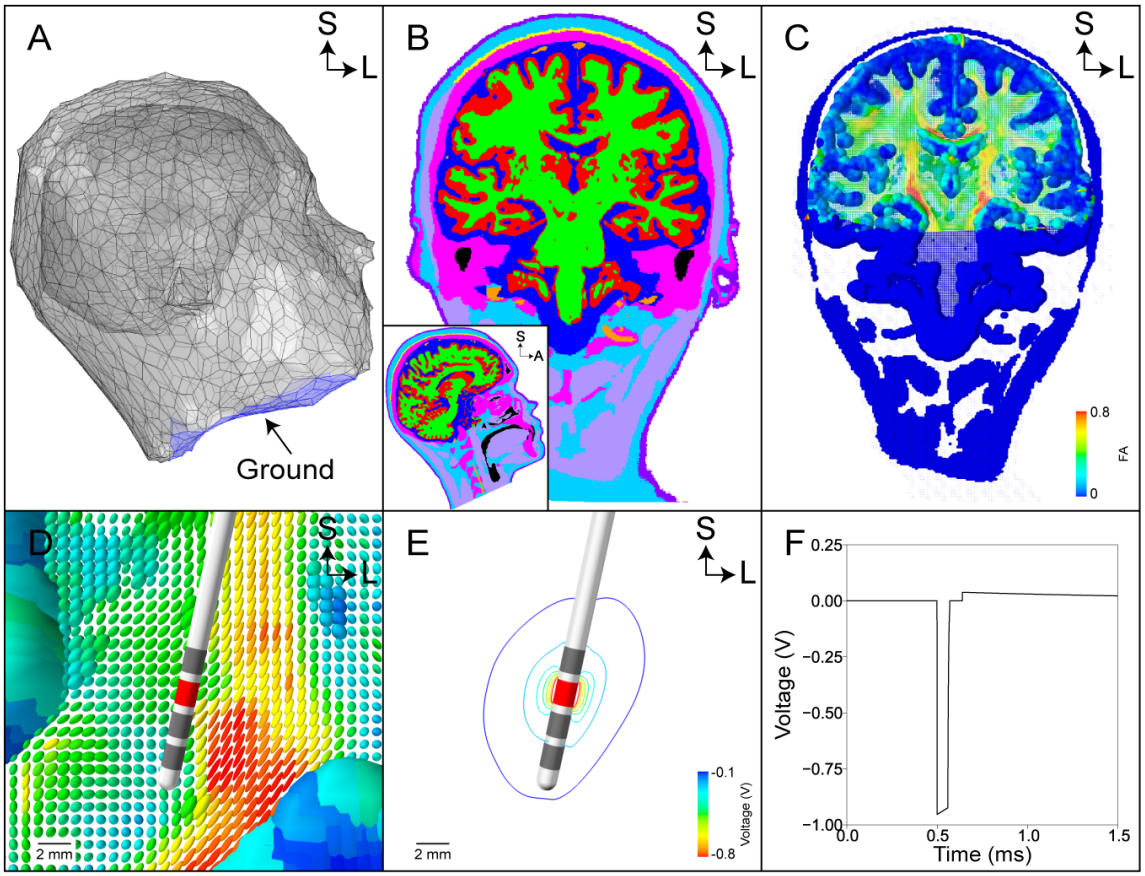

Figure 5.1. Patient-specific deep brain stimulation voltage distribution. (A) Boundaries of the finite element model. Under monopolar configurations, the neck is set to 0 V. (B) Tissue-type segmentation of the head. (C) Conductivity tensors in the head. The tensors are colored according to their fractional anisotropy (FA). (D) Conductivity tensors near the DBS electrode. (E) Isopotential contour lines of the voltage distribution generated by the DBS electrode (contact 2 [-], case [+]; 1 V). (F) Stimulus waveform at the electrode-tissue interface (contact 2 [-], case [+]; 1 V; 60 μs; 130 Hz).

5.2.4.2. Cable model of an axon

We constructed multi-compartment cable models of myelinated axons to represent the axons of the HD and IC pathways (Figure 5.2). We used probabilistic tractography to define the trajectory of the corticofugal axons of the HD and IC pathways. FSL's probabilistic tractography tool (`probtrackx`) generated trajectories, or 'streamlines', which originated in the seed mask of the white matter near the STN and terminated in the cortex and the cerebral

peduncle of the brainstem. We used 64 samples per voxel which was equivalent to 1,000 samples per mm^3. We ignored those streamlines that intersected the DBS lead, STN, red nucleus, globus pallidus, putamen, caudate nucleus, thalamus, temporal cortex, cerebrospinal fluid, or contralateral hemisphere. Of the 9,707 streamlines that were generated with tractography, we randomly sampled 1,000 to represent the IC pathway and 1,000 to represent the corticofugal axon of the HD pathway. We fit a smoothing spline to each tractography-generated streamline to ensure a smooth trajectory for use in the stimulation modeling [Gunalan et al., 2017]. The corticofugal streamlines between the cerebral peduncles and cortex were 89.0 $\pm$ 7.0 mm and 88.8 $\pm$ 6.6 mm in length for the IC and HD pathways, respectively.

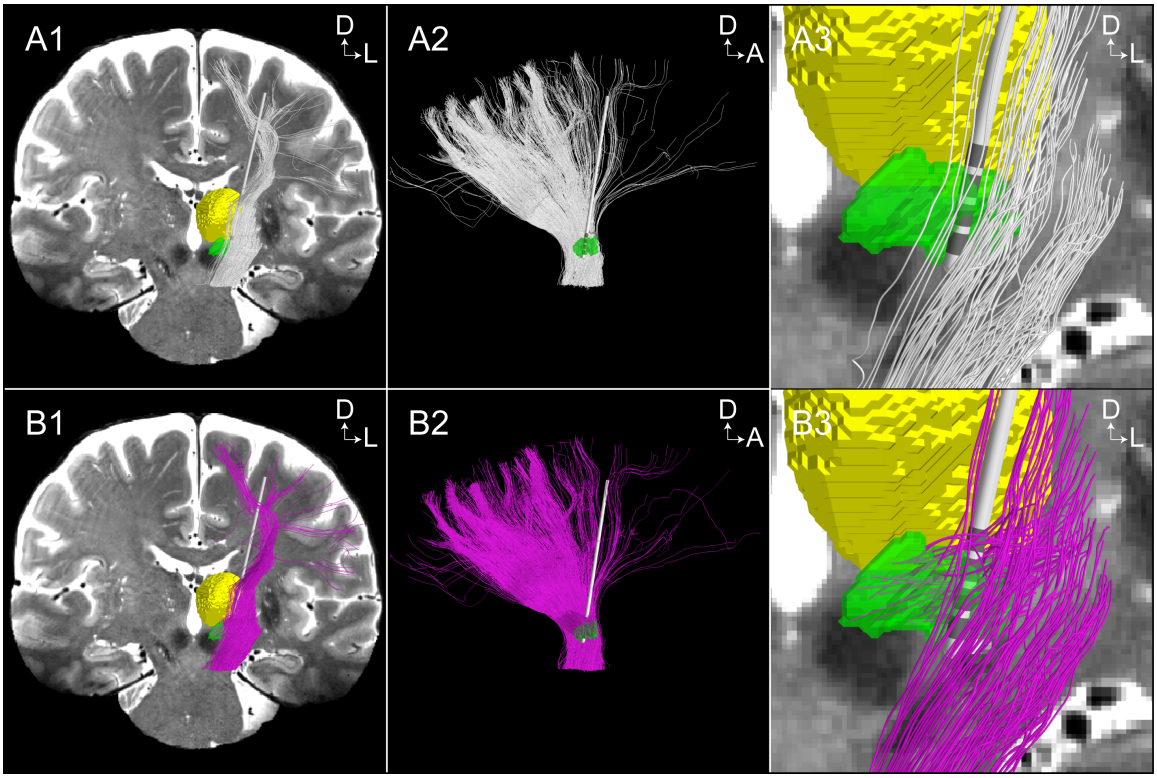

Figure 5.2. Patient-specific model of the internal capsule (IC) and hyperdirect (HD) pathways. (A1/B1) Coronal and (A2/B2) sagittal views show the tractography-generated corticofugal streamlines of the IC and HD pathways. The HD axons have a collateral that branches off of the corticofugal axon and terminates in the subthalamic nucleus. (A3/B3) Zoomed coronal view of the subthalamic region. Subthalamic nucleus – green, thalamus – yellow.

For the HD axons, we modeled a collateral at a randomly chosen node of Ranvier along the corticofugal axon that was within 3 mm in the dorsal-ventral direction from the dorsal boundary of the STN (Figure 5.2). A random voxel within the STN was selected as the termination point of the collateral. We then generated an arc connecting the branch point node of Ranvier and the termination point within the STN to define the collateral trajectory. If the collateral passed through the DBS electrode, we randomly selected a different voxel within the STN and recalculated the corresponding arc.

The geometric and electrical parameters of the cable axon models were defined from previously established models [McIntyre et al., 2002; Howell and McIntyre, 2016]. The myelinated axon was modeled with a double cable structure and the nodes of Ranvier contained voltage-gated fast Na^+, persistent Na^+, and slow K^+ ion channel conductances, and leakage conductance and membrane capacitance properties. The hyperdirect axon collateral that projected into the STN had a diameter that was defined as a fraction of the corticofugal axon diameter (1/3.1) [Hongo et al., 1987; Struijk et al., 1992; Grill et al., 2008]. The response of each individual axon model to the spatially- and temporally-varying DBS voltage distribution was calculated with NEURON (Figure 5.3) [Hines and Carnevale, 2001]. We stimulated each axon with a single DBS pulse and an axon was defined as active if an action potential reached cortex.

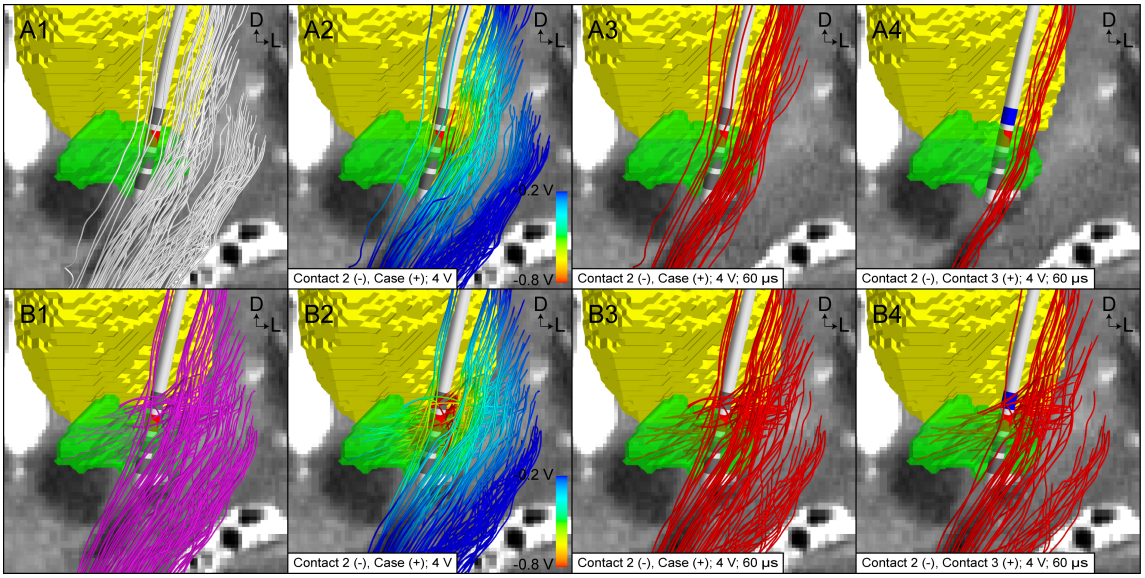

Figure 5.3. Deep brain stimulation of the internal capsule (IC) and hyperdirect (HD) pathways. (A1/B1) One hundred representative axons of each pathway. (A2/B2) The voltage distribution generated by the DBS electrode under a monopolar configuration is used to stimulate the cable axon models. (A3/B3) Those axons that generate a propagating action potential, in response to monopolar stimulation, that reaches cortex are classified as active (red). (A4/B4) Those axons that generate a propagating action potential in response to bipolar stimulation.

5.3. Results

We modeled each tractography-generated streamline as a multi-compartment cable axon structure. We modeled all of the axons within a pathway with a diameter (D) of either 5.7 µm, 10.0 µm, or 15.0 µm. We stimulated these axons with either monopolar or bipolar electrode configurations (Figure 5.3). As expected, we found that as the axon diameter of the pathway increased more axons were activated for a fixed stimulation setting.

We calculated the times for action potential propagation to cortex along the IC and HD pathways in response to subthalamic DBS (Figure 5.4 and Table 5.1). For the HD pathway, the action potentials arrived in cortex with a bimodal distribution due to the site of action potential initiation. If the action potential

initiated in the corticofugal section of a HD axon it typically arrived in the cortex earlier (Figure 5.4B1-B3, red) than if the action potential initiated in the STN collateral (Figure 5.4B1-B3, green). A small percentage of the HD axons initiated action potentials at the node of Ranvier where the collateral branched from the corticofugal axon (Figure 5.4B1-B3, blue).

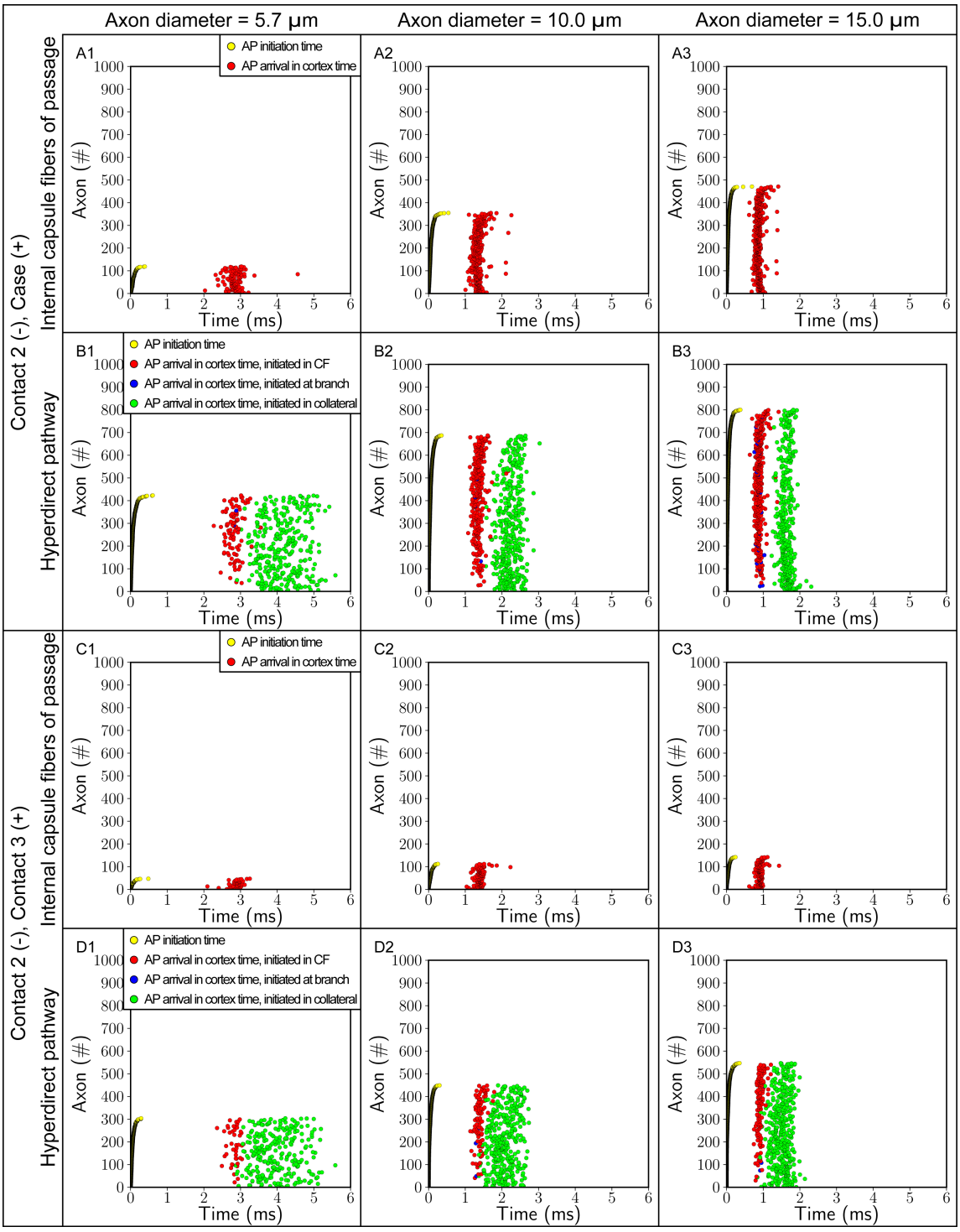

Figure 5.4. Timings of action potentials arriving in cortex after subthalamic deep brain stimulation of the internal capsule (IC) and hyperdirect (HD) pathways. The diameter of the corticofugal axon is represented as either 5.7 µm, 10.0 µm, or 15.0 µm. For each HD axon, the collateral diameter is a fraction of the corticofugal axon diameter (1/3.1). (A/B) Monopolar (contact 2 [-]; case [+]) and (C/D) bipolar (contact 2 [-]; contact 3 [+]) stimulation was modeled with the following settings: 4.0 V; 60 µs. AP – action potential.

Table 5.1. Action potential arrival time in cortex after subthalamic deep brain stimulation of the internal capsule (IC) and hyperdirect (HD) pathways. Time (ms) is calculated from the stimulus onset. Stimulation setting: monopolar (contact 2 [-], case [+]) or bipolar (contact 2 [-], contact 3 [+]); 4.0 V; 60 μs.

Axon diameter (μm)	IC axons		HD axons activated along corticofugal axon or branch node		HD axons activated along axon collateral	
	Monopolar	Bipolar	Monopolar	Bipolar	Monopolar	Bipolar
5.7	2.8 ± 0.2	2.9 ± 0.2	2.8 ± 0.2	2.8 ± 0.2	4.1 ± 0.5	4.0 ± 0.6
10.0	1.4 ± 0.1	1.4 ± 0.1	1.4 ± 0.1	1.4 ± 0.1	2.2 ± 0.2	2.1 ± 0.3
15.0	0.9 ± 0.1	0.9 ± 0.1	0.9 ± 0.1	0.9 ± 0.1	1.6 ± 0.1	1.5 ± 0.2

Once the action potential arrives in cortex it is likely to cause a depolarization of the soma resulting in a measuring electrical signal on the surface of the scalp [Anderson et al., In preparation]. We aligned the model somatic action potentials to the cortical evoked potentials measured clinically by Walker et al. [2012]. In order to do so, we shifted a somatic action potential by the time delay for the action potential to arrive in cortex (Table 5.1). Activation of the 15.0 μm corticofugal axons of the HD and IC pathways resulted in a somatic action potential with a peak at 1.955 ms which was significantly different than the average R1 peak at 1.0 ms for the five patients (six brain hemispheres) reported by Walker et al. [2012] (99% confidence interval [1.947 ms, 1.963 ms]). Activation of the 5.7 μm HD axons along the axon collateral resulted in a somatic action potential with a peak at 5.055 ms which was significantly different than the average R2 peak of 5.7 ms (99% confidence interval [5.006 ms, 5.104 ms]). Interestingly, we aligned these model somatic action potentials to the cortical evoked potentials from one patient reported by Walker et al. [2012] (Figure 5.5). For this patient, the 5.7 μm HD model somatic action potential qualitatively aligned to the R2 peak. However, statistical analyses could not be performed for

this case as the time of the R2 peak was not defined. This data suggests that HD axons with a corticofugal axon diameter equal to or smaller than 5.7 μm might result in the R2 peak.

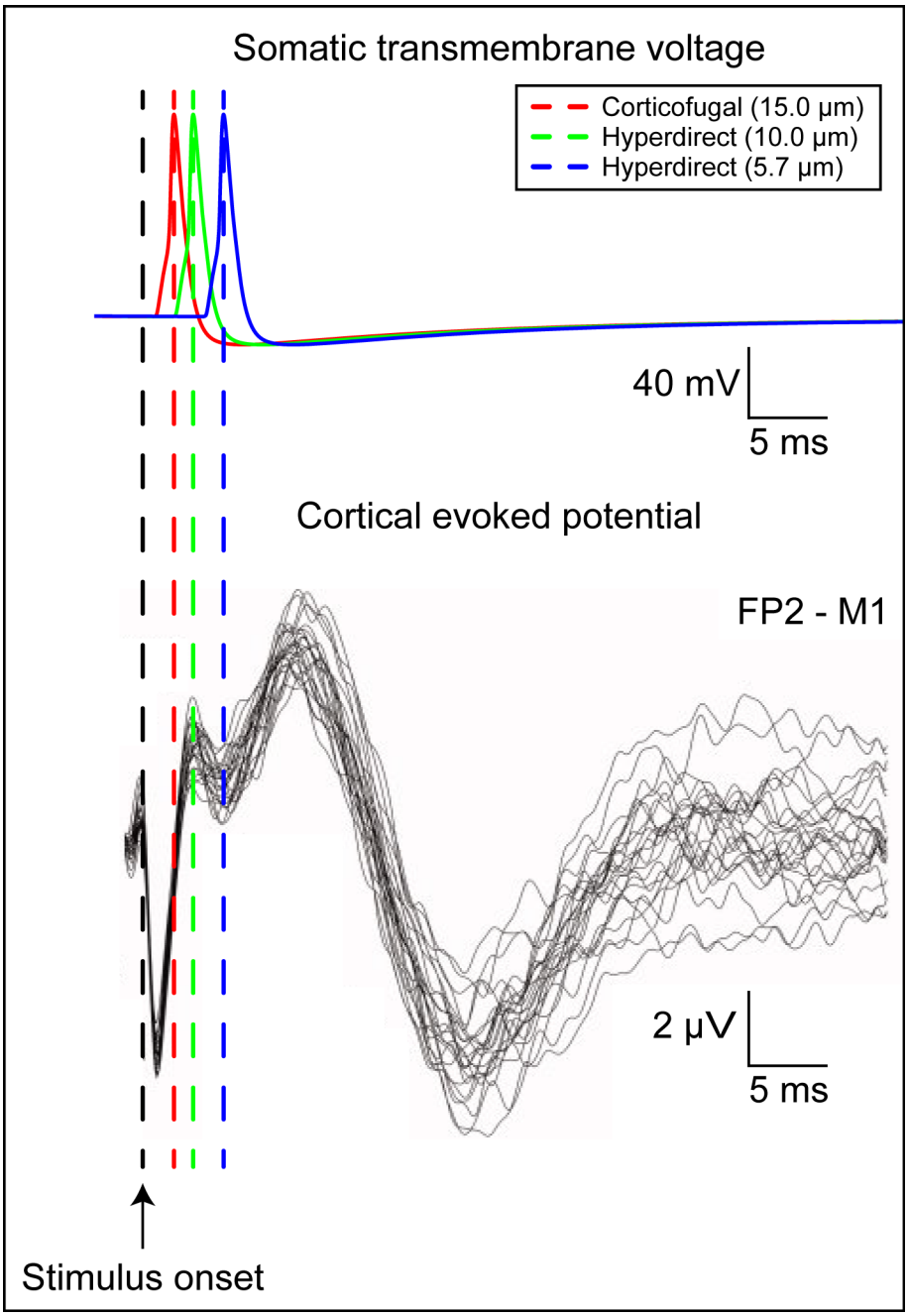

Figure 5.5. Somatic action potentials aligned to the cortical evoked potentials (black lines) from one patient measured by Walker et al. [2012]. Stimulation occurs in the subthalamic nucleus. The somatic action potentials are shifted in time according to the corresponding mean action potential arrival time in cortex (Table 5.1).

We calculated the action potential propagation speed from the node of action potential initiation in the subthalamic region to the cortex for the IC and HD axons (Table 5.2). The propagation speed was calculated separately for those HD axons that initiated an action potential in the corticofugal axon and those HD axons that initiated an action potential in the collateral. Propagation speed was similar for monopolar and bipolar stimulation; however, axon diameter substantially effected the conduction speed. If action potential initiation in the HD axon occurred in the STN collateral, as opposed to the corticofugal axon, the propagation speed to cortex was slower.

Table 5.2. Action potential propagation speed after subthalamic deep brain stimulation of the internal capsule (IC) and hyperdirect (HD) pathways. Propagation speed (m/s) is calculated from the site of action potential initiation to cortex. Stimulation setting: monopolar (contact 2 [-], case [+]) or bipolar (contact 2 [-], contact 3 [+]); 4.0 V; 60 μs.

Axon diameter (μm)	IC axons		HD axons activated along corticofugal axon or branch node		HD axons activated along axon collateral	
	Monopolar	Bipolar	Monopolar	Bipolar	Monopolar	Bipolar
5.7	25.8 ± 0.3	25.7 ± 0.6	25.7 ± 0.2	25.6 ± 0.5	18.7 ± 1.9	19.4 ± 2.1
10.0	54.2 ± 1.3	53.5 ± 1.9	53.9 ± 1.2	53.1 ± 1.7	34.6 ± 3.4	37.0 ± 4.7
15.0	83.3 ± 3.1	82.6 ± 3.6	82.9 ± 3.0	82.4 ± 3.7	46.9 ± 4.0	51.1 ± 7.0

We explored the sensitivity of the results to the stimulation amplitude (Figure 5.6). We found that as the stimulation amplitude increased, as expected more axons were activated, but that the general timing of action potentials arriving in cortex did not vary. Additionally, at all stimulus amplitudes (1 V - 4 V) the IC pathway was activated resulting in short latency action potentials in cortex.

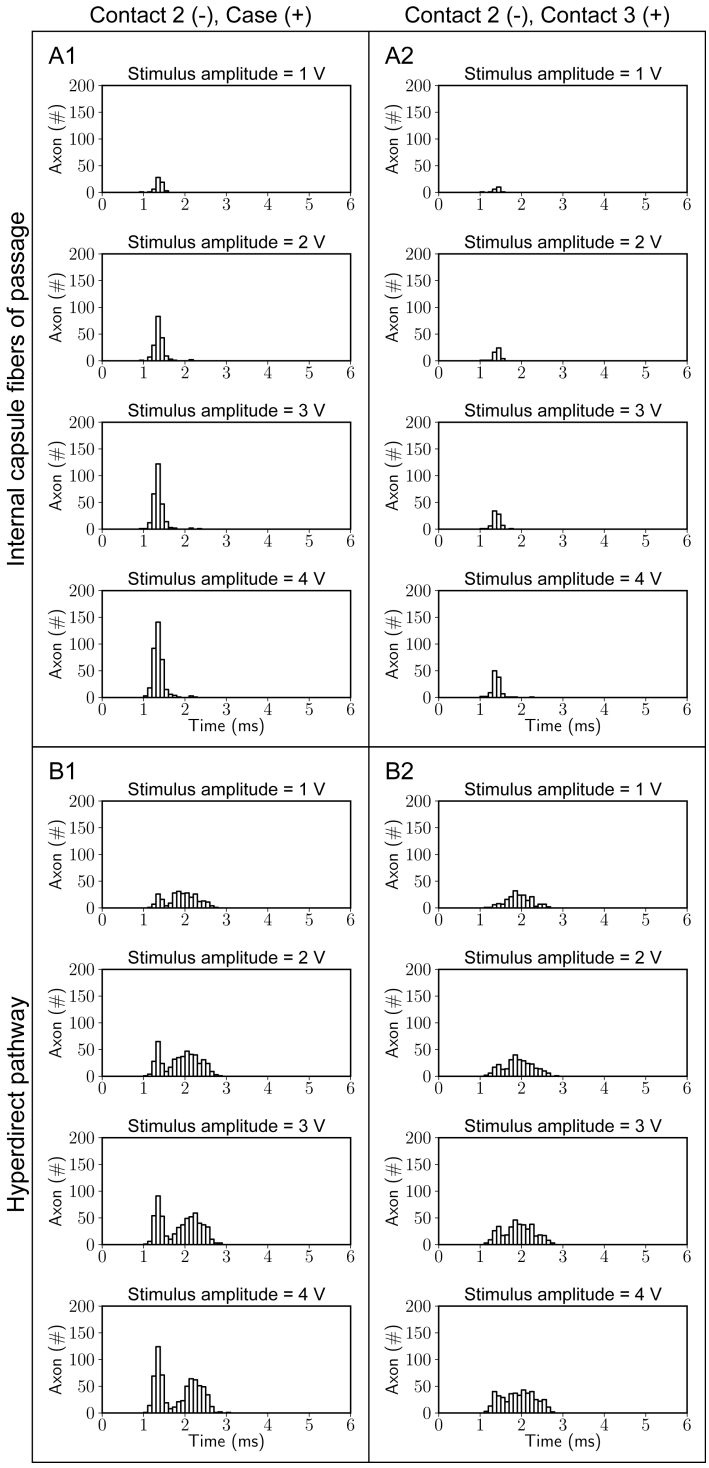

Figure 5.6. Timings of action potentials arriving in cortex for a range of stimulation amplitudes (1 V – 4 V). Histogram plots are generated for the (A) internal capsule and (B) hyperdirect pathways, in response to monopolar (contact 2 [-], case [+]) and bipolar (contact 2 [-], contact 3 [+]) electrode configurations. Stimulus pulse width = 60 μs.

5.4. Discussion

Short latency cortical evoked potentials arising from subthalamic DBS represent clinical measurements that can help dissect the underlying neural response to therapeutic stimulation. Recent advances in recording amplifiers, signal processing strategies, and experimental design have enabled experimental identification of DBS-induced cortical responses with latencies as short as ~1 ms, with additional peaks at approximately ~6 ms and ~22 ms [Walker et al., 2012]. The 1 ms and 6 ms latency signals are expected to result from antidromic activation of cortical pyramidal neurons and we set out to evaluate the plausibility of that hypothesis using a detailed biophysical model of human subthalamic DBS. Our results suggest that the 1 ms peak is unlikely to be generated by direct activation of hyperdirect axon collaterals in the STN, but could possibly be the result of directly activating corticofugal axons in the internal capsule. However, such a fast response requires axonal conduction velocities, and underlying axon diameters, that are extreme for the internal capsule. In addition, the extra time delay needed to generate a somatic action potential spike and polarization of the apical dendrites casts further doubt on the 1 ms signal being derived specifically from antidromic activation of hyperdirect neurons. Alternatively, our simulation results demonstrate that the 6 ms signal is consistent with the biophysics of hyperdirect axon collateral activation in the STN and propagation to cortex.

Wide-ranging experimental and clinical studies have recently highlighted direct stimulation of the hyperdirect pathway as an important component of

therapeutic subthalamic DBS [Li et al., 2007; Gradinaru et al., 2009; Whitmer et al., 2012; Walker et al., 2012; Li et al., 2012; Sanders and Jaeger, 2016]. As such, we developed a computational model of hyperdirect pathway DBS to explore the effects of stimulation within a controlled environment [Gunalan et al., 2017]. This detailed model allowed us to accurately account for the stimulating electric field, axonal trajectories of the internal capsule, and biophysics of action potential initiation and propagation (Figure 5.3). We used the model to evaluate the impact of different stimulation conditions (monopolar vs. bipolar), stimulus amplitudes, and axon diameters on the direct activation of action potentials in hyperdirect neurons and internal capsule fibers of passage. We then calculated the conduction times for those action potentials to reach cortex (Figure 5.4) and attempted to reconcile the simulation results with clinical recordings of cortical evoked potentials generated by subthalamic DBS (Figure 5.5) [Walker et al., 2012].

Walker et al. [2012] observed that subthalamic DBS activated cortex at ~1 ms, ~6 ms, and ~22 ms after each DBS pulse, referred to as R1, R2, and R3, respectively. They subsequently concluded that clinically effective subthalamic DBS in humans with PD activates the cerebral cortex with short latency, most likely by antidromic activation. In general, our model results support the conclusions of Walker et al. [2012] and provide quantitative estimates for the underlying neural activation responsible for their experimentally recorded signals. However, we found that simulating the 1 ms latency to cortex required model parameters (15 μm diameter axons) that are somewhat unlikely given currently

available data on the axon diameters and conduction velocities of the pyramidal tract [Edgley et al., 1997; Firmin et al., 2014]. Nonetheless, electrophysiological recordings are known to demonstrate a strong sampling bias for the most excitable and fastest conducting neurons, which would be consistent with the largest possible axons contained with the internal capsule [Humphery and Corrie, 1978; Firmin et al., 2014]. In addition, axon diameter information specifically derived from the human internal capsule is relatively limited [e.g. Graf von Keyserlingk and Schramm, 1984] and may very well consist of more large diameter fibers than seen in lower primates.

The 6 ms signal (R2) can be more easily reconciled with direct activation of hyperdirect axon collaterals in the STN. Given a corticofugal axon diameter (5.7 μm), and resulting conduction velocity (25 m/s), more in line with electron microscopy results from the internal capsule [Firmin et al., 2014], we found an average cortical arrival time of 4.0 ms for an action potential initiated in the hyperdirect axon collateral within the STN (Figure 5.4, Table 5.1). This timing, coupled with the ~1 ms necessary for the antidromic action potential to invade the cell body and propagate up to the apical dendrites [Popovic et al., 2011] (Figure 5.5), thereby creating the dipole important for evoked potential detection [Einevoll et al., 2013], should occur at ~4-6 ms. The model also predicts substantial variability in the cortical arrival times of action potentials initiated in hyperdirect axon collaterals (Figure 5.4). This variability arises from the conduction time along the axon collateral in the STN and the different corticofugal axon trajectories lengths, which are amplified by the slower

conduction velocity of 5.7 μm diameter axons. The spread in cortical arrival times would limit the magnitude of the summated cortical dipole, so it is to be expected that R2 would be smaller than R1, as observed experimentally.

While this study used the most advanced computational model of subthalamic DBS currently available to quantify axonal activation and propagation, the results remain idealized simulations subject to caveats and limitations [Gunalan et al., 2017]. For example, individual components of the model can be validated and constrained against experimental measurements, such as the axon model [McIntyre et al., 2002] or volume conductor model [Miocinovic et al., 2009], but the generalized output predictions of pathway activation cannot be directly measured with current experimental techniques. Therein lies a key motivation for this study, attempting to evaluate the congruence of the model predictions with established experimental recordings. However, in that process our theoretical analysis highlighted a number of important variables such as the role of axon diameter and the difference between stimulating HD axon collaterals or corticofugal axons in dictating the timing of cortical evoked potentials. Therefore, future DBS evoked potential studies would likely benefit from a coupled model-experiment analysis strategy to help constrain the models as well as improve interpretability of the recorded signals.

5.5. Conclusions

In conclusion, our theoretical analysis of antidromic action potential propagation to cortex from subthalamic DBS suggests that short latency

responses in cortex are the result of directly activating extremely large diameter (~15 μm) internal capsule fibers of passage, while the 6 ms signal is the result of directly activating moderately sized hyperdirect axon collaterals in the STN.

Chapter 6 – Discussion and conclusions

6.1. Summary of work presented

Deep brain stimulation (DBS) is an established therapy for treating the movement symptoms of Parkinson's disease (PD), but the axonal pathways that mediate the therapeutic effects of DBS are not clearly defined. DBS computational models are currently the only non-invasive method for predicting the direct effects of stimulation on a patient-specific basis. The goal of this work was to evaluate and utilize patient-specific DBS models to provide insights on the effects of stimulation. Throughout this study, we used these DBS models to characterize activation of the subthalamopallidal (SP), lenticular fasciculus (LF), hyperdirect (HD), internal capsule fibers of passage (IC), cerebellothalamic tract (CbTT), and medial lemniscus (ML) pathways.

In Chapter 3, we compared the differences in axonal activation predictions between detailed patient-specific DBS models described in Chapter 2 (i.e. FC PAM) and simplified DBS models (volume of tissue activated [VTA] and driving force [DF]). Our goal was to evaluate the accuracy of DF and VTA models compared to FC PAMs for relevant DBS parameters. We calculated the errors of the four predictors (DF-Peterson, VTA-Chaturvedi, VTA-Madler, VTA-Astrom) for a range of axon diameters (2 μm - 10 μm), stimulus pulse amplitudes (0.1 V- 10 V), stimulus pulse widths (30 μs - 120 μs), and electrode configurations (monopolar, bipolar, tripolar, quadripolar). We defined the criteria for accuracy as a maximum absolute error of 5% in pathway activation, as clinical effects are typically noted at pathway activation levels beginning at ~10% [Chaturvedi et al.,

2010; Gunalan et al., 2017]. We found that all DF-based and VTA-based predictors have errors in stimulation thresholds, and as a result errors in pathway activation. The errors in pathway activation for all predictors were larger than 5% for the majority of the parameter space tested. As all predictors did not meet this error tolerance technical specification, we elected to use the FC PAM for subsequent analyses.

In Chapter 4, we calculated the pathways activated by therapeutic subthalamic DBS in three PD patients using detailed patient-specific FC PAMs and performed sensitivity analyses to determine the strength of the predictions. We hypothesized that therapeutic stimulation (contact 2 [-], case [+]; 1-5 Volts; 60 μs; 130 Hz) in the subthalamic region selectively activates the HD and SP pathways, over the LF, CbTT, IC, and ML pathways. First, we found that therapeutic stimulation activates multiple pathways and these pathways were not consistent among the three PD patients. For instance, in Patient 1, the HD was activated at a higher percentage than the SP and CbTT pathways, but in Patient 3, the LF was activated at a higher percentage than the HD and SP pathways. Second, we performed a parameter sensitivity analysis to understand the influence of electrode localization errors and axon diameter choice on the activation predictions in Patient 1. We found that these parameters can have a substantial impact on the results, but the HD and SP were consistently activated for the entire parameter space. Third, we explored alternative electrode configurations, stimulus pulse amplitudes, and stimulus pulse widths in Patient 1. We found that selective activation of a single pathway is not possible with the

current electrode location in the dorsal subthalamic nucleus as multiple pathways converge in this region. This data emphasizes the importance of constructing patient-specific models as the activation characteristics are variable among patients even though the electrode location is consistently placed within the dorsal subthalamic nucleus. Additionally, the current scientific gaps in the axon diameter distribution of these 6 pathways need to be addressed to further constrain these model predictions.

In Chapter 5, we used an FC PAM to dissect the axons mediating short latency cortical evoked potentials during subthalamic DBS. We hypothesized that short latency responses at 1.0 ms in cortex are due to activation of hyperdirect axons and addressed this hypothesis by constructing a patient-specific FC PAM of the IC and HD pathways. We stimulated in the subthalamic region and quantified the timings of action potentials arriving in cortex along these two pathways. Action potentials arrived in cortex at dispersed timings that were dependent upon the axon diameter and trajectory. Activation of corticofugal axons of large diameter (15.0 μm) IC and HD axons resulted in action potentials that invaded the soma of the pyramidal neuron in cortex on average 1.955 ms after the stimulus pulse. The average timing of this cortical invasion is significantly slower than the R1 component of the cortical evoked potential. Interestingly, activation of medium diameter (5.7 μm) HD axons in the axon collateral generated somatic action potentials whose peak qualitatively coincided with the R2 component of the cortical evoked potential of one patient measured by Walker et al. [2012]. Biophysical models of DBS that explicitly represent

action potential conduction along patient-specific axonal trajectories can be coupled with experimental measurements of evoked potentials to provide insights of the neurons mediating the measured responses.

Through this work we have advanced the infrastructure for FC PAMs while providing insights on the developments necessary for the next generation of patient-specific DBS models. Here, we lay the foundation for future prospective studies aimed at targeting stimulation to specific pathway(s) and measuring the clinical response, to provide insights on the pathways mediating the therapeutic effects of DBS.

6.2. Current state of DBS modeling

Computational modeling of DBS has grown in popularity over the past 15-20 years in both academia and industry. From a research perspective, DBS modeling provides insights of brain activity that are currently not available with other imaging modalities in humans. For example, intense scientific interest surrounds identification of the axonal pathways directly activated by DBS and how those pathways are connected within the overall brain circuitry. From a clinical perspective, there is a need to simplify the customization of the stimulation parameter settings to individual patients, known as programming the DBS device, and DBS modeling software for that purpose are now commercially available. However, there exists a wide range of different DBS modeling approaches designed for research and/or clinical applications.

Experimental evidence suggests that extracellular electrical stimulation technologies, such as DBS, generate action potentials in nearby neurons [Ranck, 1975; Nowak and Bullier, 1998; Hashimoto et al., 2003]. Thus, many of the currently available DBS models are focused on calculating the neurons (and their axons) that are directly activated by stimulation. As technology has advanced over the years there has been an evolution of these patient-specific DBS models (Figure 6.1). First generation models calculated the position of the DBS electrode in the context of the patient's MRI and subcortical nuclei. Second generation models calculated the position of VTAs relative to the subcortical nuclei [Frankemolle et al., 2010; Butson et al., 2011]. Third generation models, known as activation volume tractography (AVT), generated tractography-based streamlines from the VTAs to calculate the structural connectivity from the stimulation site to all brain regions [Vanegas-Arroyave et al., 2016; Horn et al., 2017]. Fourth generation models calculated the distance between axonal pathways defined with strict anatomical constraints and the DBS electrode [Coenen et al., 2011]. Fifth generation models, known as a VTA PAM, calculated the overlap of a VTA with the axonal pathways defined with strict anatomical constraints [Madler and Coenen, 2012]. Sixth generation models, known as a FC PAM, calculated the axonal pathways (defined with strict anatomical constraints) directly activated by stimulation using biophysical axon models [Miocinovic et al., 2006; Chaturvedi et al., 2010]. With each generation, the models have become more anatomically and biophysically detailed, with an expectation of greater accuracy.

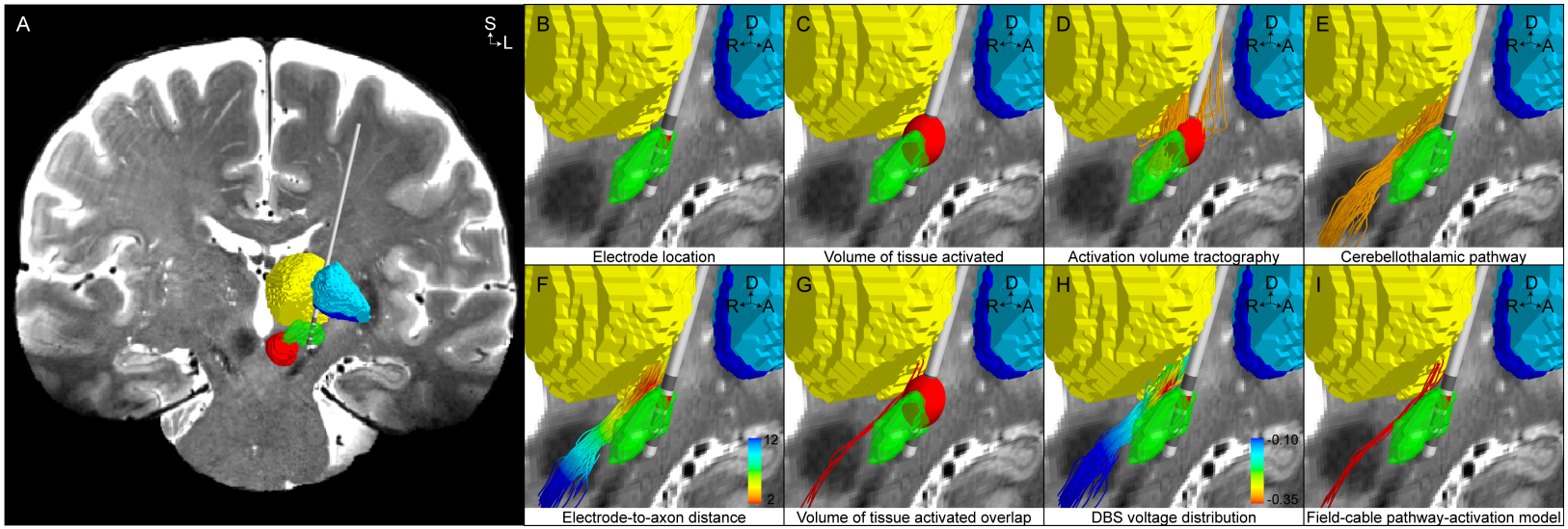

Figure 6.1. An evolution of computational models of deep brain stimulation. An example is provided in the context of the cerebellothalamic pathway. (A) Coronal view of a T2-weighted magnetic resonance image, deep brain stimulation (DBS) lead, and subcortical nuclei (thalamus – yellow, globus pallidus externus – light blue, globus pallidus internus – dark blue, subthalamic nucleus – green, red nucleus – red). (B) Electrode position relative to subcortical nuclei. (C) Volume of tissue activated (VTA, red). (D) Activation volume tractography. The voxels within the VTA are used as seeds for tractography. (E) Diffusion-weighted imaging-based tractography of the cerebellothalamic pathway. (F) Distance from contact 2 to the cerebellothalamic pathway. (G) Cerebellothalamic streamlines intersecting the VTA. (H) Patient-specific DBS voltage distribution interpolated along the cerebellothalamic pathway. (I) The DBS voltage distribution is used to stimulate multi-compartment cable axon models and those that generate action potentials are classified as active (red). Parameters: axon diameter = 5.7 μm; stimulus pulse amplitude = 1.7 V; stimulus pulse width = 60 μs; stimulus pulse frequency = 130 Hz.

Academic software packages (e.g. Cicerone, Lead-DBS, DBSproc, StimVision) [Miocinovic et al., 2007; Horn and Kuhn, 2015; Lauro et al., 2016; Noecker et al., 2017] and commercial software packages (e.g. Medtronic's SureTune3, Boston Scientific's GUIDE, and Brainlab's Elements) are becoming widely available that create a single platform for creation and analysis of patient-specific DBS models. These platforms simplify the DBS model construction by automating many steps and eliminating the necessity to move data between different software packages. Widely used platforms also have the advantage of keeping methodologies consistent between different research studies and patient cohorts. These platforms typically implement DBS models such as AVT and/or VTA PAM. Alternatively, several groups have developed custom workflows to implement DBS models that allow for more advanced methodologies (i.e. FC PAM) [Miocinovic et al., 2006; Zitella et al., 2013].

Clinical DBS research studies using models are typically focused on developing correlations between outcomes (e.g. UPDRS-III scores) and model results (e.g. DBS electrode position or pathway activation) to infer the therapeutic and non-therapeutic regions for stimulation. Coenen et al. [2011] used tractography to target the DBS electrode to the cerebellothalamic pathway for suppression of tremor in a patient. Butson et al. [2011] used VTAs to calculate those regions associated with an improvement in bradykinesia and rigidity. Frankemolle et al. [2010] showed that cognitive side effects can be avoided by targeting stimulation to the dorsal subthalamic nucleus with VTAs. Vanegas-Arroyave et al. [2016] illustrated the difference in AVT connectivity patterns

between therapeutic and non-therapeutic stimulation. Horn et al. [2017] used AVT connectivity to show that DBS outcomes can be predicted given a desired therapeutic connectivity pattern. In this work, we used FC PAMs to illustrate the pathways activated during therapeutic DBS and the strength of these predictions given several sources of error (Chapter 4). These works illustrate a few of the ways that DBS models are being utilized to better understand where to stimulate within the subthalamic region for PD.

Recent studies focused on DBS model development have illustrated the non-negligible differences in predictions that arise solely from the modeling strategy implemented. For instance, in the volume conductor model, the choice of boundary conditions [Walckiers et a., 2010; Golestanirad et al., 2012], or ignoring anisotropy and inhomogeneity of the tissue conductivities [Chaturvedi et al., 2010; Howell and McIntyre 2017], or even using different methods for calculating anisotropic and inhomogeneous tissue conductivities [Howell and McIntyre, 2016], can result in errors in the DBS voltage distribution and subsequently errors in the excitation thresholds of axons. Additionally, the accuracy of the tractography-generated streamlines is highly dependent on the choice of the voxel-wise diffusion model, tractography algorithm, and input parameters [Fillard et al., 2011; Thomas et al., 2014]. In this work, we showed that simplified methods for predicting axonal activation (i.e. VTA PAM or DF PAM) compared to detailed methods (i.e. FC PAM) have non-linear errors in the excitation thresholds and pathway activation (Chapter 3). Thus, there is growing evidence that specific methods have to be implemented in order to generate

physiologically accurate predictions, and standardizing methodologies will minimize the variations in model predictions that arise solely due to the choice of methods implemented.

As more of the model parameters become constrained and platforms for implementing the models become refined, more studies will be able to take advantage of the insights gained from patient-specific DBS models. These studies will also be able to leverage the large investments that are being made in the field of imaging with initiatives such as the Human Connectome Project [Van Essen et al., 2013] to produce even more accurate and detailed DBS models. Thus, the impact of DBS modeling has yet to reach its full potential.

6.3. Limitations of DBS models

Electrical stimulation of excitable tissue is a complex phenomenon [Rattay, 1999; Merrill et al., 2005]. The methods presented herein represent the latest advancement of patient-specific DBS models of axonal activation. However, as with any model, these methods have their own limitations. In developing the next generation of patient-specific DBS models, six general areas need to be considered.

First, image processing steps such as image registration and electrode localization can result in errors in the modeled DBS electrode position. Errors in electrode localization can result in non-negligible errors in predicted pathway activation [Miocinovic et al., 2006; Chapter 4]. These errors can be potentially

minimized by using post-operative 3D rotational fluoroscopy, instead of a post-operative CT scan, for localizing the DBS electrode [Reinacher et al., 2017].

Second, the patient-specific conductivity tensor field within the volume conductor model is defined using isotropic tissue-type conductivities that have a reported range [Gabriel et al., 1996]. The calculated DBS voltage distribution varies as a non-linear function of this range [Howell and McIntyre, 2017]. Non-invasive methods for measuring conductivities *in vivo* might be an alternative method for more accurately defining conductivities in the model [Akhtari et al., 2016]. Additionally, the encapsulation layer properties (i.e. thickness, conductivity, and heterogeneity) cannot be measured on a patient-specific basis. These parameters have a reported range [Grill and Mortimer, 1994] and likely change over time [Cheung et al., 2013; Hartmann et al., 2015]. Changes in the encapsulation layer conductivity can have a non-negligible effect on pathway activation under voltage-controlled stimulation (Chapter 4). However, current-controlled stimulation would likely minimize this issue [Lempka et al., 2010].

Third, validated methodological standards do not currently exist for the creation of tractography-based reconstructions of axonal pathways within the subthalamic region. As the choice of voxel-wise diffusion model, tractography algorithm, and input parameters can affect the streamlines reconstructed, optimization of tractography methodology for the subthalamic region remains unresolved. Alternatively, pathway atlases, defined within the context of a traditional anatomical brain atlas, represent a possible alternative. Such pathway atlases would be defined based on strict constraints in a standard space and

transformed to patient space. Future studies need to validate such approaches with histological tracing studies to determine accurate modeling strategies for axonal reconstructions.

Fourth, the multi-compartment cable axon model is a highly detailed model of a mammalian axon that is capable of reproducing excitation characteristics of experimentally measured axons [McIntyre et al., 2002]. However, this model is parameterized for larger diameter peripheral nerve axons. Future axon models need to be developed that represent the unique electrical and geometrical properties of central nervous system axons. Additionally, the composition of axon diameters within each pathway needs to be constrained with electron microscopy studies in humans.

Fifth, there are several methods for predicting axonal activation (i.e. VTA, VTA PAM, DF PAM, FC PAM, AVT). VTA analyses calculate the regions activated by stimulation. VTAs obviate the need for reconstructing axonal pathways and calculating the neural response to stimulation, by using previously calculated simulations results from idealized conditions with straight axonal trajectories in a homogeneous volume conductor. However, DBS exerts its effects on neurons and their axons that take tortuous trajectories around the electrode in a heterogeneous environment that is dependent upon the patient-specific anatomy. Thus, since our understanding of these pathways has grown in the last 10 years [Gallay et al., 2008; Kita and Kita, 2012; Haynes and Haber, 2013], DBS models need to shift paradigms from calculating the regions activated by stimulation to explicitly calculating the pathways activated.

Furthermore, comparison of predictions from simplified VTA PAMs with detailed FC PAMs have illustrated that such simplified algorithms result in large non-linear errors (Chapter 3). We propose that calculation of the non-linear response of axons to stimulation in FC PAMs can be eliminated by using a DF-based model [Warman et al., 1992; Peterson et al., 2011]. Analysis of a previously developed DF-Peterson PAM suggests that it could calculate the activation of pathways to within ~10% error for many cases tested (Chapter 3). However, the DF-Peterson algorithm was trained using artificial potentials not representative of a DBS macroelectrode. Preliminary analysis of a novel DF algorithm trained with more realistic DBS potentials suggests that prediction accuracy can be improved for a DF-based algorithm [Howell et al., In preparation]. Such a step would expedite the model computation, allowing for exploration of the effects of stimulation with a large range of parameters and large cohort of patients.

Sixth, DBS models ignore the interaction of neighboring neurons. Populations of neurons simultaneously depolarizing in response to stimulation can influence the excitability of nearby neurons by changing the local extracellular electric field [Nelson, 1966; Jefferys, 1995]. Additionally, DBS models largely ignore the influence of axon collaterals and local interneurons that could also change the activity of nearby neurons. Accounting for both of these factors would more closely mimic the *in vivo* environment.

The limitations described above represent potential areas of influence on model predictions. Future studies need to incorporate the proposed details to

construct anatomically and biophysically accurate models of DBS or provide quantitative justification for their exclusion.

6.4. Future directions

Patient-specific DBS models are now capable of making especially detailed predictions at the cellular and network levels. However, the validity of those predictions remains unclear. Individual components of the overall model system can be independently validated via comparison to experimental data. For example, the volume conductor model can be compared to microelectrode recordings of the voltage distribution in the brain [Miocinovic et al., 2009]. In addition, the axon model can be constrained by histological measurements of sodium channel density or voltage clamp measurements of the membrane potential, and compared to electrophysiological measurements of action potential generation [McIntyre et al., 2002]. However, validating the integrated DBS model represents a more challenging proposition, but validation of DBS models is necessary to enhance their scientific credibility and clinical acceptance.

The DBS model output predictions of pathway activation cannot be directly measured with current experimental techniques. However, it is possible to perform indirect measurements that could be used to evaluate model predictions, with electromyography (EMG) measurements corresponding to IC activation being the most easily attainable [Chaturvedi et al., 2010]. Recent clinical interest in using EMG to better characterize activation of the IC during subthalamic DBS [e.g. Mahlknecht et al., 2017; Bally et al., 2017], or cortically evoked electric

potentials from HD antidromic activation [e.g. Walker et al., 2012], represent excellent opportunities for the DBS modeling and clinical communities to converge on analyses that would be mutually beneficial.

Future advances in calcium imaging in nonhuman primates represents an excellent opportunity to directly validate these model predictions [Sadakane et al., 2015]. Current electrode recording technology cannot measure neural activity from the entire downstream region where axons, passing by the DBS electrode, project. However, as described by O'Shea et al. [2017], calcium imaging coupled to post-mortem brain circuit maps obtained with CLARITY [Chung et al., 2013] would provide an unparalleled platform for direct validation of the axonal reconstructions and activation predictions. These cutting edge experimental techniques truly have the potential to advance the field of computational neuroscience.

6.5. Conclusions

The goal of using computational DBS models is to first identify the underlying brain circuitry responsible for disease symptoms, and then second provide tools to accurately predict optimal strategies for targeted stimulation of those specific circuits. Our current understanding suggests that the simplest and most energy efficient method for interfacing with brain circuitry with electrical stimulation is via direct activation of axonal pathways. Therefore, this work focused on detailing the axonal pathways directly stimulated by clinical DBS.

Clinically effective subthalamic DBS likely activates multiple pathways indiscriminately, as we showed that the DBS models predict activation of large diameter corticofugal axons, the hyperdirect pathway, and the subthalamopallidal pathway. We showed that these results are robust to the choice of a few unconstrained parameters, but these results also emphasize the importance of standardizing methodologies between studies to minimize the variability in results due to the choice of parameters alone. This work lays the foundation for the use of computational models coupled with current steering technology and clinical measurements to understand the pathways that mediate specific clinical responses in DBS.

Appendix A – Short pulse width widens the therapeutic window of subthalamic neurostimulation

Reich MM, Steigerwald F, Sawalhe AD, Reese R, Gunalan K, Johannes S, Nickl R, Matthies C, McIntyre CC, Volkmann J. Short pulse width widens the therapeutic window of subthalamic neurostimulation. Annals of clinical and translational neurology. 2015 Apr 1;2(4):427-32.

Summary

We explored the impact of pulse durations <60µs on the therapeutic window of subthalamic neurostimulation in Parkinson's disease. Current thresholds for full rigidity control and first muscle contractions were evaluated at pulse durations between 20 and 120µs during a monopolar review session in 4 patients. The average therapeutic window was 2,16mA at 60µs, which proportionally increased by 182% at 30µs, while decreasing by 46% at 120µs. Measured chronaxies and model data suggest, that pulse durations <60µs lead to a focusing of the neurostimulation effect on smaller diameter axons close to the electrode while avoiding stimulation of distant pyramidal tract fibers.

A.1. Introduction

Deep brain stimulation of the subthalamic nucleus (DBS-STN) is an established surgical treatment for motor fluctuations or dyskinesia in Parkinson's disease (PD)[1-3]. The outcome critically depends on appropriate lead location[4] and setting of stimulation parameters. Inadvertent leakage of current into

adjacent fiber tracts, such as pyramidal fibers lateral to the STN[5], limits the therapeutic window by causing dysarthria or impaired fine motor skills[6]. As a result, much research has been devoted to modelling and visualizing the electrical field of a given electrode position and parameter setting within the individual brain anatomy [7] and to developing new stimulation hardware allowing more flexible shaping of the current distribution [8].

Stimulation effects, however, also depend on the temporal characteristics of the stimulus waveform. The threshold for activation of neural elements with different membrane excitability properties covaries with stimulus strength, and duration of the stimulus pulse. The non-linear interdependance of stimulus amplitude and pulse duration is reflected by the so called „strength-duration-curve“ or chronaxie relationship. The minimal amount of current necessary to excite a neural element at an infinitely long pulse width (PW) is termed rheobase current. Chronaxie is a measure of the excitability of neural elements and has been defined as the pulse duration equivalent to the double rheobase current on the strength–duration curve.

Experimental measurements have documented that axons have lower chronaxies than neuron cell bodies [9]. Chronaxies for the beneficial effects of DBS have been estimated to be around 129 µs for thalamic and around 151 µs for pallidal stimulation [10, 11] which is well within the range of myelinated axons. Here we present chronaxie evaluations of STN-DBS using a novel neurostimulation system (Vercise ®, Boston Scientific, Valencia, CA). In particular, we explored the clinical usefulness of stimulation at ultra-short pulse

duration as physiological concepts suggest, that stimulation at PW<60 µs could improve the selectivity of DBS for particular neural elements and lead to a better distinction between desirable and adverse stimulation effects.

A.2. Subjects and methods

Four patients (2 female, age 49-62 years), who had been implanted with the Vercise® neurostimulation system (Boston Scientific, Valencia, CA) for bilateral DBS-STN in PD, underwent an extended programming session of their DBS system in the practically defined medication off-state (> 12 hours medication withdrawal) 2-4 months after surgery. Patients were included into the extended monopolar review session for optimizing their stimulation parameters after having had a stable clinical response to STN-DBS of greater than 30% motor score reduction with conventional programming parameters for at least one month. Goal of the monopolar review session was to determine the clinically optimal pulse duration and amplitude setting at the monopolar contact previously selected for chronic stimulation at 60 µs pulse width. Efficacy of neurostimulation was assessed by comparing the severity of motor symptoms at the begin of the review session ON DBS to the preoperative Unified Parkinson's Disease Rating Scale, part III (UPDRS-III) in the medication off-state.

In all patients correct lead positioning had been verified by fusing the preoperative stereotactic MRI and chronic (≥ 40 days) postoperative CT using the stereotactic planning software (Leksell SurgiPlan, Elekta, Sweden). The mean AC-PC based coordinates of active contacts of the right hemisphere were

12.1±0.8 mm lateral to AC-PC 2.14±1.37 mm below AC-PC, 1.62±0.7 mm posterior to MCP, and of left hemispheric active contacts 13.4±0.59 mm lateral, 2.9±1.3 mm below and 1.4±0.8 mm posterior.

For the monopolar review session we defined the efficacy threshold of DBS as the minimal current necessary to achieve complete or almost complete suppression of contralateral rigidity (corresponding to a UPDRS item 22 score of 0 or 1) and the adverse effect threshold as the minimal current inducing clinically noticeable side effects (e.g. muscle contraction). In random order we assessed the therapeutic window (TW) for the pulse durations 20, 30, 40, 50, 60, 90 and 120 µs at a frequency of 130 Hz by quickly ramping up current until adverse effects were noted and carefully titrating the current to determine the exact threshold. Thereafter, current was lowered until contralateral arm rigidity returned to baseline severity (efficacy threshold). If no adverse effect could be encountered after increasing amplitude to 10mA, testing was suspended and no TW could be determined. TW (in mA) was calculated for each tested pulse width by subtracting the efficacy threshold from the side effect threshold. For comparison between subjects TWs were normalized to the TW at 60µs.

We calculated the chronaxies from the threshold currents for suppression of rigidity and muscle contractions by linearizing the strength-duration curves and estimating slope and intercept[12].

A.3. Computational model of axonal activation

An idealized DBS model was constructed to assist in the interpretation of the clinical results. The model system consisted of a finite element electric field model of the DBS electrode, coupled to populations of multi-compartment cable models of myelinated axons. Our previous work described the specific parameters of the electric field model [13] and axon models [14]. The effects of the DBS electric field on the axons were simulated using methods originally described by McNeal [15], adapted to specifically address modulation of the DBS waveform [16] . Our simulations evaluated DBS of two distinct pathways near the DBS electrode. One pathway consisted of smaller (2 um) diameter axons located closer (1-2 mm) the electrode, while the other pathway consisted of larger (5.7 um) diameter axons located farther from (4-5 mm) the electrode. The threshold current for action potential initiation was calculated for each axon model in each pathway, as a function of the pulse width.

A.4. Results

The patients had a mean UPDRS-III motor score improvement from 51±11,97 before surgery to 24,75±8,58 points (-52%) in the medication off-state with STN-DBS.

During the monopolar review session we observed a clear inverse relationship between PW and side effect thresholds in all patients. Mild contractions or fasciculations in hand or face muscles were elicited in all cases and served to determine the threshold for activation of pyramidal tract fibers. We

did not notice other stimulation induced adverse effects below this threshold in any patient. Complete determination of TW was possible for 7 implanted electrodes due to a lack of testable rigidity contralateral to one. The therapeutic window was 2,2±1,6 mA (median 2,3; range 3,9) at 60 µs, which proportionally increased by 182 ± 128% (median 160%; range 341%) at 30µs, while decreasing by 46 ± 28% (median 34%; range 84%) at 120µs (Figure A.1). At 20 µs PW assessment of the TW was unreliable, because we could not elicit a capsular response for 6/8 electrodes below our testing limit of 10 mA .

The threshold current for complete rigidity control increased from 1,6±0,9 (median 1,5; range 2,4) mA at 60 µs to 2,9±1,4 (median 2,8; range 3,6) mA at 30 µs but the calculated total charge delivered per pulse was actually lower: 95±51 (median 90; range 14) nC/pulse at 60 µs vs. 88±43 (median 84; range 108) nC/pulse at 30 µs; -7%).

For both strength duration curves we found a significant linear regression fit (rigidity control: r=0,97; contractions: 0,94), when plotting mean threshold amplitudes against the inverse of pulse duration (Figure A.1). The slopes of the two regression lines were significantly divergent (74,8 ± 5,8 vs. 168,4 ± 19,0; $p<0.0001$) indicating the stimulation of neural elements with different membrane excitability. From the mean and confidence range of the slopes we determined a chronaxie of 225 µs (95% confidence range: 180-270 µs) for the suppression of rigidity and 126 µs (95% confidence range: 90-163 µs) for muscular contractions.

A.5. Discussion

This is the first systematic analysis of the impact of pulse duration on therapeutic and adverse effects of subthalamic deep brain stimulation.

We found, that the therapeutic window of subthalamic neurostimulation increased up to 2 fold when using an ultra-short pulse width of 30 μs compared to the standard pulse width setting of 60μs, currently suggested for STN-DBS programming [6]. At 20 μs pulse duration we could not elicit any capsular response below our upper testing limit of 10mA in 6/8 electrodes suggesting an even better benefit/risk ratio. As expected, the efficacy threshold in mA increased at shorter pulse durations, but the total charge per pulse required for full rigidity control did actually decrease, suggesting that short PW stimulation may not only offer less risk of inducing stimulation induced adverse effects but also improve the energy efficiency of DBS. This would result in greater longevity of primary cell devices or expanded charging cycles of rechargeable pulse generators.

The estimated chronaxie of 168 μs for muscle contraction is well below the limit of <200 μs for fast conducting pyramidal tract fibers, whereas a chronaxie of 222 μs for rigidity suppression indicates stimulation of smaller axons with values between 200 and 700 μs[9]. In order to assist in the interpretation of these clinical results, we devised a computational model consisting of a finite element electric field model of the DBS electrode, coupled to populations of multi-compartment cable models of myelinated axons [17, 18]. The effects of the DBS electric field on the axons were simulated using methods originally described by McNeal[15], adapted to specifically address modulation of the DBS waveform[16]. In keeping

with the chronaxie data, our simulations evaluated DBS of smaller (2 um) diameter axons located closer (1-2 mm) and larger (5.7 um) diameter axons located farther (4-5 mm) from the electrode corresponding to the approximate distance of the pyramidal tract. The current thresholds for generating a propagating axon potential predicted by the model reproduced the marked increase in therapeutic window at pulse durations below 60 μs (Table A.1). Hence, the mechanism of stimulation at short pulse duration may be best explained by focusing on excitation of smaller myelinated axons near the electrode and a steeper falloff for activation of thick myelinated axons with increasing radius of current spread.

Our chronaxie measurements do not allow us to explicitly determine the anatomical nature of the fibers responsible for rigidity control. The chronaxie could represent excitation of a single fiber pathway or a mixed effect of multiple fibers in the subthalamic area, such as corticosubthalamic fibers, pallidothalamic fibers dorsal to the STN or pallidosubthalamic fibers crossing the internal capsule. Rodent models, however, suggest antidromic driving of corticosubthalamic fibers („hyperdirect pathway“) and subsequent retuning of motor cortical spike firing as critical for the antiparkinsonian effect of subthalamic neurostimulation[19, 20]. In the rat the hyperdirect pathway consists of thin collaterals of fast conducting pyramidal tract axons originating from the frontal cortex deep layer V neurons [21]. First imaging studies in humans did indeed visualize the ‘‘hyperdirect’’ pathway as a small bundle traveling along the internal capsule with the highest connectivity in the dorsolateral portion of the STN [22].

Hence, programming in STN-DBS could face the dilemma of needing some current spread into the internal capsule for optimal coverage of those pyramidal tract collaterals, while at the same time avoiding inadvertent stimulation of adjacent corticospinal and corticobulbar fibers.

Our data suggest, that this may be best achieved by stimulating at pulse durations below 60 µs. A limitation may be the small number of patients investigated. However, the results were consistent and the strength-duration relation is a well known physiological phenomenon, which was only reproduced in this study. Variability in our measures could result from the unblinded clinical assessments, but neither rigidity nor fibrillations or contractions as a results of capsular stimulation can be reliably detected using objective methods.

A future clinical study including blinded assessments of stimulation effects on all Parkinsonian symptoms needs to ascertain this concept.

A.6. References

1. Deuschl G, Schade-Brittinger C, Krack P, et al. A randomized trial of deep-brain stimulation for Parkinson's disease. N Engl J Med 2006;355:896-908.
2. Weaver FM, Follett K, Stern M, et al. Bilateral deep brain stimulation vs best medical therapy for patients with advanced Parkinson disease: a randomized controlled trial. JAMA 2009;301:63-73.
3. Williams A, Gill S, Varma T, et al. Deep brain stimulation plus best medical therapy versus best medical therapy alone for advanced Parkinson's disease (PD SURG trial): a randomised, open-label trial. Lancet neurology 2010;9:581-591.
4. Wodarg F, Herzog J, Reese R, et al. Stimulation site within the MRI-defined STN predicts postoperative motor outcome. Movement disorders : official journal of the Movement Disorder Society 2012;27:874-879.
5. Morel A, Magnin M, Jeanmonod D. Multiarchitectonic and stereotactic atlas of the human thalamus. The Journal of comparative neurology 1997;387:588-630.
6. Volkmann J, Moro E, Pahwa R. Basic algorithms for the programming of deep brain stimulation in Parkinson's disease. Mov Disord 2006;21 Suppl 14:S284-289.
7. Butson CR, Cooper SE, Henderson JM, Wolgamuth B, McIntyre CC. Probabilistic analysis of activation volumes generated during deep brain stimulation. Neuroimage 2011;54:2096-2104.
8. Chaturvedi A, Foutz TJ, McIntyre CC. Current steering to activate targeted neural pathways during deep brain stimulation of the subthalamic region. Brain stimulation 2012;5:369-377.
9. Ranck JB. Which elements are excited in electrical stimulation of the mammalian central nervous system: a review. Brain research 1975;98:417-440.
10. Holsheimer J, Demeulemeester H, Nuttin B, de Sutter P. Identification of the target neuronal elements in electrical deep brain stimulation. Eur J Neurosci 2000;12:4573-4577.
11. Holsheimer J, Dijkstra EA, Demeulemeester H, Nuttin B. Chronaxie calculated from current-duration and voltage-duration data. J Neurosci Methods 2000;97:45-50.
12. Groppa S, Herzog J, Falk D, Riedel C, Deuschl G, Volkmann J. Physiological and anatomical decomposition of subthalamic neurostimulation effects in essential tremor. Brain 2013.
13. Butson CR, Maks CB, McIntyre CC. Sources and effects of electrode impedance during deep brain stimulation. Clinical neurophysiology : official journal of the International Federation of Clinical Neurophysiology 2006;117:447-454.
14. McIntyre CC, Grill WM. Extracellular stimulation of central neurons: influence of stimulus waveform and frequency on neuronal output. Journal of neurophysiology 2002;88:1592-1604.
15. McNeal DR. Analysis of a model for excitation of myelinated nerve. IEEE transactions on bio-medical engineering 1976;23:329-337.
16. Foutz TJ, McIntyre CC. Evaluation of novel stimulus waveforms for deep brain stimulation. Journal of neural engineering 2010;7:066008.

17. Butson CR, McIntyre CC. Differences among implanted pulse generator waveforms cause variations in the neural response to deep brain stimulation. Clin Neurophysiol 2007;118:1889-1894.
18. McIntyre CC, Richardson AG, Grill WM. Modeling the excitability of mammalian nerve fibers: influence of afterpotentials on the recovery cycle. Journal of neurophysiology 2002;87:995-1006.
19. Li Q, Ke Y, Chan DC, et al. Therapeutic deep brain stimulation in Parkinsonian rats directly influences motor cortex. Neuron 2012;76:1030-1041.
20. Gradinaru V, Mogri M, Thompson KR, Henderson JM, Deisseroth K. Optical deconstruction of parkinsonian neural circuitry. Science 2009;324:354-359.
21. Kita T, Kita H. The subthalamic nucleus is one of multiple innervation sites for long-range corticofugal axons: a single-axon tracing study in the rat. The Journal of neuroscience : the official journal of the Society for Neuroscience 2012;32:5990-5999.
22. Brunenberg EJ, Moeskops P, Backes WH, et al. Structural and resting state functional connectivity of the subthalamic nucleus: identification of motor STN parts and the hyperdirect pathway. PloS one 2012;7:e39061.

A.7. Figures and tables

Table A.1. Measured and model estimated threshold amplitudes for rigidity control and muscle contractions (capsular response) at different pulse durations.

Pulse Width (μs)	Threshold Amplitude (mA)			
	patient data		model data	
	rigidity control mean±SD	capsular response mean±SD	2 μm axon mean±SD	5.7 μm axon mean±SD
20	3,88±2,03	9,05±0,78	7,75±1,99	10,85±1,17
30	2,94±1,43	7,94±1,30	6,03±1,55	8,43±0,91
40	2,39±1,17	6,14±0,93	4,96±1,27	6,94±0,74
50	1,98±0,98	4,53±1,25	4,23±1,08	5,92±0,63
60	1,59±0,86	3,74±0,92	3,7±0,94	5,18±0,55
70	-	-	3,29±0,84	4,61±0,49
80	-	-	2,98±0,76	4,17±0,44
90	1,21±0,71	2,94±0,68	2,72±0,69	3,81±0,40
100	-	-	2,5±0,64	3,52±0,37
110	-	-	2,33±0,59	3,27±0,35
120	0,63±0,40	2,60±0,89	2,17±0,55	3,06±0,32

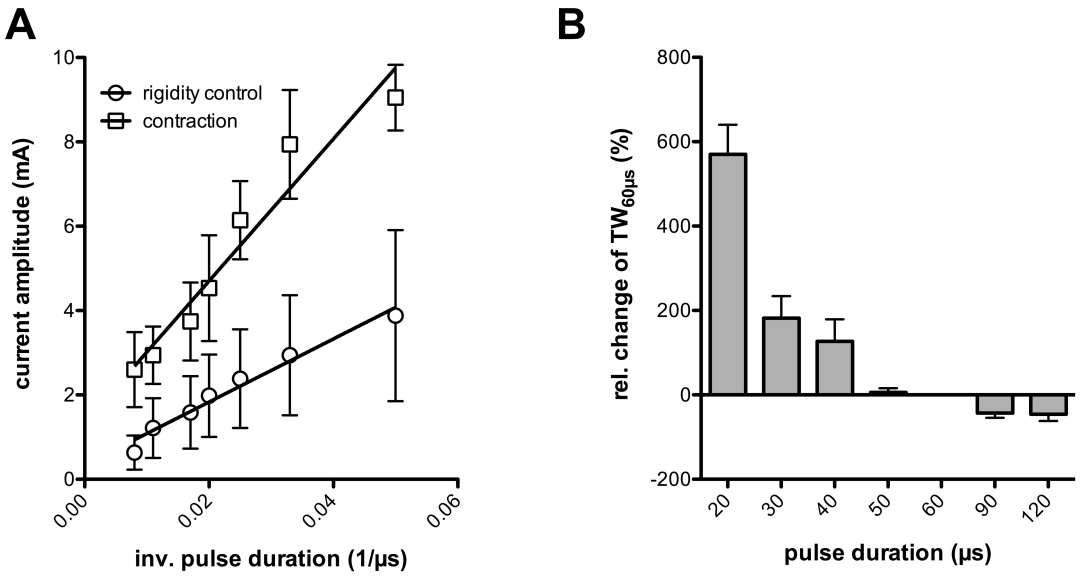

Figure A.1. (A) linearized strength-duration curves for rigidity control and muscle contractions. (B) Bar graph depicting the relative change in therapeutic window compared to 60 μs pulse duration ($TW_{60\mu s}$). Error bars indicate the standard error of mean in both graphs.

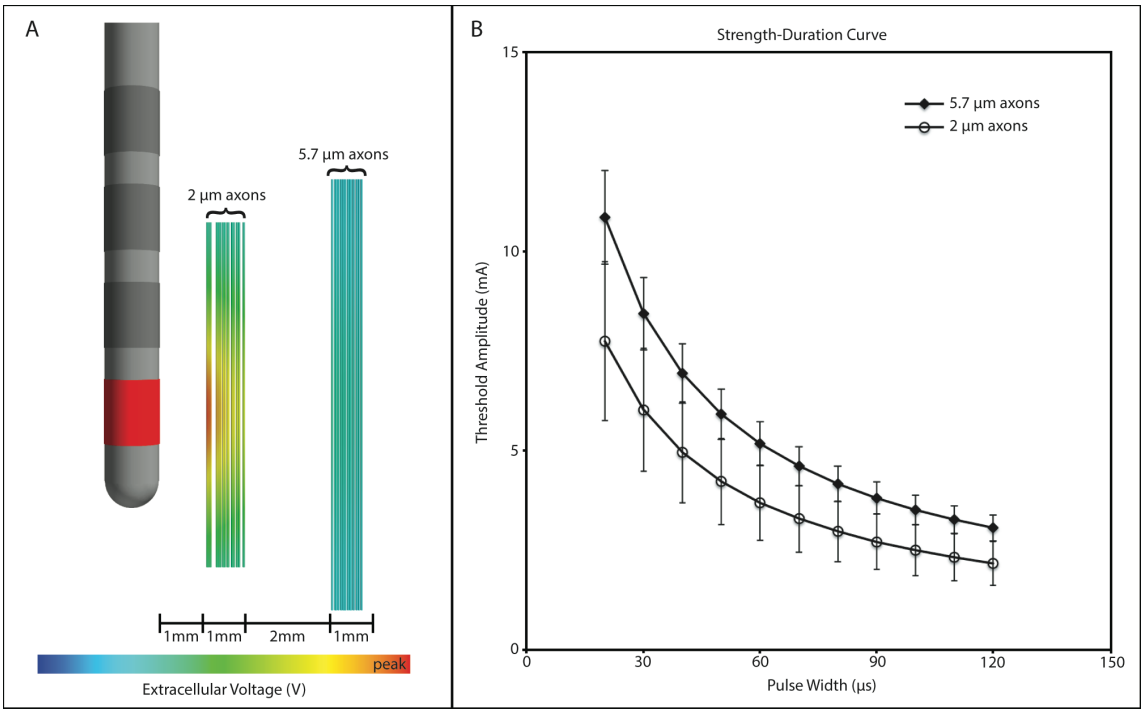

Figure Error! No text of specified style in document.**2.** Model derived strength duration curves for action potential initiation in smaller (2 um) diameter axons located closer (1-2 mm) the electrode as compared to larger (5.7 um) diameter axons located farther from (4-5 mm) the electrode. At shorter pulse duration the two curves diverge explaining an increased „therapeutic window“ if benefit was associated with stimulation of the nearby fibers and adverse effects with the distant thick myelinated axons.

Appendix B – Supporting information for Chapter 2

Gunalan K, Chaturvedi A, Howell B, Duchin Y, Lempka SF, Patriat R, Sapiro G, Harel N, McIntyre CC. Creating and parameterizing patient-specific deep brain stimulation pathway-activation models using the hyperdirect pathway as an example. PloS one. 2017 Apr 25;12(4):e0176132.

B.1. Supplementary methods

B.1.1. Software programs

We used several software programs in the model development (Table B.2). Although each program has methods for data visualization, we wrote custom Python scripts using open source software libraries such as Mayavi (docs.enthought.com/mayavi/mayavi), to combine all data into a single visualization environment. Some of these scripts are available at the McIntyre Lab GitHub site (https://github.com/mcintyrelab).

B.1.2. Image scanning parameters

We scanned the subject using an actively shielded 7T magnet, using SC72 gradients capable of 70 mT/m and a 200 T/m/s slew rate, driven by a Siemens console (Erlangen, Germany). We acquired all 7T images with a 32-element head array coil (Nova Medical, Inc., Burlington, MA) and with the MRI vendor's 3D distortion correction, which compensates for geometrical distortions originating from gradient nonlinearities. We acquired T2W and SW images in

both the coronal and axial orientations centered around the basal ganglia. We acquired DW images with diffusion gradients applied along 50 uniformly distributed directions (b-value = ~1500 s/mm2). We also acquired four additional non-DW images (b-value = 5 s/mm2). We repeated the diffusion acquisition with the same parameters and head position but with the opposite phase encoding direction to allow for distortion correction.

B.1.3. Image pre-processing and co-registration

We corrected DW images for distortions from eddy currents using FSL's `eddy` tool and from magnetic field inhomogeneities using FSL's `topup` tool. We registered all images to the same coordinate system using Advanced Normalization Tools (ANTs) or FSL's linear image registration tool (`flirt`). To facilitate the registration, we extracted non-brain structures from the 1.5T T1W, 7T T1W, 7T T2W, 7T SW, and 7T DW b_0 images using FSL's brain extraction tool (`bet`). As the T2W and SW images have in-plane resolutions of 0.39 mm, the common coordinate system had an isotropic resolution of 0.4 mm.

We used a post-operative CT image to verify the final location of the implanted DBS electrode. First, we registered the CT image to the pre-operative T1W image and then in Cicerone we positioned a model Medtronic 3389 DBS electrode to match the electrode artifact in oblique slices (Fig 2.2C) (Hemm et al., 2009). We exported the coordinates of the collinear contact centers from Cicerone.

B.1.4. Imaging space

In Python, MATLAB, and COMSOL, we positioned all objects according to flipped, scaled voxel space (x,y,z) (Equation B.1). First, we scaled each coordinate in voxel space (i,j,k) by the voxel dimensions ($voxel_x$,$voxel_y$,$voxel_z$), thereby converting the coordinates to millimeters. Next, we obtained the x-axis orientation from the sign of the determinant of the T1W image qform matrix. We used FSL's `fslorient` tool with the `-getqform` flag to obtain the qform matrix. This process can be summarized as follows, where ∘ is the Hadamard product:

$$\begin{pmatrix} x \\ y \\ z \end{pmatrix} = \begin{pmatrix} i \\ j \\ k \end{pmatrix} \circ \begin{pmatrix} voxel_x \\ voxel_y \\ voxel_z \end{pmatrix} \circ \begin{pmatrix} sign(|\text{qform}|) \\ 1 \\ 1 \end{pmatrix} \tag{B.1}$$

Although true anatomical space, as defined by the qform of the NIfTI header, can also be rotated, translated, and sheared, we have elected to ignore those transforms since Python and MATLAB do not handle those transformations easily.

B.1.5. Conductivity tensor field construction

Howell and McIntyre (2017) showed that the heterogeneity in the soft tissues of the head effect the voltage distribution generated by DBS. They defined conductivities for each region outside of the brain instead of a lumped equivalent value for all regions, and compared the results. However, specification of these regions on a patient-specific basis is difficult as it requires manual segmentation of a MRI. Thus we have opted to transform the soft tissues from the multimodal imaging-based detailed anatomical (MIDA) model of

the human head and neck (Iacono et al., 2015). We used a variant of the MIDA model, specifically the $MIDA_{12}$ model as described by Howell and McIntyre (2017). The following is a list of steps for transforming the $MIDA_{12}$ regions outside of the brain to the patient's T1W space (Fig 2.3A): 1) Segmented the patient brain-extracted 1.5T T1W image into tissue types (grey matter, white matter, cerebrospinal fluid [CSF]) with FSL's `fast` tool. 2) Registered the $MIDA_{12}$ brain (grey matter, white matter, and CSF) to the tissue-type segmented patient brain from step 1 with FLIRT using 12 degrees of freedom. 3) Transformed $MIDA_{12}$ head segmentations to the patient T1W space with nearest neighbor interpolation using the transformation from step 2. The following steps will refer to the $MIDA_{12}$ mask that is now in patient space. 4) Calculated overlap in the $MIDA_{12}$ spinal cord/brainstem regions and patient brain. Subtracted remaining spinal cord/brainstem regions from $MIDA_{12}$ mask. 5) Subtracted the patient's brain region from $MIDA_{12}$ mask, thereby leaving soft tissues, skull, and residual brain regions from $MIDA_{12}$. 6) Removed the residual brain regions from $MIDA_{12}$, specifically the dura, grey matter, white matter, and CSF. Reassigned this region to CSF. 7) Added back the remaining $MIDA_{12}$ spinal cord/brainstem regions. 8) Added the tissue-type segmented patient brain from step 1.

The processing steps to transform the $MIDA_{12}$ segmentations to patient space preserve the anatomy of the patient's brain. However, the $MIDA_{12}$ skull is partially removed to ensure preservation of the patient's brain. Another limitation with this method is that the outer boundary of the patient's head is not preserved. Furthermore, anatomical variability exists from patient to patient and thus using

the $MIDA_{12}$ segmentations to define regions outside of the brain is only an approximation.

Once this classification mask was created (Fig 2.3A), we then constructed conductivity tensors, S, that were anisotropic within the brain and isotropic in the encapsulation layer surrounding the electrode and outside of the brain (Table B.3). We constructed the anisotropic and inhomogeneous conductivity tensors within the brain by first using FSL's `dtifit` tool to estimate the diffusion tensors, D, from the DW images. We used FSL's `vecreg` tool to transform the diffusion tensors from DW to T1W space. We then used `vecreg` to down sample this image by a factor of 2. Using eigen decomposition, we decomposed these diffusion tensors to diffusion eigenvalues and diffusion eigenvectors. Using the preservation of tensor electrical load approach, we scaled the diffusion eigenvalues at each voxel to create conductivity eigenvalues (Howell and McIntyre, 2016). This scalar mapping was dependent on whether the tensor was within grey matter, white matter, or CSF. Finally, using the eigenvalues of S, we reconstructed S by assuming that D and S have the same eigenvectors (Basser et al., 1994). We saved a text file with the tensor values at each voxel, resulting in a matrix with a size of M x 9. The first three columns are the x, y, and z coordinates, and the last six columns are the upper triangular portion of S. We imported this text file into COMSOL and the conductivity tensors at each voxel location were interpolated onto the mesh nodes. We visualized the conductivity tensors in Python (Mayavi) to ensure correct registration with the T1W image and

correct orientation of the tensors (Fig 3B/C/D). For this visualization, we used the conductivity eigenvalues to calculate the fractional anisotropy of each tensor.

We used the isotropic conductivity of the encapsulation layer to match the implanted DBS system model impedance to the clinically-measured impedance using the following steps (Fig B.2) (Butson et al., 2006): 1) We used the Medtronic programming device to measure the electrode impedance for contact 2 (-0.7 V, 80 μs, 100 Hz). 2) We solved the FEM, with contact 2 set as the working electrode, for a range of encapsulation layer conductivities (0.05 – 0.2 S/m) (Grill and Mortimer, 1994; Butson et al., 2006). For each encapsulation layer conductivity, we calculated the FEM impedance using Ohm's law (i.e. divided the electrode voltage applied by the total current produced at the electrode surface). 3) For contact 2, to replicate the impedance measurements of the Medtronic programming device, we calculated the implanted DBS system model impedance using Ohm's law by setting R_{Tissue} equal to the FEM impedance, applying a -0.7 V 80 μs stimulus to the circuit in S1 Fig, and measuring the current through R_{Tissue} at 70 μs. 4) We selected the encapsulation layer conductivity that minimized the absolute difference between the implanted DBS system model impedance calculated in Step 3 and the clinical impedance measured with the Medtronic programming device in Step 1, for contact 2 (i.e. 0.07 S/m) (Fig B.2). With the encapsulation layer conductivity set to 0.07 S/m, the implanted DBS system model impedance calculated in Step 3 with contact 2 set as the working electrode was 1493 Ω. It should be noted that impedance is a misnomer. Loads from the IPG are not measured at steady state with sinusoidal

stimuli and thereby are not impedances. Nonetheless, dynamic loads measured with IPGs are referred to as impedances, so we chose to use the same terminology.

B.1.6. Surface mesh processing

To define the brain and head volumes, we used `bet` to extract the patient-specific inner skull surface mesh from the 1.5T T1W image (Fig 2.2A/B), and used Seg3D to extract the outer head surface mesh from the $MIDA_{12}$ volume (Section B.1.5). We ran `bet` with the fractional intensity threshold that yielded the best qualitative extraction of the inner skull surface. For the patient presented in this manuscript, we used a fractional intensity value of 0.4. This tessellated surface mesh typically results in a high number of faces, which would cause COMSOL to take a long time to solve. Therefore, we imported this surface mesh into MeshLab and decimated to reduce the number of faces to less than 1000. Specifically, we applied the 'Quadratic Edge Collapse Decimation' filter three times with the percentage reduction set to 0.5. After each decimation step, we applied the 'Laplacian smooth (surface preserve)' filter to maintain a uniform distribution of faces. We registered the tissue-type segmented $MIDA_{12}$ brain to the tissue-type segmented patient brain with FLIRT using 12 degrees of freedom (Section B.1.5). We used this transformation to transform the $MIDA_{12}$ outer head surface mesh to the patient T1W space. In MeshLab, we converted these triangular meshes to quadratic meshes with the 'Tri to Quad by 4-8 subdivision' filter and exported it as an *.off file. To ensure there was no overlap,

we imported the two meshes into MeshLab. Because COMSOL cannot import quadratic meshes, we converted these meshes to a non-uniform rational basis spline (NURBS) file format in MATLAB using the 'NURBS Toolbox by D.M. Spink'. We then imported these meshes into COMSOL to ensure there was no overlap.

B.1.7. Finite element model – Other details

We defined floating potential boundary conditions of 0 A net current through the inactive contacts, and Neumann boundary conditions of 0 A/mm^2 along the electrode shaft (except for the contacts) and head surface (except for the neck region).

We created a cube centered around the electrode contacts with a side length of 30 mm that was meshed at a higher resolution. We aligned the electrode, encapsulation layer, and cube to the contact coordinates using Rodrigues' rotation formula. The entire mesh contained 1,429,416 tetrahedral elements (head outside brain – 293,054; brain outside 30 mm cube – 834,778; brain inside 30 mm cube – 229,580; encapsulation layer – 72,004). We generated a second mesh with increased resolution to ensure solution convergence (total – 2,347,048; head outside brain – 293,863; brain outside 30 mm cube – 1,177,452; brain inside 30 mm cube – 440,303; encapsulation layer – 435,430).

B.1.8. Nuclei segmentation

We performed manual segmentation of subcortical structures (i.e. putamen, globus pallidus externus, globus pallidus internus, subthalamic nucleus, substantia nigra, and red nucleus) using Seg3D, on the image that provided the best contrast for the nuclei of interest in the common coordinate system (Fig 2.4A and Table B.3). Because Seg3D doesn't permit exporting the files in the NIfTI file format, we exported the files in the nearly raw raster data (NRRD) file format, and converted to NIfTI in 3DSlicer. The resulting NIfTI file had an incorrect orientation, so we implemented the `fslorient -forceradiological` and `fslreorient2std` commands to correct this error. Tools are currently under development to automate these subcortical segmentations (Kim et al., 2014).

Due to a lack of contrast in the 1.5T and 7T T1W images, thalamic segmentation was difficult. Therefore, to define the thalamus, we used the Harvard-Oxford subcortical structural atlas distributed within FSL. Specifically, we used Cicerone to fit the thalamus to the 1.5T T1W image with 9 degrees of freedom (Miocinovic et al., 2007).

In the axial view, we used Seg3D to segment the seed and target masks used in the tractography algorithm (Fig B.3). We defined the seed mask as the white matter between the thalamus and lenticular nucleus, 1.2 mm superior to the STN. We defined two target masks, one superior to the seed mask and one inferior to the seed mask. We defined the superior target mask as the white matter between the thalamus and lenticular nucleus, 10.8 mm superior to the

seed mask. We defined the inferior target mask as the cerebral peduncle of the midbrain, 17.2 mm inferior to the seed mask.

For tractography, we used an exclusion mask that included the ipsilateral thalamus, globus pallidus, putamen, CSF, and contralateral hemisphere. We used Freesurfer's `recon-all` tool to segment the ipsilateral CSF and contralateral hemisphere masks from the 1.5T T1W image. First, we converted the output file from `recon-all` (aparc+aseg.mgz) to a NIfTI file format with Freesurfer's `mri_convert` tool. Next, we used FSL's `fslmaths` tool to extract the regions of interest from the output file with the threshold flags (`-thr`, `-uthr`) and subsequently binarized with the `-bin` flag. We then used `mri_convert -rl` to reslice this image to the original T1W image dimensions.

B.1.9. Probabilistic tractography

After we segmented the patient-specific subcortical masks, the next step was to reconstruct streamlines that would be used to define the axon trajectories. We reconstructed two sets of streamlines that represented corticofugal axons of the hyperdirect pathway and internal capsule fibers of passage. We used FSL's `bedpostx` tool to estimate the parameters for a diffusion model in each voxel (Behrens et al., 2007). Next, we used FSL's `probtrackx` tool to perform probabilistic tractography from the seed mask, with 100 streamlines generated from each seed voxel. We saved the coordinates of each streamline by passing the `-V 2` option when running `probtrackx`. One constraint was that the streamline files were generically named (i.e. particle0, particle1, etc.) for each

seed voxel. Therefore, when more than one seed voxel was run with the same `probtrackx` instance, the files were overwritten with the results for each subsequent seed voxel. To save the streamlines for all voxels within the seed mask, for each voxel we ran a separate instance of `probtrackx` and concatenated the streamline files into a single file. We ran each instance of `probtrackx`, followed by the streamline processing described below, on a computational cluster to decrease the computation time.

We processed the streamlines exported from `probtrackx` to identify the streamlines that originated from the seed mask, intersected both target masks, and avoided exclusion masks and the electrode (Fig 2.4B). First, the streamline coordinates exported from `probtrackx` were in DW space, so we used FSL's `img2imgcoord` tool and the DW-to-T1W transformation matrix to calculate the streamline coordinates in T1W space. We manipulated the streamline so that it formed a continuous path from the superior end of the streamline, through the seed voxel, and to the inferior end. As the streamlines were now in T1W space, we scaled the streamlines by the voxel dimensions to convert the streamlines from voxel space to millimeter space (Section B.1.4). Furthermore, we obtained the x-axis orientation from the sign of the determinant of the T1W image qform matrix. In our example, we multiplied the x values by -1.

Next, we checked to determine if a streamline intersected with both target masks. If so, we cropped the streamline between the target masks and if not, we excluded it from further analysis. If the cropped streamline took a trajectory above or below the superior or inferior target masks, respectively, we excluded it

from further analysis. Additionally, if the cropped streamline intersected the electrode or the exclusion mask, we also excluded it from further analysis. Subsequently, we concatenated the processed streamline files for all seed voxels into the same file. In our example, 13,219 streamlines originated from the seed mask, terminated in the target masks, and avoided the electrode and exclusion mask.

B.2. Supplementary tables

Table B.1. Imaging parameters. All MRI scans were acquired pre-operatively while the CT scan was acquired post-operatively. T2W and SW images were acquired in both coronal and axial orientations.

Image	Sequence	FOV (mm^3)	Matrix	Voxel resolution (mm^3)	Other parameters	Acquisition time (minutes)
1.5T T1W	3D gradient echo MPRAGE	250x187x176	256x192x176	0.98x0.98x1.0	TR = 1650 ms TI = 1100 ms TE = 3.02 ms Flip angle = 15°	10
7T T1W	3D gradient echo MPRAGE	230x187x153	312x384x256	1.0x1.0x1.0	TR = 3100 ms TI = 1500 ms TE = 3.5 ms Flip angle = 6° Acceleration factor of 2 (GRAPPA) along the phase-encoding direction.	6.5
7T T2W	2D turbo spin echo	200x200x26	512x512x26	0.39x0.39x1.0	TR = 9000 ms TE = 58 ms Flip angle = 150° Acceleration factor of 3 (GRAPPA) along the phase-encoding direction.	7.5
7T SW	3D flow-compensated gradient echo	200x200x48	512x512x60	0.39x0.39x0.8	TR = 28 ms TE = 21 ms Flip angle = 17° Pixel bandwidth = 121 Hz/pixel 6/8 partial Fourier parallel imaging using an acceleration factor of 2 (GRAPPA) along the phase-encoding direction.	4
7T DW	Single refocused 2D single-shot spin echo echo planar imaging	204x204x99	136x136x66	1.5x1.5x1.5	TR = 4896 ms TE = 56 ms Flip angle = 90° Pixel bandwidth = 1671 Hz/pixel Acceleration factor of 3 (GRAPPA).	4.5
CT	-	302x200x302	512x334x512	0.59x0.6x0.59	120 kV 315 mAs Gantry tilt = 0.0°	0.5

Table B.2. Software programs utilized in the scientific workflow.

Software	Version	Website	Citation
COMSOL Multiphysics	5.1	comsol.com/comsol-multiphysics	-
Python	2.7.8	python.org	-
MATLAB	8.0.0.783	mathworks.com/products/matlab	-
NEURON	7.3	neuron.yale.edu	Hines and Carnevale, 2001
FSL	5.0.7	fsl.fmrib.ox.ac.uk/fsl/fslwiki	Jenkinson et al., 2012
Freesurfer	5.3.0	surfer.nmr.mgh.harvard.edu	Fischl, 2012
Seg3D	2.3.0	seg3d.org	-
Cicerone	-	ciceronedbs.org	Miocinovic et al., 2007
MeshLab	1.3.3	meshlab.sourceforge.net	-
3DSlicer	4.4.0	slicer.org	-

Table B.3. Isotropic conductivities for tissue types.

Tissue	Isotropic conductivity (S/m)
Grey matter	0.23
White matter	0.14
Cerebrospinal fluid	1.45
Glial scar	0.07
Muscle	0.32116
Tendon	0.38271
Bone	0.020157
Fat	0.022405
Skin	0.00020006
Disk	0.65
Blood	0.7
Air	1e-12

Table B.4. Images and methods for segmenting structures.

Structure	MRI	Method
Thalamus	1.5T T1W	Manual fitting
Caudate	7T T1W	Manual segmentation
Putamen	7T T2W (or SW) axial	Manual segmentation
Globus pallidus externus	7T T2W (or SW) axial	Manual segmentation
Globus pallidus internus	7T T2W (or SW) axial	Manual segmentation
Subthalamic nucleus	7T T2W (or SW) coronal	Manual segmentation
Substantia nigra	7T T2W (or SW) coronal	Manual segmentation
Red nucleus	7T T2W (or SW) coronal	Manual segmentation
Contralateral hemisphere	1.5T T1W	Automated segmentation
Cerebrospinal fluid	1.5T T1W	Automated segmentation

B.3. Supplementary figures

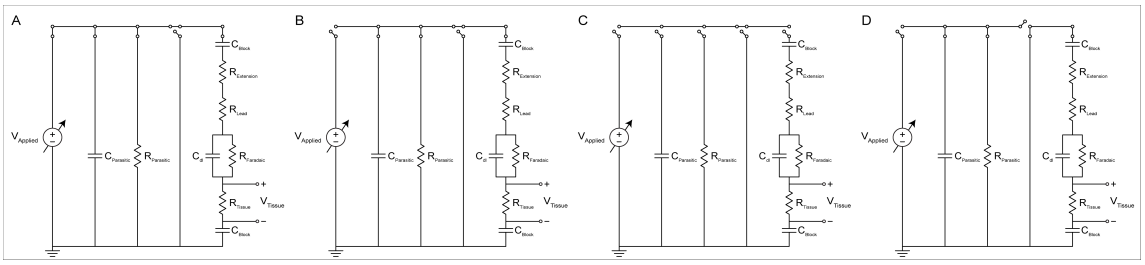

Figure B.1. Equivalent electrical circuit diagram of the implanted DBS system for voltage-regulated, monopolar stimulation. The circuit included representations of the blocking capacitors (C_{Block}), extension wire resistance ($R_{Extension}$), lead wire resistance (R_{Lead}), electrode-tissue interface with a double-layer capacitance (C_{dl}) and Faradaic resistance ($R_{Faradaic}$) in parallel, and tissue resistance (R_{Tissue}). A 'parasitic' capacitance ($C_{Parasitic}$) and 'parasitic' resistance ($R_{Parasitic}$) were included in parallel with the load of the DBS system. (A) During the cathodic phase the circuit is driven by the voltage source ($V_{Applied}$) (60 μs). (B) During the first portion of the interphase interval the voltage source is disconnected from the circuit (10 μs), and (C) during the second portion of the interphase interval the parasitic capacitance and parasitic resistance are also disconnected (70 μs). (D) During the passive charge recovery phase the DBS system load is connected to ground, and the parasitic capacitance and parasitic resistance are connected to each other (3.686 ms).

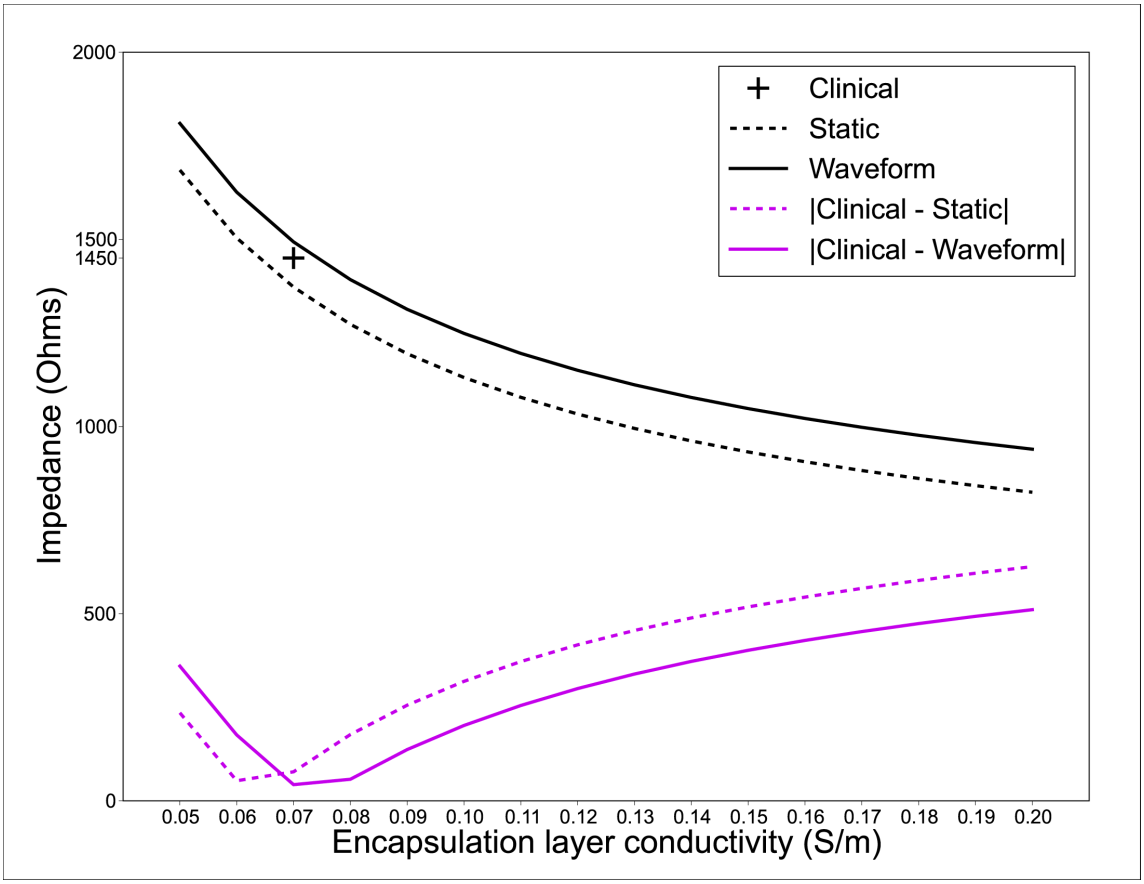

Figure B.2. Patient-specific definition of the encapsulation layer conductivity. The impedance of the finite element model (FEM) ('Static', black dashed line) and implanted DBS system model ('Waveform', black solid line) as a function of the encapsulation layer conductivity for contact 2. To replicate the Medtronic clinical impedance measurement (crosshair), we calculated the implanted DBS system model impedance at 70 μs into an 80 μs pulse. The difference between the clinical impedance measured with the Medtronic programming device and the two model impedances is shown in purple.

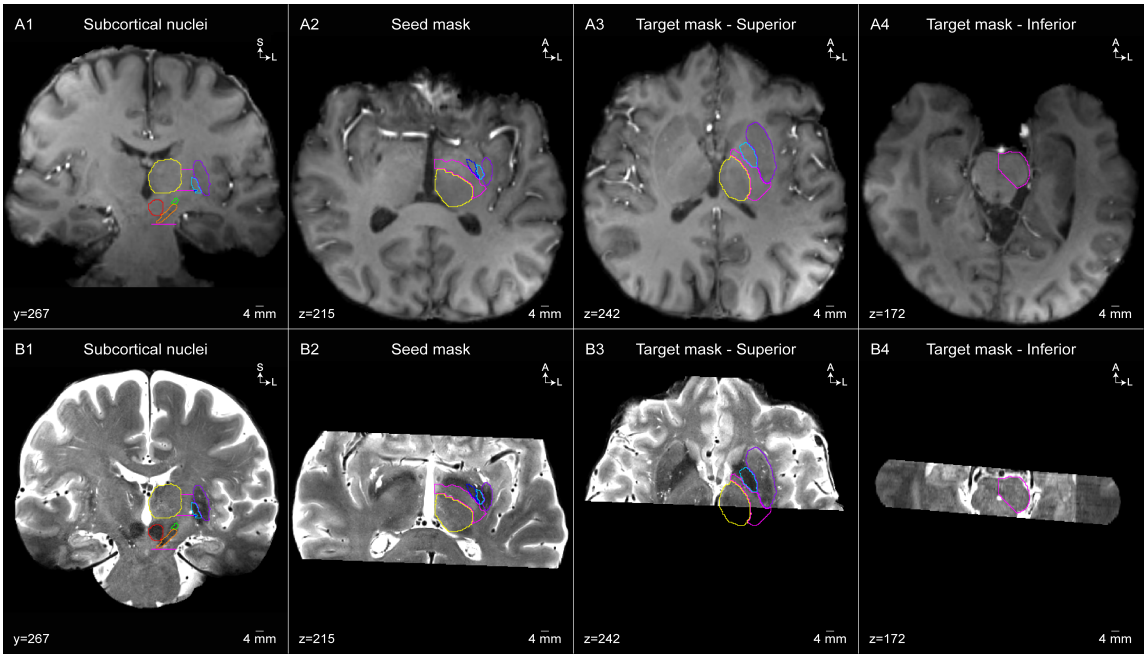

Figure B.3. Seed and target masks used by the probabilistic tractography algorithm to generate streamlines representing corticofugal axons. The subcortical nuclei outlined on the (A) T1-weighted image and (B) T2-weighted coronal image (subthalamic nucleus [STN] - green, substantia nigra – orange, red nucleus – red, thalamus – yellow, putamen – purple, globus pallidus externus – light blue, globus pallidus internus – dark blue). The 3 pink lines indicate the seed and target masks shown in A2-A4 and B2-B4. (A2), (B2) The seed mask was defined as the white matter between the thalamus and lenticular nucleus, 1.2 mm superior to the STN. (A3), (B3) The superior target mask was defined as the white matter between the thalamus and lenticular nucleus, 10.8 mm superior to the seed mask. (A4), (B4) The inferior target mask was defined as the cerebral peduncle of the midbrain, 17.2 mm inferior to the seed mask.

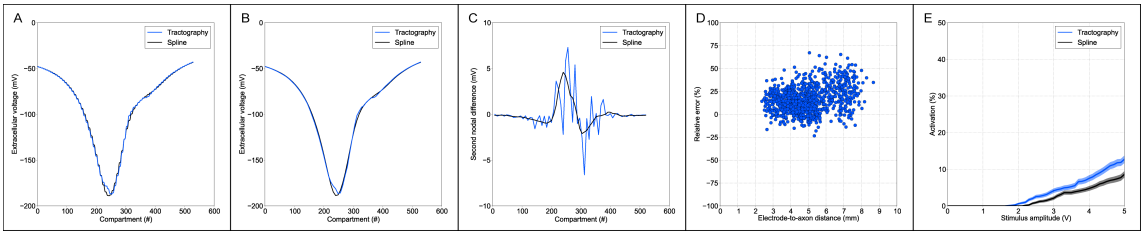

Figure B.4. Differences between a tractography-generated streamline and a smoothing spline fit to a tractography-generated streamline. (A-C) Based off of corticofugal streamline shown in Fig 4C. (A) Extracellular voltage at the axon compartment midpoints along the tractography-generated streamline (blue) and spline-based streamline (black). (B) Extracellular voltage at the nodal compartment midpoints along the tractography-generated streamline and spline-based streamline. (C) Second nodal differences of the extracellular voltages along the tractography-generated streamline and spline-based streamline. (D) Stimulus threshold errors and (E) recruitment curves for the internal capsule fibers of passage axon models defined from the tractography-generated streamlines and spline-based streamlines.

B.4. Supplementary videos

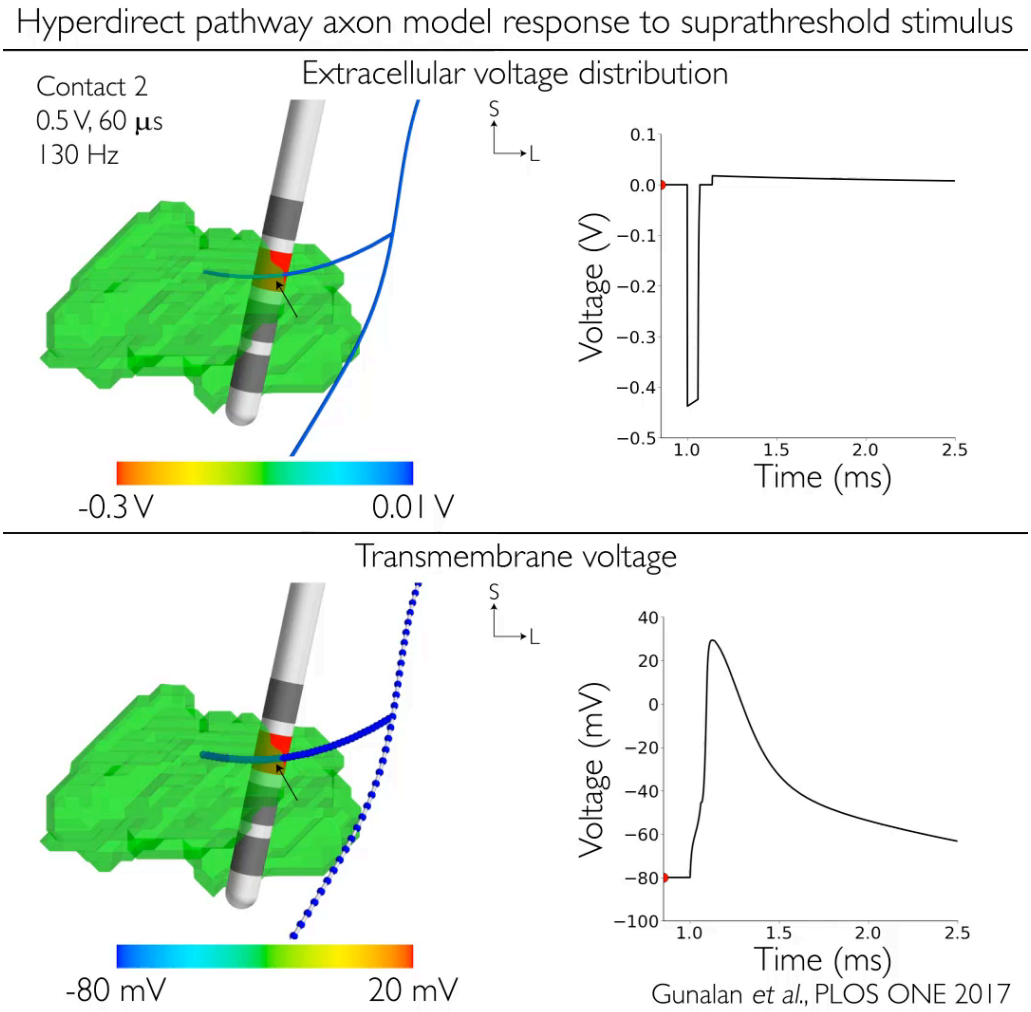

Figure B.5. Hyperdirect pathway axon model response to stimulation. In this example, the stimulation setting chosen is suprathreshold and thus generates an action potential that propagates orthodromically and antidromically (subthalamic nucleus –green). All four images are simultaneously changing over time to show: (A) the extracellular voltage distribution generated by the DBS electrode that is used to stimulate the model axon; and (B) the change in transmembrane voltage in response to stimulation. The line plots show the change in voltage at the node of Ranvier where action potential initiation occurs (black arrow).

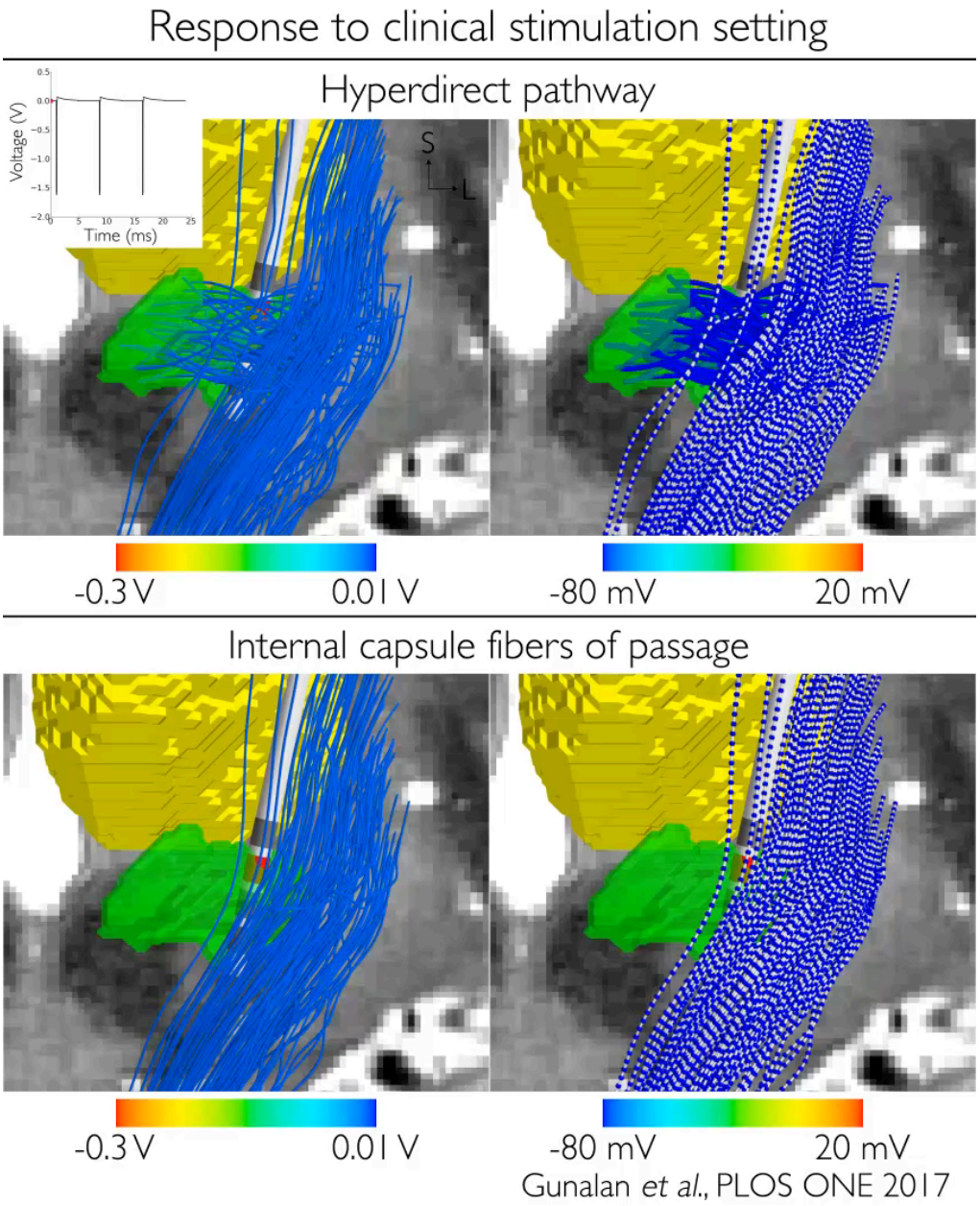

Figure B.6. Model predictions for the response of 100 hyperdirect pathway axons and 100 internal capsule fibers of passage to the clinically effective stimulation setting. All five images are simultaneously changing over time to show (subthalamic nucleus – green; thalamus – yellow): (Left) the extracellular voltage distribution generated by contact 2 (red) that is used to stimulate the model axons; (Inset) the time course of the stimulus waveform; and (Right) the membrane voltage response to stimulation. For this stimulation setting (contact 2 [cathode], IPG case [anode], 1.7 V, 60 μs, 130 Hz), 14 hyperdirect pathway axons and zero internal capsule fibers of passage generate propagating action potentials in response to each stimulus pulse.

Appendix C – Supporting information for Chapter 3

C.1. Supplementary methods

C.1.1. Weights for DF-Peterson

For a given stimulus pulse width (PW) and axon diameter (D), weights are calculated by applying a monophasic intracellular point-source stimulus that is PW in duration to a node of Ranvier (NoR). At a reference NoR, the maximum transmembrane voltage (i.e. the maximum $V_{m,0}$) reached during or after stimulation is calculated. The middle NoR of a long cable is typically designated as the reference NoR, which in the above description (Section 3.2.2.1), corresponds to $i = 0$. The process is then repeated by applying the intracellular stimulus, one at a time, to all other NoR. w_i is the maximum $V_{m,0}$ observed over time when the stimulus is applied at the i^{th} NoR divided by the same quantity but when the stimulus is applied to the reference NoR at $i = 0$. w_0 is thereby 1, and all other w_i are between 0 and 1. For more details on the motivation behind this type of weighting, we refer the reader to the work by Warman et al. [1992].

C.1.2. Bilinear interpolation

We used bilinear interpolation to approximate parameters and values used in DF-Peterson and VTA-Astrom at combinations of D and PW not reported in the respective works. In DF-Peterson, we are referring to the weights, $\Phi_{e,0,th}$, and MDF_{th} (see Section 3.2.2.1); and in VTA-Astrom, we are referring to $E_{T,th}$

(see Section 3.2.3.3, Figure C.2). To approximate the dependent variable of interest, *y**, we applied the following matrix formula:

$$y^* = \begin{bmatrix} 1 & D^* & PW^* & D^*PW^* \end{bmatrix} \begin{bmatrix} 1 & D_1 & PW_1 & D_1PW_1 \\ 1 & D_1 & PW_2 & D_1PW_2 \\ 1 & D_2 & PW_1 & D_2PW_1 \\ 1 & D_2 & PW_2 & D_2PW_2 \end{bmatrix}^{-1} \begin{bmatrix} y_{11} \\ y_{12} \\ y_{21} \\ y_{22} \end{bmatrix} \quad \text{(C.1)}$$

, where D* and PW* are the respective independent variables. D_1 and D_2 are the closest values (inclusive) below and above D*, respectively; PW_1 and PW_2 are the closest values (inclusive) above and below PW*, respectively; and y_{ij} is the respective value at D_i and PW_j, for i,j = 1,2. Note, multiplication of the latter two matrices in Equation C.1 yields the coefficients for bilinear interpolation.

C.1.3. Activation volume tractography

Activation volume tractography (AVT) was performed by calculating those streamlines that originated from the VTA-Chaturvedi ellipsoid and terminated in the ventral lateral posteroventral (VLpv) thalamic nucleus (Figure 3.11B). We performed tractography from the voxels with centers within a 1 V VTA-Chaturvedi ellipsoid (Figure 3.11B2). We used 320 seeds per voxel, which was equivalent to 5,000 seeds per mm^3. Those streamlines that intersected the VLpv thalamic nucleus and avoided the ipsilateral CSF and contralateral cerebral hemisphere were retained (Figure 3.11B3). This resulted in a total of 37,163 streamlines, or 16.0% of the streamlines originating from the VTA-Chaturvedi. We repeated this process but also excluded streamlines that passed through the globus pallidus, substantia nigra, ventral lateral anterior (VLa) thalamic nucleus, ventral posterior

lateral (VPL) thalamic nucleus, and took a trajectory above the VLpv thalamic nucleus, totaling 7 exclusion criteria. This resulted in 31,911 streamlines, or 13.7% (Figure 3.11B4). We also performed tractography for a 2 V VTA-Chaturvedi ellipsoid with all 7 exclusion criteria, which totaled 52,450 streamlines or 15.1% (Figure 3.11B5).

C.2. Supplementary tables

Table C.1. Maximum absolute difference in percent activation between each predictor and the FC PAM, for the range of 0-5 Volts. This analysis is based on the data presented in the recruitment curves in Figures 8 and 9. '-' signifies that the predictor was not developed for the pulse width and axon diameter combination and 'X' signifies that the FC PAM values predicted 0% activation for the entire range. Data is presented for the internal capsule fibers of passage (IC), hyperdirect pathway (HDP), and cerebellothalamic tract (CbTT).

Axon diameter (µm)	Pulse width (µs)	DF-Peterson			VTA-Chaturvedi			VTA-Madler			VTA-Astrom		
		IC	HDP	CbTT	IC	HDP	CbTT	IC	HDP	CbTT	IC	HDP	CbTT
2.0	**90**	X	3.2	0.7	X	7.1	2.5	--------	--------	--------	X	19.5	1.7
5.7	**30**	4.4	7.7	15.3	--------	--------	--------	--------	--------	--------	22.4	57.0	24.0
5.7	**60**	5.6	6.2	6.2	1.9	37.0	5.4	--------	--------	--------	47.1	62.7	38.8
5.7	**90**	3.3	2.9	4.0	6.3	28.7	15.8	3.7	31.1	13.4	47.2	58.1	34.7
5.7	**120**	3.8	6.8	10.3	13.6	32.1	26.9	--------	--------	--------	46.4	55.4	30.7
10.0	**90**	53.6	25.9	60.7	11.3	69.1	32.8	--------	--------	--------	--------	--------	--------

C.3. Supplementary figures

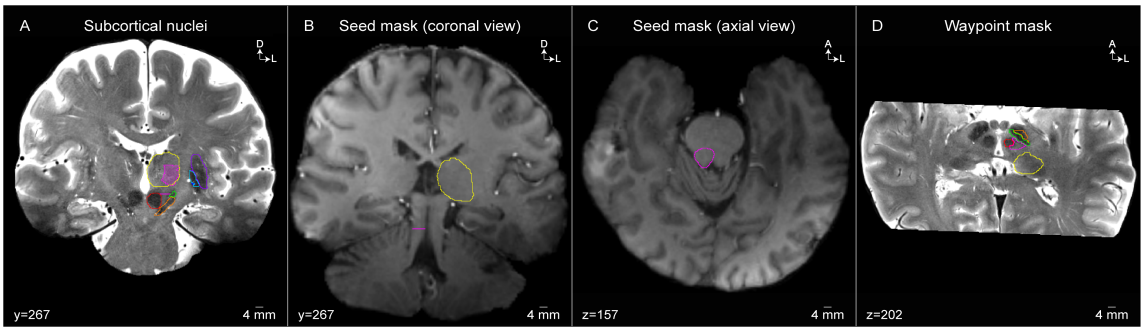

Figure C.1. Masks for constructing the cerebellothalamic tract with tractography. (A) Coronal view of subcortical nuclei overlaid on the 7T T2-weighted (T2W) image (subthalamic nucleus—green, substantia nigra–orange, red nucleus–red, thalamus–yellow, ventral lateral posteroventral thalamic nucleus–striped pink, putamen–purple, globus pallidus externus–light blue, globus pallidus internus–dark blue). The pink line indicates the waypoint mask shown in D. (B) Coronal view of the seed mask in the superior cerebellar peduncle (pink) overlaid on the 7T T1-weighted (T1W) image. (C) Axial view of the seed mask in the superior cerebellar peduncle (pink) overlaid on the 7T T1W image. (D) Axial view of the waypoint mask between the subthalamic nucleus and red nucleus overlaid on the 7T T2W image.

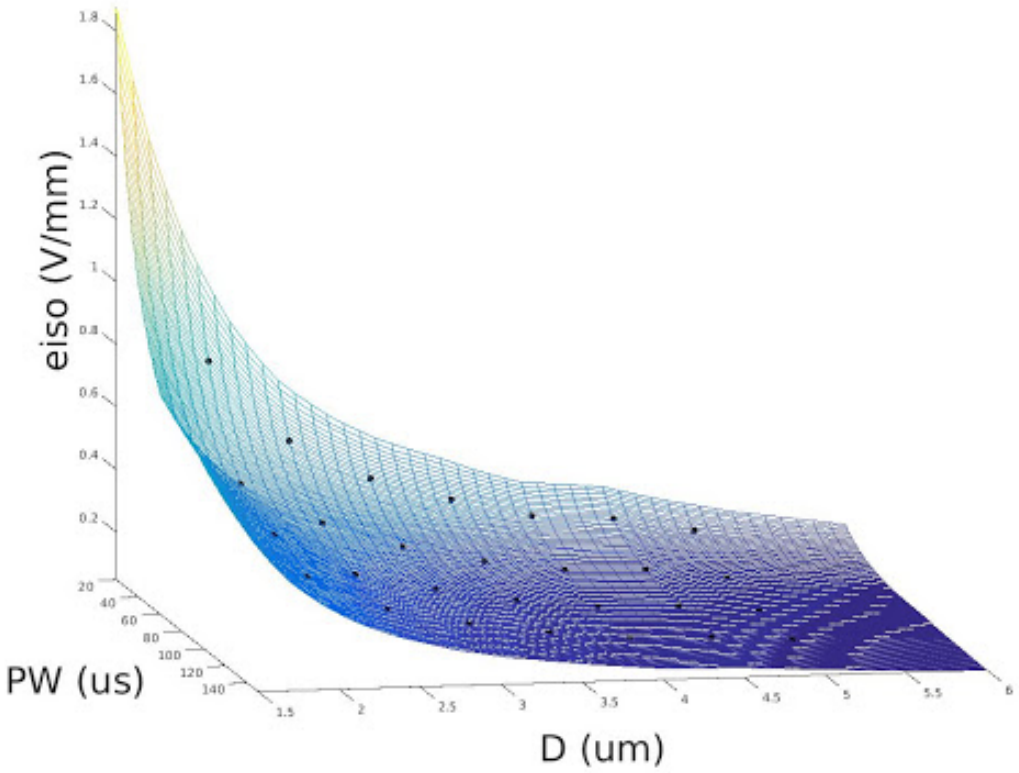

Figure C.2. VTA-Astrom electric field strength threshold values ($E_{T,th}$). We used bilinear interpolation of the reported values (black dots) to create a continuous function. PW=pulse width; D=axon diameter.

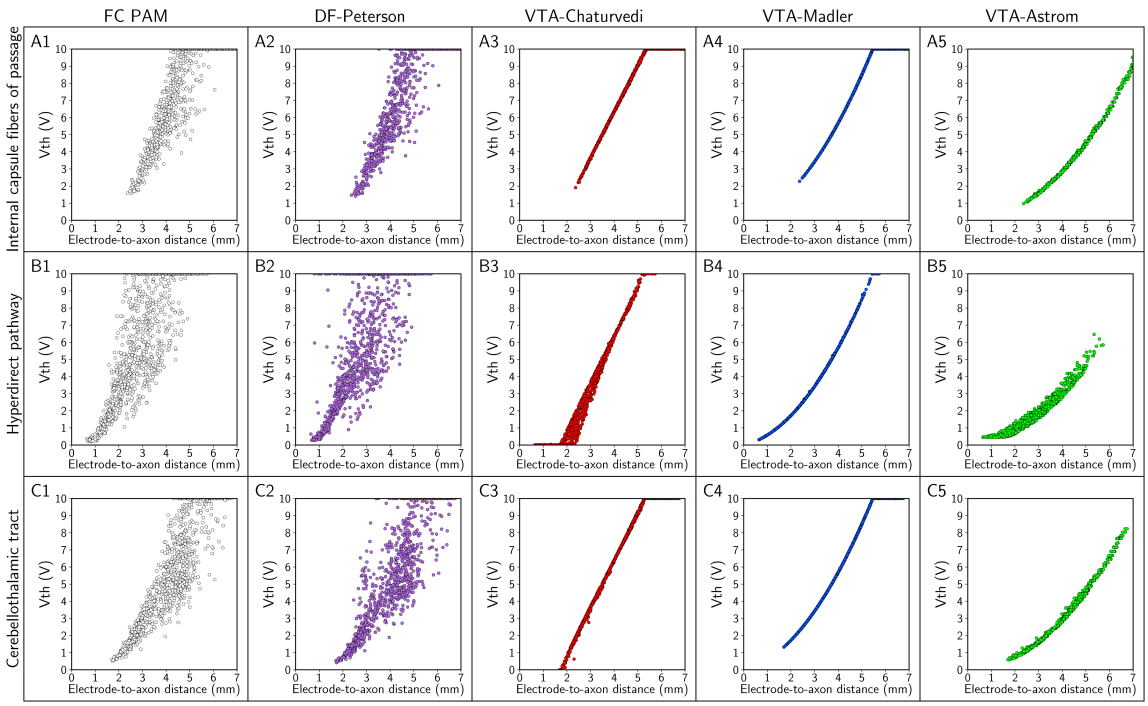

Figure C.3. Strength-distance relationship of the threshold stimulus amplitudes (V_{th}) for action potential initiation calculated with the FC, DF, and VTA PAMs. Thresholds were calculated for the: (A) internal capsule fibers of passage, (B) hyperdirect pathway, and (C) cerebellothalamic tract. The stimulus pulse width was 90 µs, electrode configuration was contact 2 (-), case (+), and axon diameter was 5.7 µm. In this plot, we set axons with V_{th} > 10 V as 10 V, so that all axons representing a pathway can be visualized in the field of view. Note, electrode-to-axon distance is calculated from the center of the electrode contact.

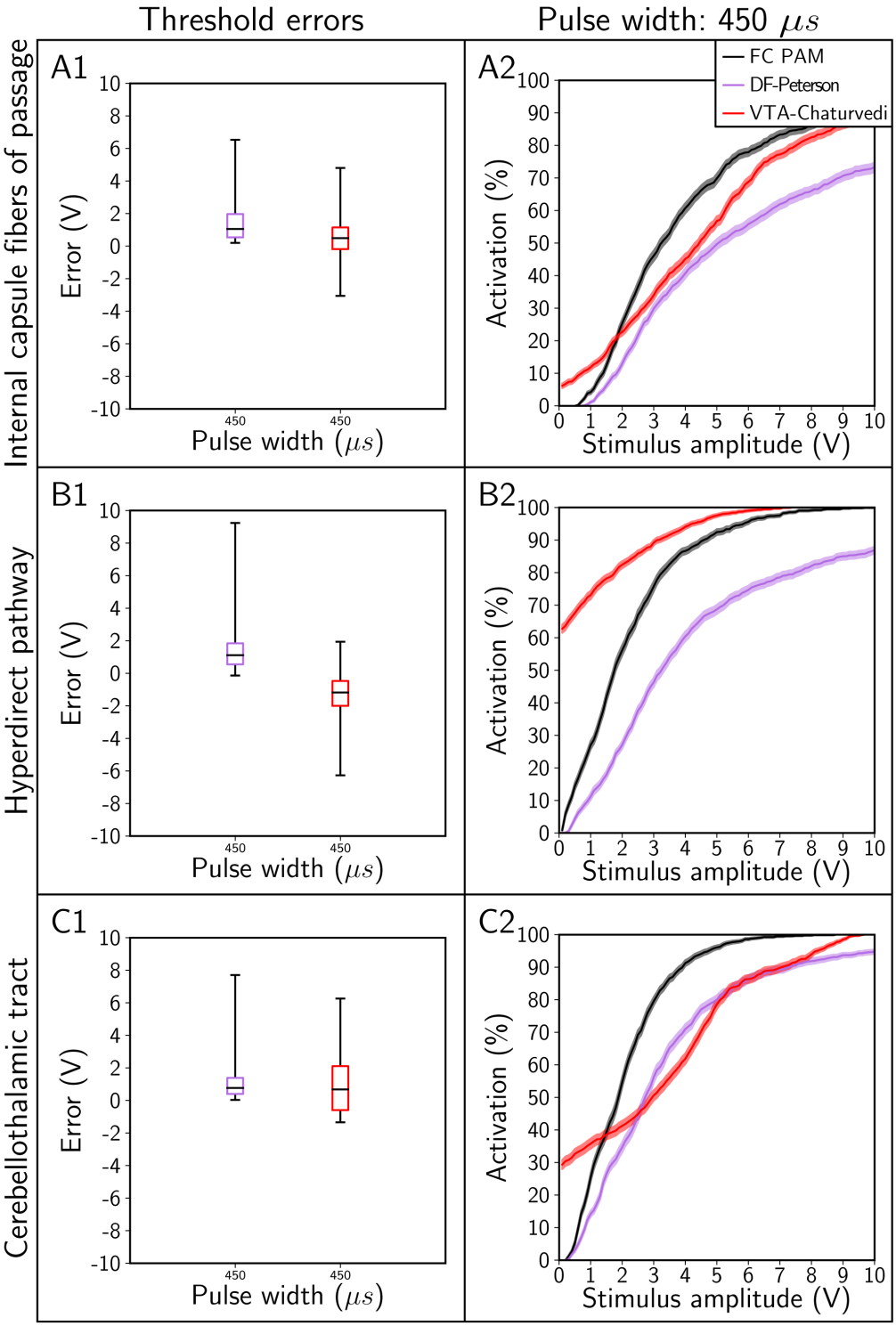

Figure C.4. Errors in stimulation thresholds and recruitment curves generated with the FC, DF, and VTA PAMs using a pulse width of 450 µs. Recruitment curves were calculated for the: (A) internal capsule fibers of passage, (B) hyperdirect pathway, and (C) cerebellothalamic tract. The electrode configuration was contact 2 (-), case (+) and axon diameter was 5.7 µm.

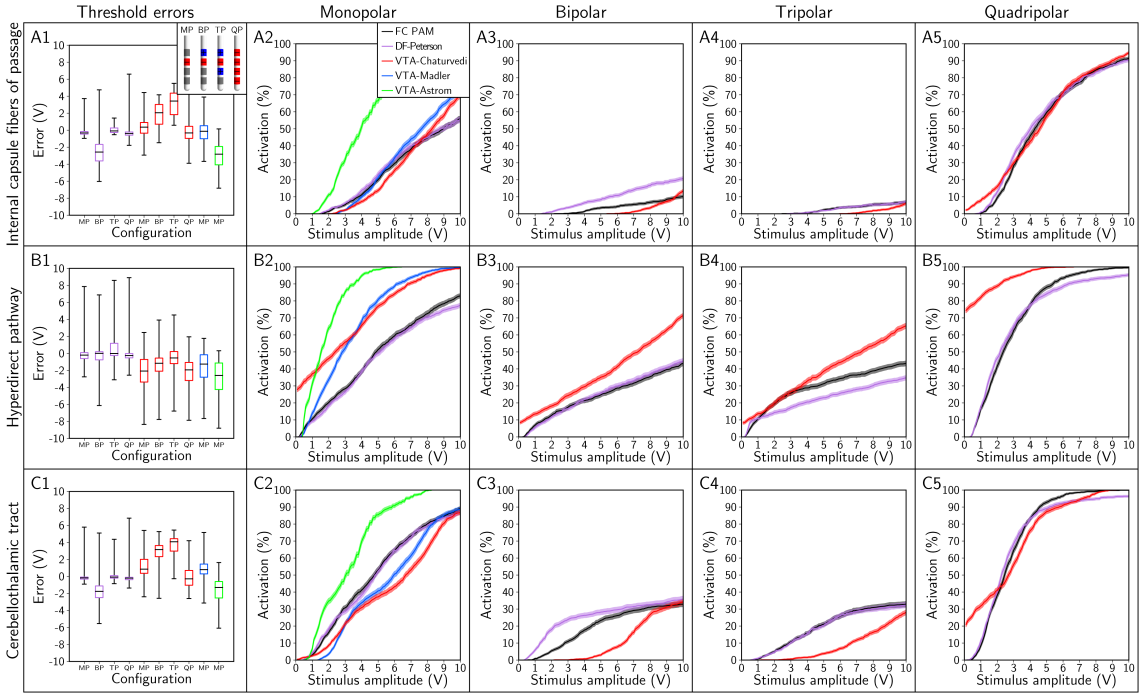

Figure C.5. Errors in stimulation thresholds and recruitment curves generated with the FC, DF, and VTA PAMs for electrode configurations of monopolar (MP; contact 2 [-], case [+]), bipolar (BP; contact 2 [-], contact 3 [+]), tripolar (TP; contact 1 [+], contact 2 [-], contact 3 [+]), and quadripolar (QP; contact 0 [-], contact 1 [-], contact 2 [-], contact 3 [-], case [+]). Recruitment curves were calculated for the: (A) internal capsule fibers of passage, (B) hyperdirect pathway, and (C) cerebellothalamic tract. The stimulus pulse width was 90 μs and axon diameter was 5.7 μm.

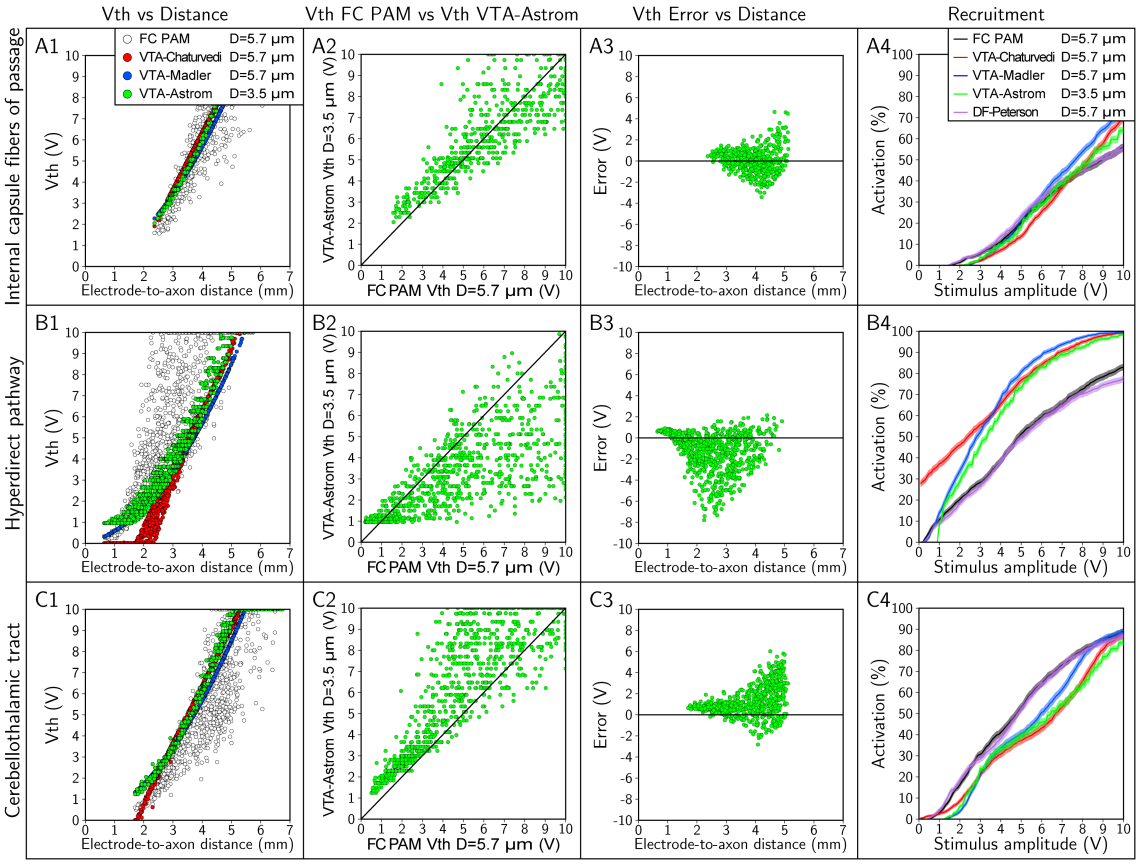

Figure C.6. Results for the VTA PAM developed by Astrom et al. [2015] for an axon diameter (D) of 3.5 µm. The FC, DF-Peterson, VTA-Chaturvedi, and VTA-Madler PAMs were calculated for D=5.7 µm. The rows denote results for the: (A) internal capsule fibers of passage, (B) hyperdirect pathway, and (C) cerebellothalamic tract. (1) Threshold stimulus amplitude (V_{th}) as a function of electrode-to-axon distance. In this plot, we set axons with V_{th} > 10 V as 10 V, so that all axons representing a pathway can be visualized in the field of view. Electrode-to-axon distance is calculated from the center of the electrode contact. (2) V_{th} of the VTA-Astrom (D=3.5 µm) as a function of the V_{th} of the FC PAM (D=5.7 µm). In this plot, we set axons with V_{th} > 10 V as 10 V, so that all axons representing a pathway can be visualized in the field of view. (3) Errors in the V_{th} of the VTA-Astrom as a function of electrode-to-axon distance. (4) Recruitment curves calculated with each method. The stimulus pulse width was 90 µs, electrode configuration was contact 2 (-), case (+).

References

Accolla EA, Herrojo Ruiz M, Horn A, Schneider GH, Schmitz-Hübsch T, Draganski B, Kühn AA. Brain networks modulated by subthalamic nucleus deep brain stimulation. Brain. 2016 Jul 13;139(9):2503-15.

Akhtari M, Emin D, Ellingson BM, Woodworth D, Frew A, Mathern GW. Measuring the local electrical conductivity of human brain tissue. Journal of Applied Physics. 2016 Feb 14;119(6):064701.

Akram H, Sotiropoulos SN, Jbabdi S, Georgiev D, Mahlknecht P, Hyam J, Foltynie T, Limousin P, De Vita E, Jahanshahi M, Hariz M. Subthalamic deep brain stimulation sweet spots and hyperdirect cortical connectivity in parkinson's disease. NeuroImage. 2017 Sep 1;158:332-45.

Anderson ME, Postupna N, Ruffo M. Effects of high-frequency stimulation in the internal globus pallidus on the activity of thalamic neurons in the awake monkey. Journal of neurophysiology. 2003 Feb 1;89(2):1150-60.

Anderson VC, Burchiel KJ, Hogarth P, Favre J, Hammerstad JP. Pallidal vs subthalamic nucleus deep brain stimulation in Parkinson disease. Archives of neurology. 2005 Apr 1;62(4):554-60.

Aravamuthan BR, Muthusamy KA, Stein JF, Aziz TZ, Johansen-Berg H. Topography of cortical and subcortical connections of the human pedunculopontine and subthalamic nuclei. Neuroimage. 2007 Sep 1;37(3):694-705.

Ashby P, Paradiso G, Saint-Cyr JA, Chen R, Lang AE, Lozano AM. Potentials recorded at the scalp by stimulation near the human subthalamic nucleus. Clinical Neurophysiology. 2001 Mar 31;112(3):431-7.

Åström M, Tripoliti E, Hariz MI, Zrinzo LU, Martinez-Torres I, Limousin P, Wårdell K. Patient-specific model-based investigation of speech intelligibility and movement during deep brain stimulation. Stereotactic and functional neurosurgery. 2010;88(4):224-33.

Åström M, Diczfalusy E, Martens H, Wårdell K. Relationship between neural activation and electric field distribution during deep brain stimulation. IEEE Transactions on Biomedical Engineering. 2015 Feb;62(2):664-72.

Bally JF, Vargas MI, Horvath J, Fleury V, Burkhard P, Momjian S, Pollak P, Boex C. Localization of deep brain stimulation contacts using corticospinal/corticobulbar tracts stimulation. Frontiers in Neurology. 2017 May 31;8:239.

Baker KB, Montgomery EB, Rezai AR, Burgess R, Lüders HO. Subthalamic nucleus deep brain stimulus evoked potentials: physiological and therapeutic implications. Movement Disorders. 2002 Sep 1;17(5):969-83.

Barone P, Antonini A, Colosimo C, Marconi R, Morgante L, Avarello TP, Bottacchi E, Cannas A, Ceravolo G, Ceravolo R, Cicarelli G. The PRIAMO study: a multicenter assessment of nonmotor symptoms and their impact on quality of life in Parkinson's disease. Movement Disorders. 2009 Aug 15;24(11):1641-9.

Basser PJ, Mattiello J, LeBihan D. MR diffusion tensor spectroscopy and imaging. Biophysical journal. 1994 Jan 1;66(1):259-67.

Behrens TE, Johansen-Berg H, Woolrich MW, Smith SM, Wheeler-Kingshott CA, Boulby PA, Barker GJ, Sillery EL, Sheehan K, Ciccarelli O, Thompson AJ. Non-invasive mapping of connections between human thalamus and cortex using diffusion imaging. Nature neuroscience. 2003 Jul 1;6(7):750-7.

Behrens TE, Berg HJ, Jbabdi S, Rushworth MF, Woolrich MW. Probabilistic diffusion tractography with multiple fibre orientations: What can we gain?. Neuroimage. 2007 Jan 1;34(1):144-55.

Benabid AL, Pollak P, Louveau A, Henry S, De Rougemont J. Combined (thalamotomy and stimulation) stereotactic surgery of the VIM thalamic nucleus for bilateral Parkinson disease. Stereotactic and functional neurosurgery. 1987;50(1-6):344-6.

Benabid AL, Pollak P, Hoffmann D, Gervason C, Hommel M, Perret JE, De Rougemont J, Gao DM. Long-term suppression of tremor by chronic stimulation of the ventral intermediate thalamic nucleus. The Lancet. 1991 Feb 16;337(8738):403-6.

Benabid AL, Pollak P, Gross C, Hoffmann D, Benazzouz A, Gao DM, Laurent A, Gentil M, Perret J. Acute and long-term effects of subthalamic nucleus stimulation in Parkinson's disease. Stereotactic and functional neurosurgery. 1994;62(1-4):76-84.

Brown P, Oliviero A, Mazzone P, Insola A, Tonali P, Di Lazzaro V. Dopamine dependency of oscillations between subthalamic nucleus and pallidum in Parkinson's disease. Journal of Neuroscience. 2001 Feb 1;21(3):1033-8.

Brunenberg EJ, Moeskops P, Backes WH, Pollo C, Cammoun L, Vilanova A, Janssen ML, Visser-Vandewalle VE, ter Haar Romeny BM, Thiran JP, Platel B. Structural and resting state functional connectivity of the subthalamic nucleus: identification of motor STN parts and the hyperdirect pathway. PloS one. 2012 Jun 29;7(6):e39061.

Butson CR, McIntyre CC. Tissue and electrode capacitance reduce neural activation volumes during deep brain stimulation. Clinical neurophysiology. 2005 Oct 31;116(10):2490-500.

Butson CR, Maks CB, McIntyre CC. Sources and effects of electrode impedance during deep brain stimulation. Clinical Neurophysiology. 2006 Feb 28;117(2):447-54.

Butson CR, McIntyre CC. Role of electrode design on the volume of tissue activated during deep brain stimulation. Journal of neural engineering. 2006 Mar;3(1):1-8.

Butson CR, Cooper SE, Henderson JM, McIntyre CC. Patient-specific analysis of the volume of tissue activated during deep brain stimulation. Neuroimage. 2007 Jan 15;34(2):661-70.

Butson CR, Cooper SE, Henderson JM, Wolgamuth B, McIntyre CC. Probabilistic analysis of activation volumes generated during deep brain stimulation. Neuroimage. 2011 Feb 1;54(3):2096-104.

Chaturvedi A, Butson CR, Lempka SF, Cooper SE, McIntyre CC. Patient-specific models of deep brain stimulation: influence of field model complexity on neural activation predictions. Brain stimulation. 2010 Apr 30;3(2):65-77.

Chaturvedi A, Foutz TJ, McIntyre CC. Current steering to activate targeted neural pathways during deep brain stimulation of the subthalamic region. Brain stimulation. 2012 Jul 31;5(3):369-77.

Chaturvedi A, Luján JL, McIntyre CC. Artificial neural network based characterization of the volume of tissue activated during deep brain stimulation. Journal of neural engineering. 2013 Sep 24;10(5):056023.

Cheung T, Nuño M, Hoffman M, Katz M, Kilbane C, Alterman R, Tagliati M. Longitudinal impedance variability in patients with chronically implanted DBS devices. Brain stimulation. 2013 Sep 30;6(5):746-51.

Chung K, Wallace J, Kim SY, Kalyanasundaram S, Andalman AS, Davidson TJ, Mirzabekov JJ, Zalocusky KA, Mattis J, Denisin AK, Pak S. Structural and molecular interrogation of intact biological systems. Nature. 2013 May 16;497(7449):332-7.

Coenen VA, Mädler B, Schiffbauer H, Urbach H, Allert N. Individual fiber anatomy of the subthalamic region revealed with diffusion tensor imaging: a concept to identify the deep brain stimulation target for tremor suppression. Neurosurgery. 2011 Apr 1;68(4):1069-76.

Coenen VA, Allert N, Mädler B. A role of diffusion tensor imaging fiber tracking in deep brain stimulation surgery: DBS of the dentato-rubro-thalamic tract (drt) for the treatment of therapy-refractory tremor. Acta neurochirurgica. 2011 Aug 1;153(8):1579-85.

Coenen VA, Schlaepfer TE, Allert N, Mädler B. Diffusion tensor imaging and neuromodulation: DTI as key technology for deep brain stimulation. Int Rev Neurobiol. 2012 Jan 1;107:207-34.

Connolly BS, Lang AE. Pharmacological treatment of Parkinson disease: a review. Jama. 2014 Apr 23;311(16):1670-83.

Cotzias GC, Papavasiliou PS, Gellene R. Modification of Parkinsonism—chronic treatment with L-dopa. New England Journal of Medicine. 1969 Feb 13;280(7):337-45.

Damier P, Hirsch EC, Agid Y, Graybiel AM. The substantia nigra of the human brain: II. Patterns of loss of dopamine-containing neurons in Parkinson's disease. Brain. 1999 Aug 1;122(8):1437-48.

de Hemptinne C, Swann NC, Ostrem JL, Ryapolova-Webb ES, San Luciano M, Galifianakis NB, Starr PA. Therapeutic deep brain stimulation reduces cortical phase-amplitude coupling in Parkinson's disease. Nature neuroscience. 2015 May 1;18(5):779-86.

DeLong MR. Primate models of movement disorders of basal ganglia origin. Trends in neurosciences. 1990 Jul 31;13(7):281-5.

Deuschl G, Schade-Brittinger C, Krack P, Volkmann J, Schäfer H, Bötzel K, Daniels C, Deutschländer A, Dillmann U, Eisner W, Gruber D. A randomized trial of deep-brain stimulation for Parkinson's disease. New England Journal of Medicine. 2006 Aug 31;355(9):896-908.

Duchin Y, Abosch A, Yacoub E, Sapiro G, Harel N. Feasibility of using ultra-high field (7 T) MRI for clinical surgical targeting. PloS one. 2012 May 17;7(5):e37328.

Edgley SA, Eyre JA, Lemon RN, Miller S. Comparison of activation of corticospinal neurons and spinal motor neurons by magnetic and electrical transcranial stimulation in the lumbosacral cord of the anaesthetized monkey. Brain: a journal of neurology. 1997 May 1;120(5):839-53.

Einevoll GT, Kayser C, Logothetis NK, Panzeri S. Modelling and analysis of local field potentials for studying the function of cortical circuits. Nature Reviews Neuroscience. 2013 Nov 1;14(11):770-85.

Eisenstein SA, Koller JM, Black KD, Campbell MC, Lugar HM, Ushe M, Tabbal SD, Karimi M, Hershey T, Perlmutter JS, Black KJ. Functional anatomy of subthalamic nucleus stimulation in Parkinson disease. Annals of neurology. 2014 Aug 1;76(2):279-95.

Fillard P, Descoteaux M, Goh A, Gouttard S, Jeurissen B, Malcolm J, Ramirez-Manzanares A, Reisert M, Sakaie K, Tensaouti F, Yo T. Quantitative evaluation of 10 tractography algorithms on a realistic diffusion MR phantom. Neuroimage. 2011 May 1;56(1):220-34.

Firmin L, Field P, Maier MA, Kraskov A, Kirkwood PA, Nakajima K, Lemon RN, Glickstein M. Axon diameters and conduction velocities in the macaque pyramidal tract. Journal of neurophysiology. 2014 Sep 15;112(6):1229-40.

Fischl B. FreeSurfer. Neuroimage. 2012 Aug 15;62(2):774-81.

Foutz TJ, McIntyre CC. Evaluation of novel stimulus waveforms for deep brain stimulation. Journal of neural engineering. 2010 Nov 17;7(6):066008.

Fox MD, Buckner RL, Liu H, Chakravarty MM, Lozano AM, Pascual-Leone A. Resting-state networks link invasive and noninvasive brain stimulation across diverse psychiatric and neurological diseases. Proceedings of the National Academy of Sciences. 2014 Oct 14;111(41):E4367-75.

Frankemolle AM, Wu J, Noecker AM, Voelcker-Rehage C, Ho JC, Vitek JL, McIntyre CC, Alberts JL. Reversing cognitive–motor impairments in Parkinson's disease patients using a computational modelling approach to deep brain stimulation programming. Brain. 2010 Jan 8;133(3):746-61.

Frankenhaeuser B, Huxley AF. The action potential in the myelinated nerve fibre of Xenopus laevis as computed on the basis of voltage clamp data. The Journal of Physiology. 1964 Jun 1;171(2):302-15.

Gabriel C, Gabriel S, Corthout E. The dielectric properties of biological tissues: I. Literature survey. Physics in medicine and biology. 1996 Nov;41(11):2231.

Gallay MN, Jeanmonod D, Liu J, Morel A. Human pallidothalamic and cerebellothalamic tracts: anatomical basis for functional stereotactic neurosurgery. Brain Structure and Function. 2008 Aug 1;212(6):443-63.

Giannicola G, Marceglia S, Rossi L, Mrakic-Sposta S, Rampini P, Tamma F, Cogiamanian F, Barbieri S, Priori A. The effects of levodopa and ongoing deep brain stimulation on subthalamic beta oscillations in Parkinson's disease. Experimental neurology. 2010 Nov 30;226(1):120-7.

Glasser MF, Smith SM, Marcus DS, Andersson JL, Auerbach EJ, Behrens TE, Coalson TS, Harms MP, Jenkinson M, Moeller S, Robinson EC. The human connectome project's neuroimaging approach. Nature Neuroscience. 2016 Sep 1;19(9):1175-87.

Golestanirad L, Izquierdo AP, Graham SJ, Mosig JR, Pollo C. Effect of realistic modeling of deep brain stimulation on the prediction of volume of activated tissue. Progress In Electromagnetics Research. 2012;126:1-6.

Gradinaru V, Mogri M, Thompson KR, Henderson JM, Deisseroth K. Optical deconstruction of parkinsonian neural circuitry. Science. 2009 Apr 17;324(5925):354-9.

Graf von Keyserlingk D, Schramm U. Diameter of axons and thickness of myelin sheaths of the pyramidal tract fibres in the adult human medullary pyramid. Anatomischer Anzeiger. 1984;157(2):97-111.

Grill WM, Mortimer JT. Electrical properties of implant encapsulation tissue. Annals of biomedical engineering. 1994 Jan 1;22(1):23-33.

Grill WM, Cantrell MB, Robertson MS. Antidromic propagation of action potentials in branched axons: implications for the mechanisms of action of deep brain stimulation. Journal of computational neuroscience. 2008 Feb 1;24(1):81-93.

Groppa S, Herzog J, Falk D, Riedel C, Deuschl G, Volkmann J. Physiological and anatomical decomposition of subthalamic neurostimulation effects in essential tremor. Brain. 2014 Jan;137(1):109-21.

Gunalan K, Chaturvedi A, Howell B, Duchin Y, Lempka SF, Patriat R, Sapiro G, Harel N, McIntyre CC. Creating and parameterizing patient-specific deep brain stimulation pathway-activation models using the hyperdirect pathway as an example. PloS one. 2017 Apr 25;12(4):e0176132.

Gutman DA, Holtzheimer PE, Behrens TE, Johansen-Berg H, Mayberg HS. A tractography analysis of two deep brain stimulation white matter targets for depression. Biological psychiatry. 2009 Feb 15;65(4):276-82.

Hahn PJ, McIntyre CC. Modeling shifts in the rate and pattern of subthalamopallidal network activity during deep brain stimulation. Journal of computational neuroscience. 2010 Jun 1;28(3):425-41.

Hamel W, Köppen JA, Alesch F, Antonini A, Barcia JA, Bergman H, Chabardes S, Contarino MF, Cornu P, Demmel W, Deuschl G. Targeting of the Subthalamic Nucleus for Deep Brain Stimulation: A Survey Among Parkinson Disease Specialists. World neurosurgery. 2017 Mar 31;99:41-6.

Hartmann CJ, Wojtecki L, Vesper J, Volkmann J, Groiss SJ, Schnitzler A, Südmeyer M. Long-term evaluation of impedance levels and clinical development in subthalamic deep brain stimulation for Parkinson's disease. Parkinsonism & related disorders. 2015 Oct 31;21(10):1247-50.

Hashimoto T, Elder CM, Okun MS, Patrick SK, Vitek JL. Stimulation of the subthalamic nucleus changes the firing pattern of pallidal neurons. Journal of neuroscience. 2003 Mar 1;23(5):1916-23.

Haynes WI, Haber SN. The organization of prefrontal-subthalamic inputs in primates provides an anatomical substrate for both functional specificity and integration: implications for Basal Ganglia models and deep brain stimulation. Journal of Neuroscience. 2013 Mar 13;33(11):4804-14.

Hemm S, Coste J, Gabrillargues J, Ouchchane L, Sarry L, Caire F, Vassal F, Nuti C, Derost P, Durif F, Lemaire JJ. Contact position analysis of deep brain stimulation electrodes on post-operative CT images. Acta neurochirurgica. 2009 Jul 1;151(7):823-9.

Henderson JM. “Connectomic surgery”: diffusion tensor imaging (DTI) tractography as a targeting modality for surgical modulation of neural networks. Frontiers in integrative neuroscience. 2012;6.

Herzog J, Fietzek U, Hamel W, Morsnowski A, Steigerwald F, Schrader B, Weinert D, Pfister G, Müller D, Mehdorn HM, Deuschl G. Most effective stimulation site in subthalamic deep brain stimulation for Parkinson's disease. Movement disorders. 2004 Sep 1;19(9):1050-4.

Hines ML, Carnevale NT. NEURON: a tool for neuroscientists. The Neuroscientist. 2001 Apr;7(2):123-35.

Hodgkin AL, Huxley AF. A quantitative description of membrane current and its application to conduction and excitation in nerve. The Journal of physiology. 1952 Aug 28;117(4):500-44.

Hongo T, Kudo N, Sasaki S, Yamashita M, Yoshida K, Ishizuka N, Mannen H. Trajectory of group Ia and Ib fibers from the hind-limb muscles at the L3 and L4 segments of the spinal cord of the cat. Journal of Comparative Neurology. 1987 Aug 8;262(2):159-94.

Horn A, Kühn AA. Lead-DBS: a toolbox for deep brain stimulation electrode localizations and visualizations. Neuroimage. 2015 Feb 15;107:127-35.

Horn A, Blankenburg F. Toward a standardized structural–functional group connectome in MNI space. NeuroImage. 2016 Jan 1;124:310-22.

Horn A, Reich M, Vorwerk J, Li N, Wenzel G, Fang Q, Schmitz-Hübsch T, Nickl R, Kupsch A, Volkmann J, Kühn AA. Connectivity predicts deep brain stimulation outcome in Parkinson's disease. Annals of Neurology. 2017 Jul;82(1):67-78.

Howell B, McIntyre CC. Analyzing the tradeoff between electrical complexity and accuracy in patient-specific computational models of deep brain stimulation. Journal of neural engineering. 2016 May 11;13(3):036023.

Howell B, McIntyre CC. Role of Soft-Tissue Heterogeneity in Computational Models of Deep Brain Stimulation. Brain stimulation. 2017 Feb 28;10(1):46-50.

Humphrey DR, Corrie WS. Properties of pyramidal tract neuron system within a functionally defined subregion of primate motor cortex. Journal of Neurophysiology. 1978 Jan 1;41(1):216-43.

Iacono MI, Neufeld E, Akinnagbe E, Bower K, Wolf J, Oikonomidis IV, Sharma D, Lloyd B, Wilm BJ, Wyss M, Pruessmann KP. MIDA: a multimodal imaging-based detailed anatomical model of the human head and neck. PloS one. 2015 Apr 22;10(4):e0124126.

Jankovic J, McDermott M, Carter J, Gauthier S, Goetz C, Golbe L, Huber S, Koller W, Olanow C, Shoulson I, Stern M. Variable expression of Parkinson's disease A base-line analysis of the DAT ATOP cohort. Neurology. 1990 Oct 1;40(10):1529-34.

Jefferys JG. Nonsynaptic modulation of neuronal activity in the brain: electric currents and extracellular ions. Physiological reviews. 1995 Oct 1;75(4):689-723.

Jenkinson M, Smith S. A global optimisation method for robust affine registration of brain images. Medical image analysis. 2001 Jun 30;5(2):143-56.

Jenkinson M, Bannister P, Brady M, Smith S. Improved optimization for the robust and accurate linear registration and motion correction of brain images. Neuroimage. 2002 Oct 31;17(2):825-41.

Jenkinson M, Beckmann CF, Behrens TE, Woolrich MW, Smith SM. FSL. Neuroimage. 2012 Aug 15;62(2):782-90.

Johansen-Berg H, Gutman DA, Behrens TE, Matthews PM, Rushworth MF, Katz E, Lozano AM, Mayberg HS. Anatomical connectivity of the subgenual cingulate region targeted with deep brain stimulation for treatment-resistant depression. Cerebral cortex. 2008 Jun;18(6):1374-83.

Jones DK, Knösche TR, Turner R. White matter integrity, fiber count, and other fallacies: the do's and don'ts of diffusion MRI. Neuroimage. 2013 Jun 30;73:239-54.

Kahan J, Urner M, Moran R, Flandin G, Marreiros A, Mancini L, White M, Thornton J, Yousry T, Zrinzo L, Hariz M. Resting state functional MRI in Parkinson's disease: the impact of deep brain stimulation on 'effective'connectivity. Brain. 2014 Apr 1;137(4):1130-44.

Kang G, Lowery MM. Effects of antidromic and orthodromic activation of STN afferent axons during DBS in Parkinson's disease: a simulation study. Frontiers in computational neuroscience. 2014 Mar 19;8:32.

Kim J, Lenglet C, Duchin Y, Sapiro G, Harel N. Semiautomatic segmentation of brain subcortical structures from high-field MRI. IEEE journal of biomedical and health informatics. 2014 Sep;18(5):1678-95.

Kita T, Kita H. The subthalamic nucleus is one of multiple innervation sites for long-range corticofugal axons: a single-axon tracing study in the rat. Journal of Neuroscience. 2012 Apr 25;32(17):5990-9.

Klein A, Andersson J, Ardekani BA, Ashburner J, Avants B, Chiang MC, Christensen GE, Collins DL, Gee J, Hellier P, Song JH. Evaluation of 14 nonlinear deformation algorithms applied to human brain MRI registration. Neuroimage. 2009 Jul 1;46(3):786-802.

Klein JC, Barbe MT, Seifried C, Baudrexel S, Runge M, Maarouf M, Gasser T, Hattingen E, Liebig T, Deichmann R, Timmermann L. The tremor network targeted by successful VIM deep brain stimulation in humans. Neurology. 2012 Mar 13;78(11):787-95.

Krauth A, Blanc R, Poveda A, Jeanmonod D, Morel A, Székely G. A mean three-dimensional atlas of the human thalamus: generation from multiple histological data. Neuroimage. 2010 Feb 1;49(3):2053-62.

Kühn AA, Kupsch A, Schneider GH, Brown P. Reduction in subthalamic 8–35 Hz oscillatory activity correlates with clinical improvement in Parkinson's disease. European Journal of Neuroscience. 2006 Apr 1;23(7):1956-60.

Lauro PM, Vanegas-Arroyave N, Huang L, Taylor PA, Zaghloul KA, Lungu C, Saad ZS, Horovitz SG. DBSproc: an open source process for DBS electrode localization and tractographic analysis. Human brain mapping. 2016 Jan 1;37(1):422-33.

Leksell L. A stereotaxic apparatus for intracerebral surgery. Acta Chirurgica Scandinavica. 1950 Jan 1;99(3):229-33.

Lempka SF, Johnson MD, Miocinovic S, Vitek JL, McIntyre CC. Current-controlled deep brain stimulation reduces in vivo voltage fluctuations observed during voltage-controlled stimulation. Clinical Neurophysiology. 2010 Dec 31;121(12):2128-33.

Lenglet C, Abosch A, Yacoub E, De Martino F, Sapiro G, Harel N. Comprehensive in vivo mapping of the human basal ganglia and thalamic connectome in individuals using 7T MRI. PloS one. 2012 Jan 3;7(1):e29153.

Li S, Arbuthnott GW, Jutras MJ, Goldberg JA, Jaeger D. Resonant antidromic cortical circuit activation as a consequence of high-frequency subthalamic deep-brain stimulation. Journal of neurophysiology. 2007 Dec 1;98(6):3525-37.

Li Q, Ke Y, Chan DC, Qian ZM, Yung KK, Ko H, Arbuthnott GW, Yung WH. Therapeutic deep brain stimulation in Parkinsonian rats directly influences motor cortex. Neuron. 2012 Dec 6;76(5):1030-41.

Limousin P, Pollak P, Benazzouz A, Hoffmann D, Le Bas JF, Perret JE, Benabid AL, Broussolle E. Effect on parkinsonian signs and symptoms of bilateral subthalamic nucleus stimulation. The Lancet. 1995 Jan 14;345(8942):91-5.

Limousin P, Krack P, Pollak P, Benazzouz A, Ardouin C, Hoffmann D, Benabid AL. Electrical stimulation of the subthalamic nucleus in advanced Parkinson's disease. New England Journal of Medicine. 1998 Oct 15;339(16):1105-11.

Lozano AM, Dostrovsky J, Chen R, Ashby P. Deep brain stimulation for Parkinson's disease: disrupting the disruption. The Lancet Neurology. 2002 Aug 31;1(4):225-31.

Lozano AM, Lipsman N. Probing and regulating dysfunctional circuits using deep brain stimulation. Neuron. 2013 Feb 6;77(3):406-24.

Lujan JL, Chaturvedi A, Malone DA, Rezai AR, Machado AG, McIntyre CC. Axonal pathways linked to therapeutic and nontherapeutic outcomes during psychiatric deep brain stimulation. Human brain mapping. 2012 Apr 1;33(4):958-68.

Lujan JL, Chaturvedi A, Choi KS, Holtzheimer PE, Gross RE, Mayberg HS, McIntyre CC. Tractography-activation models applied to subcallosal cingulate deep brain stimulation. Brain stimulation. 2013 Sep 30;6(5):737-9.

Mädler B, Coenen VA. Explaining clinical effects of deep brain stimulation through simplified target-specific modeling of the volume of activated tissue. American Journal of Neuroradiology. 2012 Jun 1;33(6):1072-80.

Mahlknecht P, Akram H, Georgiev D, Tripoliti E, Candelario J, Zacharia A, Zrinzo L, Hyam J, Hariz M, Foltynie T, Rothwell JC. Pyramidal tract activation due to subthalamic deep brain stimulation in Parkinson's disease. Movement Disorders. 2017 Jun 7.

Mathai A, Wichmann T, Smith Y. More than meets the eye—Myelinated axons crowd the subthalamic nucleus. Movement Disorders. 2013 Nov 1;28(13):1811-5.

McIntyre CC, Grill WM. Excitation of central nervous system neurons by nonuniform electric fields. Biophysical journal. 1999 Feb 28;76(2):878-88.

McIntyre CC, Grill WM. Selective microstimulation of central nervous system neurons. Annals of biomedical engineering. 2000 Mar 1;28(3):219-33.

McIntyre CC, Richardson AG, Grill WM. Modeling the excitability of mammalian nerve fibers: influence of afterpotentials on the recovery cycle. Journal of neurophysiology. 2002 Feb 1;87(2):995-1006.

McIntyre CC, Grill WM, Sherman DL, Thakor NV. Cellular effects of deep brain stimulation: model-based analysis of activation and inhibition. Journal of neurophysiology. 2004 Apr 1;91(4):1457-69.

McIntyre CC, Miocinovic S, Butson CR. Computational analysis of deep brain stimulation. Expert review of medical devices. 2007 Sep 1;4(5):615-22.

McIntyre CC, Hahn PJ. Network perspectives on the mechanisms of deep brain stimulation. Neurobiology of disease. 2010 Jun 30;38(3):329-37.

McIntyre CC, Anderson RW. Deep brain stimulation mechanisms: the control of network activity via neurochemistry modulation. Journal of neurochemistry. 2016 Oct 1;139(S1):338-45.

McNeal DR. Analysis of a model for excitation of myelinated nerve. IEEE Transactions on Biomedical Engineering. 1976 Jul(4):329-37.

Merrill DR, Bikson M, Jefferys JG. Electrical stimulation of excitable tissue: design of efficacious and safe protocols. Journal of neuroscience methods. 2005 Feb 15;141(2):171-98.

Miocinovic S, Parent M, Butson CR, Hahn PJ, Russo GS, Vitek JL, McIntyre CC. Computational analysis of subthalamic nucleus and lenticular fasciculus activation during therapeutic deep brain stimulation. Journal of neurophysiology. 2006 Sep 1;96(3):1569-80.

Miocinovic S, Noecker AM, Maks CB, Butson CR, McIntyre CC. Cicerone: stereotactic neurophysiological recording and deep brain stimulation electrode

placement software system. Acta neurochirurgica. Supplement. 2007;97(Pt 2):561-7.

Miocinovic S, Lempka SF, Russo GS, Maks CB, Butson CR, Sakaie KE, Vitek JL, McIntyre CC. Experimental and theoretical characterization of the voltage distribution generated by deep brain stimulation. Experimental neurology. 2009 Mar 31;216(1):166-76.

Miocinovic S, Somayajula S, Chitnis S, Vitek JL. History, applications, and mechanisms of deep brain stimulation. JAMA neurology. 2013 Feb 1;70(2):163-71.

Moffitt MA, McIntyre CC, Grill WM. Prediction of myelinated nerve fiber stimulation thresholds: limitations of linear models. IEEE Transactions on Biomedical Engineering. 2004 Feb;51(2):229-36.

Montgomery EB. Effects of GPi stimulation on human thalamic neuronal activity. Clinical Neurophysiology. 2006 Dec 31;117(12):2691-702.

Moro E, Esselink RJ, Xie J, Hommel M, Benabid AL, Pollak P. The impact on Parkinson's disease of electrical parameter settings in STN stimulation. Neurology. 2002 Sep 10;59(5):706-13.

Morris DM, Embleton KV, Parker GJ. Probabilistic fibre tracking: differentiation of connections from chance events. Neuroimage. 2008 Oct 1;42(4):1329-39.

Moseley ME, Cohen Y, Kucharczyk J, Mintorovitch J, Asgari HS, Wendland MF, Tsuruda J, Norman D. Diffusion-weighted MR imaging of anisotropic water diffusion in cat central nervous system. Radiology. 1990 Aug;176(2):439-45.

Nambu A, Tokuno H, Takada M. Functional significance of the cortico–subthalamo–pallidal 'hyperdirect'pathway. Neuroscience research. 2002 Jun 30;43(2):111-7.

Nelson PG. Interaction between spinal motoneurons of the cat. Journal of neurophysiology. 1966 Mar 1;29(2):275-87.

Nowak LG, Bullier J. Axons, but not cell bodies, are activated by electrical stimulation in cortical gray matter I. Evidence from chronaxie measurements. Experimental brain research. 1998 Feb 1;118(4):477-88.

Noecker AM, Choi KS, Riva-Posse P, Gross RE, Mayberg HS, McIntyre CC. StimVision Software: Examples and Applications in Subcallosal Cingulate Deep Brain Stimulation for Depression. Neuromodulation: Technology at the Neural Interface. 2017 Jun 27.

Nowinski WL, Belov D, Pollak P, Benabid AL. Statistical analysis of 168 bilateral subthalamic nucleus implantations by means of the probabilistic functional atlas. Operative Neurosurgery. 2005 Oct 1;57(Suppl 4):319-30.

Obeso JA, Rodriguez-Oroz MC, Goetz CG, Marin C, Kordower JH, Rodriguez M, Hirsch EC, Farrer M, Schapira AH, Halliday G. Missing pieces in the Parkinson's disease puzzle. Nature medicine. 2010 Jun 1;16(6):653-61.

Odekerken VJ, van Laar T, Staal MJ, Mosch A, Hoffmann CF, Nijssen PC, Beute GN, van Vugt JP, Lenders MW, Contarino MF, Mink MS. Subthalamic nucleus versus globus pallidus bilateral deep brain stimulation for advanced Parkinson's disease (NSTAPS study): a randomised controlled trial. The Lancet Neurology. 2013 Jan 31;12(1):37-44.

O'Shea DJ, Trautmann E, Chandrasekaran C, Stavisky S, Kao JC, Sahani M, Ryu S, Deisseroth K, Shenoy KV. The need for calcium imaging in nonhuman primates: New motor neuroscience and brain-machine interfaces. Experimental neurology. 2017 Jan 31;287:437-51.

Parent A, Hazrati LN. Functional anatomy of the basal ganglia. II. The place of subthalamic nucleus and external pallidum in basal ganglia circuitry. Brain research. Brain research reviews. 1995 Jan;20(1):128-54.

Parent M, Parent A. The pallidofugal motor fiber system in primates. Parkinsonism & related disorders. 2004 Jun 30;10(4):203-11.

Peterson EJ, Izad O, Tyler DJ. Predicting myelinated axon activation using spatial characteristics of the extracellular field. Journal of neural engineering. 2011 Jul 13;8(4):046030.

Petersen MV, Lund TE, Sunde N, Frandsen J, Rosendal F, Juul N, Østergaard K. Probabilistic versus deterministic tractography for delineation of the cortico-subthalamic hyperdirect pathway in patients with Parkinson disease selected for deep brain stimulation. Journal of neurosurgery. 2016 Jul 8;126(5):1657-68.

Popovic MA, Foust AJ, McCormick DA, Zecevic D. The spatio-temporal characteristics of action potential initiation in layer 5 pyramidal neurons: a voltage imaging study. The Journal of physiology. 2011 Sep 1;589(17):4167-87.

Ranck JB. Which elements are excited in electrical stimulation of mammalian central nervous system: a review. Brain research. 1975 Nov 21;98(3):417-40.

Rascol O, Brooks DJ, Korczyn AD, De Deyn PP, Clarke CE, Lang AE. A five-year study of the incidence of dyskinesia in patients with early Parkinson's disease who were treated with ropinirole or levodopa. New England Journal of Medicine. 2000 May 18;342(20):1484-91.

Rattay F. Analysis of models for external stimulation of axons. IEEE transactions on biomedical engineering. 1986 Oct(10):974-7.

Rattay F. The basic mechanism for the electrical stimulation of the nervous system. Neuroscience. 1999 Mar 31;89(2):335-46.

Reich MM, Steigerwald F, Sawalhe AD, Reese R, Gunalan K, Johannes S, Nickl R, Matthies C, McIntyre CC, Volkmann J. Short pulse width widens the therapeutic window of subthalamic neurostimulation. Annals of clinical and translational neurology. 2015 Apr 1;2(4):427-32.

Reinacher PC, Krüger MT, Coenen VA, Shah M, Roelz R, Jenkner C, Egger K. Determining the Orientation of Directional Deep Brain Stimulation Electrodes Using 3D Rotational Fluoroscopy. American Journal of Neuroradiology. 2017 Jun 1;38(6):1111-6.

Riva-Posse P, Choi KS, Holtzheimer PE, McIntyre CC, Gross RE, Chaturvedi A, Crowell AL, Garlow SJ, Rajendra JK, Mayberg HS. Defining critical white matter pathways mediating successful subcallosal cingulate deep brain stimulation for treatment-resistant depression. Biological psychiatry. 2014 Dec 15;76(12):963-9.

Riva-Posse P, Choi KS, Holtzheimer PE, Crowell AL, Garlow SJ, Rajendra JK, McIntyre CC, Gross RE, Mayberg HS. A connectomic approach for subcallosal cingulate deep brain stimulation surgery: prospective targeting in treatment-resistant depression. Molecular psychiatry. 2017 Apr 11.

Rizzone M, Lanotte M, Bergamasco B, Tavella A, Torre E, Faccani G, Melcarne A, Lopiano L. Deep brain stimulation of the subthalamic nucleus in Parkinson's disease: effects of variation in stimulation parameters. Journal of Neurology, Neurosurgery & Psychiatry. 2001 Aug 1;71(2):215-9.

Rolston JD, Englot DJ, Starr PA, Larson PS. An unexpectedly high rate of revisions and removals in deep brain stimulation surgery: Analysis of multiple databases. Parkinsonism & related disorders. 2016 Dec 31;33:72-7.

Rossi MA, Stebbins G, Murphy C, Greene D, Brinker S, Sarcu D, Tenharmsel A, Stoub T, Stein MA, Hoeppner TJ, Byrne RW. Predicting white matter targets for direct neurostimulation therapy. Epilepsy research. 2010 Oct 31;91(2):176-86.

Sadakane O, Masamizu Y, Watakabe A, Terada SI, Ohtsuka M, Takaji M, Mizukami H, Ozawa K, Kawasaki H, Matsuzaki M, Yamamori T. Long-term two-photon calcium imaging of neuronal populations with subcellular resolution in adult non-human primates. Cell reports. 2015 Dec 1;13(9):1989-99.

Saint-Cyr JA, Hoque T, Pereira LC, Dostrovsky JO, Hutchison WD, Mikulis DJ, Abosch A, Sime E, Lang AE, Lozano AM. Localization of clinically effective stimulating electrodes in the human subthalamic nucleus on magnetic resonance imaging. Journal of neurosurgery. 2002 Nov;97(5):1152-66.

Sanders TH, Jaeger D. Optogenetic stimulation of cortico-subthalamic projections is sufficient to ameliorate bradykinesia in 6-ohda lesioned mice. Neurobiology of disease. 2016 Nov 30;95:225-37.

Sato F, Parent M, Levesque M, Parent A. Axonal branching pattern of neurons of the subthalamic nucleus in primates. Journal of Comparative Neurology. 2000 Aug 14;424(1):142-52.

Schrag A, Quinn N. Dyskinesias and motor fluctuations in Parkinson's disease: A community-based study. Brain. 2000 Nov 1;123(11):2297-305.

Setsompop K, Kimmlingen R, Eberlein E, Witzel T, Cohen-Adad J, McNab JA, Keil B, Tisdall MD, Hoecht P, Dietz P, Cauley SF. Pushing the limits of in vivo diffusion MRI for the Human Connectome Project. Neuroimage. 2013 Oct 15;80:220-33.

Schlaepfer TE, Bewernick BH, Kayser S, Mädler B, Coenen VA. Rapid effects of deep brain stimulation for treatment-resistant major depression. Biological psychiatry. 2013 Jun 15;73(12):1204-12.

Smith SM. Fast robust automated brain extraction. Human brain mapping. 2002 Nov 1;17(3):143-55.

Struijk JJ, Holsheimer J, van der Heide GG, Boom HB. Recruitment of dorsal column fibers in spinal cord stimulation: influence of collateral branching. IEEE Transactions on Biomedical Engineering. 1992 Sep;39(9):903-12.

Sweet JA, Walter BL, Gunalan K, Chaturvedi A, McIntyre CC, Miller JP. Fiber tractography of the axonal pathways linking the basal ganglia and cerebellum in Parkinson disease: implications for targeting in deep brain stimulation. Journal of neurosurgery. 2014 Apr;120(4):988-96.

Sweeney JD, Mortimer JT, Durand D. MODELING OF MAMMALIAN MYELINATED NERVE FOR FUNCTIONAL NEUROMUSCULAR STIMULATION. InIEEE/Engineering in Medicine and Biology Society Annual Conference 1987. IEEE.

Thomas C, Frank QY, Irfanoglu MO, Modi P, Saleem KS, Leopold DA, Pierpaoli C. Anatomical accuracy of brain connections derived from diffusion MRI tractography is inherently limited. Proceedings of the National Academy of Sciences. 2014 Nov 18;111(46):16574-9.

Tommasi G, Krack P, Fraix V, Le Bas JF, Chabardes S, Benabid AL, Pollak P. Pyramidal tract side effects induced by deep brain stimulation of the subthalamic nucleus. Journal of Neurology, Neurosurgery & Psychiatry. 2008 Jul 1;79(7):813-9.

Tripoliti E, Limousin P, Foltynie T, Candelario J, Aviles-Olmos I, Hariz MI, Zrinzo L. Predictive factors of speech intelligibility following subthalamic nucleus stimulation in consecutive patients with Parkinson's disease. Movement Disorders. 2014 Apr 1;29(4):532-8.

Van Essen DC, Smith SM, Barch DM, Behrens TE, Yacoub E, Ugurbil K, Wu-Minn HCP Consortium. The WU-Minn human connectome project: an overview. Neuroimage. 2013 Oct 15;80:62-79.

Vanegas-Arroyave N, Lauro PM, Huang L, Hallett M, Horovitz SG, Zaghloul KA, Lungu C. Tractography patterns of subthalamic nucleus deep brain stimulation. Brain. 2016 Feb 26;139(4):1200-10.

Volkmann J, Herzog J, Kopper F, Deuschl G. Introduction to the programming of deep brain stimulators. Movement disorders. 2002 Mar 1;17(S3):S181-7.

Volkmann J, Moro E, Pahwa R. Basic algorithms for the programming of deep brain stimulation in Parkinson's disease. Movement Disorders. 2006 Jun 1;21(S14).

Walckiers G, Fuchs B, Thiran JP, Mosig JR, Pollo C. Influence of the implanted pulse generator as reference electrode in finite element model of monopolar deep brain stimulation. Journal of neuroscience methods. 2010 Jan 30;186(1):90-6.

Walker HC, Huang H, Gonzalez CL, Bryant JE, Killen J, Cutter GR, Knowlton RC, Montgomery EB, Guthrie BL, Watts RL. Short latency activation of cortex during clinically effective subthalamic deep brain stimulation for Parkinson's disease. Movement Disorders. 2012 Jun 1;27(7):864-73.

Warman EN, Grill WM, Durand D. Modeling the effects of electric fields on nerve fibers: determination of excitation thresholds. IEEE Transactions on Biomedical Engineering. 1992 Dec;39(12):1244-54.

Wei XF, Grill WM. Impedance characteristics of deep brain stimulation electrodes in vitro and in vivo. Journal of neural engineering. 2009 Jul 9;6(4):046008.

Welter ML, Schüpbach M, Czernecki V, Karachi C, Fernandez-Vidal S, Golmard JL, Serra G, Navarro S, Welaratne A, Hartmann A, Mesnage V. Optimal target

localization for subthalamic stimulation in patients with Parkinson disease. Neurology. 2014 Apr 15;82(15):1352-61.

Whitmer D, De Solages C, Hill B, Yu H, Henderson JM, Bronte-Stewart H. High frequency deep brain stimulation attenuates subthalamic and cortical rhythms in Parkinson's disease. Frontiers in human neuroscience. 2012 June 4;6:155.

Zhang Y, Brady M, Smith S. Segmentation of brain MR images through a hidden Markov random field model and the expectation-maximization algorithm. IEEE transactions on medical imaging. 2001 Jan;20(1):45-57.

Zimnik AJ, Nora GJ, Desmurget M, Turner RS. Movement-related discharge in the macaque globus pallidus during high-frequency stimulation of the subthalamic nucleus. Journal of Neuroscience. 2015 Mar 4;35(9):3978-89.

Zitella LM, Mohsenian K, Pahwa M, Gloeckner C, Johnson MD. Computational modeling of pedunculopontine nucleus deep brain stimulation. Journal of neural engineering. 2013 May 31;10(4):045005.

Zitella LM, Teplitzky BA, Yager P, Hudson HM, Brintz K, Duchin Y, Harel N, Vitek JL, Baker KB, Johnson MD. Subject-specific computational modeling of DBS in the PPTg area. Frontiers in computational neuroscience. 2015;9.